

AN ABSTRACT OF THE THESIS OF

Kevin J. Harada for the degree of Master of Science in Mechanical Engineering presented on September 27, 2010

Title: Development of a Small Scale Scroll Expander.

Abstract approved:

Richard B. Peterson

The organic Rankine cycle (ORC) is a versatile approach in the utilization of waste heat in the production of electricity, clean drinking water, and cooling. The efficiency of these cycles must be maximized to make them economical. Parameters for the optimization of ORCs such as evaporator and condenser temperature have practical limits. This is why the expander has the greatest effect in increasing the efficiency of an ORC when recovering waste heat.

In this thesis the design, fabrication, and demonstration of a small scale scroll expander will be presented. Scroll expanders are positive displacement expanders that have consistently shown high efficiencies in literature. The fabricated expander was modified from a compliant scroll compressor. It was self-starting and had external control over the seal piston pressure. Spherical miter gears placed the power takeoff on the side of the expander which allowed the lubrication system designed by the compressor manufacturer to function properly. The gears had the unforeseen effect of acting as an oil mister which improved the lubrication of the scroll assembly. It was dynamically balanced to minimize vibration.

This expander was demonstrated with both R134a and R245fa as working fluids with varying rotational speeds, expansion ratios, and achieved isentropic efficiencies typically over 70%. It achieved a maximum isentropic efficiency of 87.2% and a maximum power output of 1 [kW]. The performance characteristics such as speed, torque, and power were measured

using two separate dynamometers. It was shown that the expander shows good off design performance and has an optimal pressure ratio of approximately 3.3. It was also shown that its performance is a weak function of rotational speed. It is important to note the significant impact that a larger diameter shaft and shaft seal can have on performance. Break-in is another important consideration when evaluating performance.

©Copyright by Kevin J. Harada

September 27, 2010

All Rights Reserved

Development of a Small Scale Scroll Expander

by

Kevin J. Harada

A THESIS

submitted to

Oregon State University

in partial fulfillment of
the requirements for the
degree of

Master of Science

Presented September 27, 2010

Commencement June 2011

Master of Science thesis of Kevin J. Harada presented on September 27, 2010

APPROVED:

Major Professor, representing Mechanical Engineering

Head of the School of Mechanical Industrial and Manufacturing Engineering

Dean of the Graduate School

I understand that my thesis will become part of the permanent collection of Oregon State University libraries. My signature below authorizes release of my thesis to any reader upon request

Kevin J. Harada, Author

ACKNOWLEDGEMENTS

First of all, I would like to express my gratitude to my graduate professor Dr. Richard B. Peterson for giving me the opportunity to pursue my Masters of Science under him at Oregon State University. It has given me a multitude of experiences and opportunities I would not have had otherwise. My appreciation is extended to my graduate committee Dr. Annette R. Von Jouanne, Dr. Hailei Wang, and Dr. Kathy K. Mullet for their recommendations and advice on my thesis. Specially, I would like to thank Dr. Annette R. Von Jouanne for serving as my graduate minor professor in Electrical Engineering. I would like to extend my special thanks to Dr. Hailei Wang for being a supportive friend and colleague throughout my graduate studies. Without his hard work and efforts the scroll expander would not be the smooth running machine it is today.

I would like to thank in addition Erik W. Miller and Robbie Ingram-Goble for their contributions to the scroll expander and their support both as friends and colleagues. In addition I am very grateful for the grammatical edits my sister Emily J. Robertson contributed to my thesis. I am also grateful for the quality craftsmanship that Robert C. Wright, Denise M. Wright, Jim E. Blackburn, and the employees of Wright Prototype provided during the design and fabrication of the scroll expander.

Finally I would like to extend these thanks to my family and friends for their endless mental support.

TABLE OF CONTENTS

	<u>Page</u>
1 INTRODUCTION.....	1
2 LOW TEMPERATURE ENERGY RECOVERY REVIEW	4
2.1 Organic Rankine Cycle Overview	5
2.1.1 Cycle Configurations	5
2.1.2 Working Fluids	11
2.1.3 Irreversibility.....	13
2.1.4 Cycle Improvements	14
2.1.5 Applications	15
2.2 Alternative Solutions	16
2.2.1 Kalina Cycle	17
2.2.2 Transcritical CO ₂ Cycle	19
2.2.3 Stirling Engine	20
2.2.4 Thermal Electric Generators.....	23
2.2.5 Comparison.....	24
2.3 Expander Overview.....	24
2.3.1 Turbine.....	25
2.3.2 Reciprocating Piston	27
2.3.3 Rotary Vane	28
2.3.4 Rolling Piston	30
2.3.5 Gerotor	31
2.3.6 Scroll	32
2.3.7 Comparison.....	35

TABLE OF CONTENTS (Continued)

	<u>Page</u>
3 EXPANDER SELECTION AND DESIGN.....	38
3.1 Design Conditions	38
3.2 Scroll Compressor Selection	38
3.1.1 Scroll Compressor Description.....	39
3.3 Review of Previous Designs	42
3.3.1 1 st Design Iteration.....	42
3.3.2 2 nd Design Iteration.....	44
3.4 Transmission Configuration Selection	44
3.4.1 Direct Drive	44
3.4.2 Roller Chain.....	46
3.4.3 Helical Spur Gears.....	47
3.4.4 Helical Gear-Chain Hybrid.....	48
3.4.5 Spherical Miter Gears	49
3.4.6 Comparison and Selection	50
3.5 Transmission System Development.....	52
3.5.1 Spherical Miter Gears	52
3.5.2 Reaction Force Calculations.....	53
3.5.3 Bearing Selection	53
3.5.4 Vertical Bearing Holder Design	54
3.5.5 Horizontal Bearing Holder Design.....	55
3.5.6 Power Takeoff Shaft Design.....	55
3.5.7 Shaft Seal	56

TABLE OF CONTENTS (Continued)

	<u>Page</u>
3.5.8 Connections	57
3.5.9 Balancing.....	58
3.6 Lubrication System Development.....	59
3.6.1 Gear Lubrication	60
3.6.2 Scroll Lubrication	61
3.6.3 Lubrication System Validation	62
3.7 Seal Piston Engagement	64
3.8 Part Modifications	64
3.8.1 Tube Assembly.....	64
3.8.2 Top Cover.....	65
3.9 Final Design.....	66
4 EXPERIMENTAL SETUP	68
4.1 Modified Organic Rankine Cycle Test Bed.....	68
4.2 Heat Activated Cooling System.....	69
5 DATA REDUCTION AND UNCERTAINTY.....	71
6 RESULTS AND DISCUSSION	72
7 CONCLUSION.....	82
8 FUTURE WORK.....	83
9 BIBLIOGRAPHY	83
10 APPENDICES.....	89

LIST OF FIGURES

<u>Figure</u>	<u>Page</u>
1. Levelized energy cost to produce electricity from different sources [5]. Levelized includes the capital cost of the building and operational costs but not incentives.....	2
2. Carnot efficiency as a function of T_{hot} with a T_{cold} of 25°C.	4
3. Different types of working fluids and the shape of their saturated vapor line on a T-s diagram.	6
4. Component diagrams of a basic ORC (left) and a regenerative ORC (right).	8
5. T-s diagram for a w1 cycle with wet expansion (left). T-s diagram for a w2 cycle where point 3 lies in the superheated region (right).	9
6. T-s diagram of a d1 ORC with a dry working fluid where at the expander outlet the fluid is superheated (left). T-s diagram of an s1 ORC where the fluid is pressured to become supercritical (right).	10
7. Sensitivity analysis of a regenerative ORC with varying expander efficiency, evaporator temperature, and condensing temperature. Baseline conditions are condenser=40°C, evaporator=120°C, and isentropic efficiency=60% [19].	15
8. Component diagram of a Kalina cycle.	17
9. Temperature profile through an evaporator pure fluid (left) and azeotropic (right) [24].	18
10. T-s diagram for a transcritical CO ₂ cycle [26].	20
11. Qualitative P-v and T-s diagrams for a Stirling engine.	21
12. Illustration of the different thermodynamic states of the Stirling cycle and a component diagram [29].	22
13. The arrangement of the P and N type semiconductors in a TEG [7].	23
14. Impulse turbine (left), reaction turbine (middle), and radial inflow (right).	25
15. Different processes of a reciprocating piston [35].	27
16. Rotary vane expander with intake (1), expansion (2-3), and exhaust (4). Leakage and friction are the primary causes for loss in performance RVE.	29
17. Rolling piston expander with intake (1), expansion (2-3), and exhaust (4).	30

LIST OF FIGURES (Continued)

<u>Figure</u>	<u>Page</u>
18. Gerotor expander with intake (1) and expansion (2). Not all steps are shown due to the complexity of the motion between the rotor and stator. They both rotate in the same direction.	32
19. Scroll expander with fixed and orbiting scroll shown. Intake (1), expansion (2-5), and exhaust (6).....	33
20. This shows the two passages for leakage in a scroll assembly [44]......	34
21. Scroll compressor exploded (left) and assembled (right) views.	40
22. Scroll sealing piston with high pressure highlighted in red and relative movement in blue.	41
23. Lubrication system for scroll compressor.	41
24. 1 st generation scroll expander (left) and 2 nd generation (right). Both are not on the same scale.....	43
25. Direct drive section view, expander top and compressor bottom (left). Isometric view (right).....	45
26. Partial section view of chain drive (left). Chain configuration 1 (top-right) and 2 (bottom-right). The wheels with the black center are the expander and compressor and the white center is the idler. The chain configuration of the section view is type 1.	46
27. Partial section view of helical gear drive (left). Gear configuration 1 (top-right) and 2 (bottom-right). The gears with the black center are the expander and compressor while the ones with white centers are idlers. The gear configuration of the section view is type 2.....	48
28. Interaction between chain and gear components. The top and side views are shown respectively. The orange shafts designate the compressor and expander and the blue is an idler shaft.	49
29. Partial section view of miter gear drive.	50
30. Spherical miter gear nominal dimensions [mm]. The 40 [mm] represents the mounting distance which is how far the gear should be from the center of the mating gear.	53

LIST OF FIGURES (Continued)

<u>Figure</u>	<u>Page</u>
31. Nominal dimensions of the 6201 (left) and W6205 (right) bearings. All dimensions are in [mm].	54
32. Power takeoff shaft comparison original (left) and revision (right). All units are [in].	55
33. Extensive wear caused by a Teflon shaft seal on the original power takeoff shaft.	56
34. Shaft seal in the bottom cover with washer for unsupported span (left) and failure caused by excessive pressure (right).	57
35. Shaft assembly sent to OTS Wire for balancing.	59
36. Lubrication methods; the black center represents a drive shaft.	60
37. Bottom cover assembly with horizontal miter gear, artificial sump, power takeoff shaft, and main shaft. It also shows the oil height in the bottom cover as well as oil flow into the shafts oil pump.	61
38. Artificial sump and section view of artificial sump and shaft.	62
39. Extensive wear to orbiting scroll caused by insufficient lubrication.	62
40. Qualitative oil mass flow rate out of the shaft as a function of shaft speed. Solid shapes signify that an impeller was used. In the legend the number represents the height of the oil in the bottom cover (refer to Fig. 37 for reference).	63
41. Changes made to the 2 nd generation expander housing. 2 nd generation (left) and 3 rd generation (right). All units are in [in].	65
42. Changes made to the 1 nd generation expander top cover. 1 nd generation (left) and 3 rd generation (right). All units are in [in].	65
43. Expander assembly built and partial section.	67
44. Expander lubrication system (left) and shaft assembly (right).	67
45. Diagram of the ORC Test Bed.	68
46. Component diagram of the HAC system.	70

LIST OF FIGURES (Continued)

<u>Figure</u>	<u>Page</u>
47. Expander isentropic efficiency as a function of break-in period with $Pr=4\pm 0.2$. The speed was not kept constant. Each data set is given in chronological order for the date of data collection.....	73
48. The data for 1/28/2010 and 2/16/2010 was taken with the damaged shaft and the 3/17/2010 is taken with the new shaft. The changes are highlighted in Fig. 32. The data for 3/17/2010 has only 3 hours of cumulative break-in.	74
49. Expander efficiency versus shaft speed for 3 rd generation expander.....	75
50. Expander power output versus speed as well as mass flow rate versus speed.	76
51. Expander isentropic efficiency as a function of pressure ratio. Speed is mostly kept constant but to achieve a high pressure ratio the speed had to be decreased. The 7/23/2007 data is extracted from [48].	77
52. Counterclockwise: Ideal expansion, under-expansion, and over-expansion. Points 3-4 represent expansion.	78
53. Showing the relationship between EM_{ratio} and pressure ratio. The ideal expansion for the case data is represented by the dot on the dashed line.	80
54. Isentropic efficiency as a function of EM_{ratio} . The Gerotor and Scroll C data is taken from Mathias et al. [42].	81

LIST OF TABLES

<u>Table</u>	<u>Page</u>
1. International energy production by source in 2005 [2].	1
2. Summary of thermophysical properties of different refrigerants [12].	12
3. Summary of atmospheric lifetime, GWP, and ODP of different fluids [14].	12
4. Kalina cycle and ORC simulation with a geothermal source at 90°C [25].	19
5. Summary of operating conditions and performance of different expander types.	37
6. List of assumptions for Table 5.	37
7. Design requirements for the scroll expander and preliminary test conditions.	38
8. Summary of scroll characteristics.	39
9. Figure references for description of designs.	42
10. House of quality for comparison of the helical spur gear, helical gear-chain hybrid, and spherical miter gear designs.	51
11. Summary of spherical miter gear characteristics where R and L represent teeth direction.	52
12. Design stage uncertainties of several quantities for each test bed.	71

LIST OF APPENDICES

	<u>Page</u>
Appendix A: Engineering Calculations	90
A.1 Counterweight Calculations	91
A.2 Reaction Force Calculations	92
A.3 Bearing Life	94
A.4 Minimum Thread Engagement.....	95
A.5 Top Cover Bolts.....	96
A.6 Bottom Cover Bolts	97
A.7 Vertical Bearing Holder Bolts	97
A.8 Horizontal Bearing Holder Bolts	98
A.9 Set Screw	98
A.10 Dowel Pins	99
A.11 Design Stage Uncertainty	99
Appendix B: Finite Element Analysis	102
B.1 Vertical Bearing Holder.....	103
B.2 Horizontal Bearing Holder	104
B.3 Top Cover.....	106
B.4 Tube Assembly.....	108
B.5 Bottom Cover.....	111
Appendix C: Engineering Drawing	112

LIST OF APPENDIX FIGURES

<u>Figure</u>	<u>Page</u>
55. Free body diagram of the position of the different components in the balancing calculation.	91
56. Free body diagram of reaction forces on the shaft and power takeoff.....	94
57. From left to right and top to bottom. Factor of safety plot based on a yield strength of 185 [Mpa] with ISO clipping, stress plot, strain plot, displacement plot, and mesh.	104
58. From left to right and top to bottom. Factor of safety plot based on a yield strength of 460 [Mpa] with ISO clipping, stress plot, strain plot, displacement plot, and mesh.	106
59. From left to right and top to bottom. Factor of safety plot based on a yield strength of 206.8 [Mpa] with ISO clipping, Stress plot, strain plot, displacement plot, and mesh....	108
60. FEA analysis of the tube assembly. Top to bottom and left to right: Stress plot, strain plot, displacement plot, mesh, and factor of safety distribution with ISO clipping based on a yield strength of 206.8 [Mpa].	110

LIST OF APPENDIX TABLES

<u>Table</u>	<u>Page</u>
13. Summary of fixed and calculated parameters for the design of the counterweights.....	92
14. Summary of bearing reaction forces shown in Fig. 56. All forces are in [N].	93
15. Summary of pressure force information for top cover.....	96
16. Summary of important quantities in calculating bolt load factor.....	96
17. Summary of factors of safety for the top cover under varying scenarios.	97
18. Summary of bolt reaction results from Solidworks Simulation for the vertical bearing holder.	97
19. Summary of bolt reaction results from Solidworks Simulation for the horizontal bearing holder.	98
20. Detailed uncertainty summary of torque sensor in the HAC test bed. The rated output (R.O.) is 5VDC. Temperature effects are not included because we are operating within the compensated range of the device.	99
21. Summary of equipment bias uncertainty.	100
22. Summary of nominal and perturbed values used in the enthalpy uncertainty calculation.	100
23. Summary of perturbed, nominal, and overall uncertainty for ORC and HAC test beds. .	101
24. Summary of mesh and solver information from Solidworks Simulation for the vertical bearing holder.....	103
25. Summary of mesher and solver information from Solidworks Simulation for the horizontal bearing holder.....	105
26. Summary of mesh and solver information from Solidworks Simulation for the top cover	107
27. Summary of mesh and solver information from Solidworks Simulation for the tubing assembly.....	109
28. Bill of materials.....	113

1 INTRODUCTION

It was during the early 1800s that mankind first discovered how to harness the power of heat and put it to work. The critical component that facilitated this process was the expander. Today, its most common incarnations are the turbine and piston which are respectively dynamic and positive displacement types. These devices and their respective power cycles have harnessed over 150 years worth of inexpensive energy. Sadi Carnot (1796-1832) said it best in his “Reflection of The Motive Power of Heat,”

“To take away to-day from England her steam engines would be to take away at the same time her coal and iron. It would be to dry up all her sources of wealth, to ruin all of which her prosperity depends, in short, to annihilate that colossal power [1].”

The vast majority of our transportation, homes, and industries still rely on some form of fossil fuel that is burned and converted into electrical-mechanical power. Fossil fuels account for 86.2% of all energy production in the world [2]. Table 1 gives a breakdown of the energy production worldwide.

Table 1: International energy production by source in 2005 [2].

	Quadrillion Btu	Percent %
Coal	122.07	26.6
Crude Oil	157.65	34.3
Natural Gas	104.75	22.8
Natural Gas Plant Liquids	11.47	2.5
Nuclear	27.54	6.0
Hydroelectric	28.98	6.3
Geothermal	6.88	1.5
Total	459.34	100

The consumption of energy by source for the U.S. closely follows the international percentages above. The U.S. consumes close to 100 Quadrillion [Btu] (1.06×10^{20} Joules) of energy each year [2]. This number does not constitute the actual amount that becomes usable work. As with all processes the conversion of chemical to electrical energy has

inherent losses and limitations. One limitation is the Carnot efficiency. It dictates the maximum efficiency that any thermodynamic cycle can achieve. For this reason we lose 25.81 of the 40.67 quadrillion [Btu] of energy that is consumed to produce electricity in the U.S. each year [2]. That translates into a conversion efficiency of 36.5%.

There are also environmental considerations. After combustion hydrocarbons (HC) produce several pollutants such as carbon dioxide, carbon monoxide, nitrogen oxides, unburned HC, and sulfur oxides. These byproducts have led to several consequences such as global warming, ocean acidification, acid rain, and many other hazardous effects to both the environment and mankind [3].

Fossil fuels do have advantages which include high energy density, abundance, and low cost. Octane has a 40 fold advantage in energy density when compared to a lithium ion battery [3], [4]. If an internal combustion engine was only 10% efficient the fuel would still have four times higher energy density than a chemical battery. They additionally have one of the lowest costs in [\$/MWh] which can be compared to other energy sources in Fig. 1.

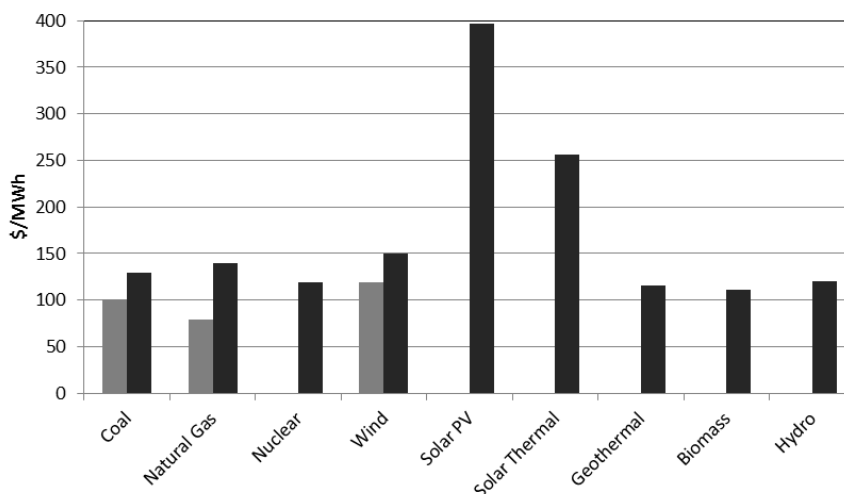


Fig. 1: Levelized energy cost to produce electricity from different sources [5]. Levelized includes the capital cost of the building and operational costs but not incentives.

Current trends show that fossil fuel consumption is forecasted to increase over the next 20 years [2]. Moving forward we need to research new energy technologies that can decrease our dependence on fossil fuels. We also need to improve the efficiency of the cycles that consume them. Low temperature Rankine cycles are a potential technology that

could facilitate both of these aspects. The most common form being the organic Rankine cycle (ORC). They have a wide variety of applications that include power generation, powering reverse osmosis pumps, and heat activated cooling. The cycle is compatible with a variety of heat sources such as exhaust, industrial process waste heat, geothermal, biological waste, and the sun.

The purpose of this work was to develop a high efficiency scroll expander for use in an ORC. The expander is a crucial component in the power cycle. The efficiency, power, and nominal operation were amongst the most important aspects of its design. It is of interest to this work to provide an overview of Rankine cycles as well as alternative methods to recover energy at low temperatures. An extensive comparison of different types of expanders for low temperature applications will also be given. The scroll expander design and its evolution will be described. The test bed, results, and recommendations for future work will be presented.

2 LOW TEMPERATURE ENERGY RECOVERY REVIEW

Low temperature energy recovery by thermal cycles is limited by the Carnot efficiency. This describes the maximum efficiency that any heat engine can achieve given two thermal reservoirs. This efficiency is described by the difference in temperature between the two reservoirs and is given as

$$\eta_{Carnot} = \frac{T_{Hot} - T_{Cold}}{T_{Hot}} \quad (1)$$

where T_{Hot} is the average temperature of the heat source and T_{Cold} is the average temperature of the rejection sink. With a decreasing hot side temperature the efficiency becomes more sensitive to changes in temperature. This is the region between the two orange points in Fig. 2 and can be described as the regime for both low and medium quality heat sources. Recovery at these low temperatures will result in a low thermal efficiency of the cycle but the energy is generally free.

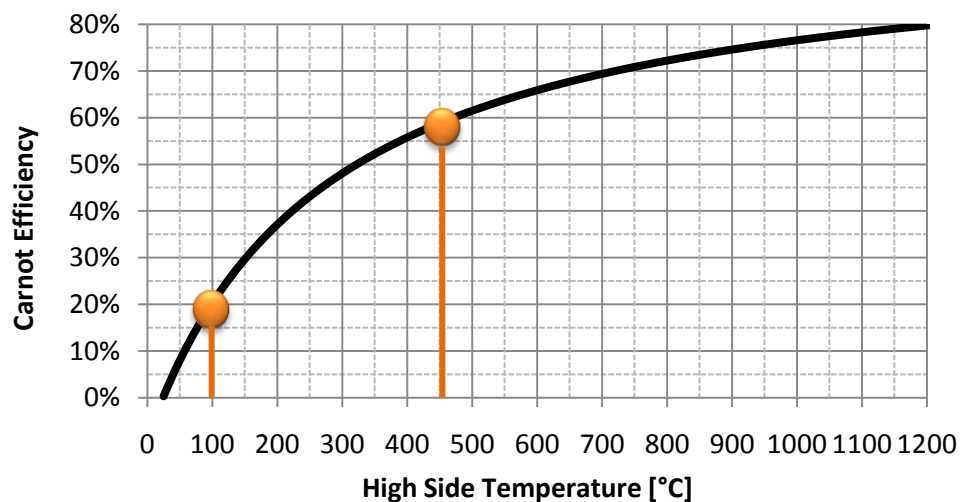


Fig. 2: Carnot efficiency as a function of T_{hot} with a T_{cold} of 25°C.

Low temperature sources can be described by their grade and are broken up into low, medium, and high. The actual definitions are not well defined but can generally be categorized with 80-150°C for low, 150-500°C for medium [6], and anything above 500°C as

high. With this fundamental understanding of low energy recovery and its limitations a review of different Rankine cycle configurations, working fluids, losses, and cycle improvements will be presented. Alternatives to the ORC will also be presented along with an overview of different expander types.

2.1 Organic Rankine Cycle Overview

The Rankine cycle is a mature technology that has been refined for over 150 years. It is a closed cycle that is composed of a pump, evaporator, expander, and condenser. These components are well standardized and commercially available. Even though the cycle is covered in most thermodynamic textbooks it is of interest to this thesis to present a review of the different configurations of this cycle. The Rankine cycle is a closed vapor power cycle. It takes advantage of the small amount of work required to pump a liquid [7] and the amount of energy that can be extracted from latent heat. An ORC differs from the basic Rankine cycle in that the working fluid is organic. Sahar et al. [8] modeled 31 different working fluids in different ORC configurations. Types of organic working fluids modeled included alkanes, fluorinated alkanes, ethers and fluorinated ethers. These fluids can behave differently when used in an ORC and it is important to discuss the different configurations and working fluid characteristics together. Organic working fluids have performance advantages over water-steam at low power levels but these advantages disappear at 300 [kW] or more because of the poor heat transfer properties of organic fluids [7].

2.1.1 Cycle Configurations

Different fluid types can be classified by the shape of their saturated vapor line in a T-s diagram. The slope of the line dT/ds can have a positive, infinite, or negative slope and are respectively dry, isentropic, and wet fluid types. The general shape of these different fluid types in a T-s diagram is shown in Fig. 3.

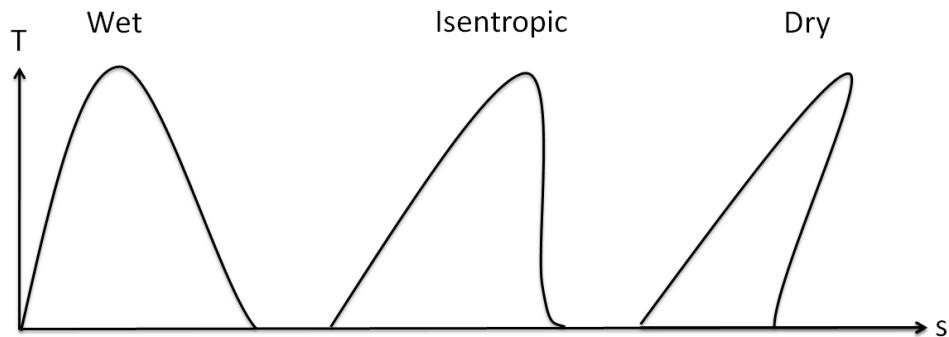


Fig. 3: Different types of working fluids and the shape of their saturated vapor line on a T-s diagram.

Wet and isentropic fluids have a bell-shaped curve while dry fluids have an overhang. We will classify wet fluids with “w-,” isentropic fluids with “i-,” and dry fluids with “d-.” Beyond fluid type cycles can be classified by the pressures they operate during heat addition. Most common are subcritical pressures where the working fluid changes phase from a liquid to a vapor. A cycle can also operate at supercritical pressures and no phase change will occur during heat addition. With these concepts we can now define the different cycle configurations.

Two different component diagrams have been illustrated in Fig. 4 for reference. The most common forms of the ORC are the basic and the regenerative cycles. In a regenerative cycle the useful heat is recovered from the expansion process and cycled back into the working fluid after the pump. The different processes within the ORC are described by the following relationships.

Pump 1 → 2: the amount of work required by the pump is given by

$$\dot{W}_p = \frac{\dot{m}(h_1 - h_{2s})}{\eta_p} \quad (2)$$

where \dot{m} is the working fluids mass flow rate, h_1 and h_{2s} are the enthalpy and isentropic enthalpy at the pump inlet and outlet respectively, and η_p is the isentropic efficiency of the pump.

Evaporator 2 → 3: the amount of heat taken up by the working fluid in the evaporator is given by

$$\dot{Q}_E = \dot{m}(h_3 - h_2) \quad (3)$$

where h_2 and h_3 are the enthalpies before and after the evaporator.

Expander 3 → 4: the amount of work that is extracted for the working fluid by the expander is given by

$$\dot{W}_E = \dot{m}(h_3 - h_{4s})\eta_E \quad (4)$$

where h_3 and h_{4s} are the enthalpy and isentropic enthalpy at the expander inlet and outlet respectively, and η_E is the isentropic efficiency of the expander. Equation (4) can be rearranged to solve for η_E .

Condenser 4 → 1: the amount of heat that is rejected to the environment from the working fluid is given by

$$\dot{Q}_C = \dot{m}(h_4 - h_1) \quad (5)$$

where h_4 and h_1 are the enthalpies at the inlet and exit of the condenser respectively. The performance of an ORC is measured by the thermal efficiency which is described by

$$\eta_T = \frac{\dot{W}_E - \dot{W}_P}{\dot{Q}_E} = \frac{(h_3 - h_4) - (h_2 - h_1)}{h_3 - h_2} \quad (6)$$

where the different enthalpies are taken at their respective state points. The quantity is the work extracted by the expander minus the work required to drive the pump for a specific heat input.

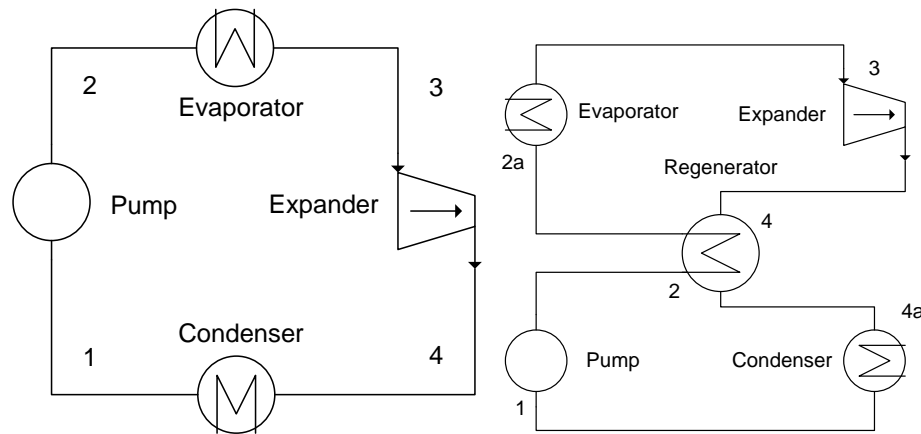


Fig. 4: Component diagrams of a basic ORC (left) and a regenerative ORC (right).

Next we describe how the characteristics of the different types of working fluids effect the cycle configuration. All of the cycles should be thought of as basic Rankine cycles unless described differently.

w1: The T-s diagram for this wet fluid is represented in Fig. 5. The fluid leaves the condenser as a saturated liquid at state point 1. It is at temperature T_1 and pressure P_{\min} . The fluid is compressed in the pump from 1→2 to a subcritical pressure P_{\max} . Heat is added at constant pressure in the evaporator from 2→3. The saturated vapor at the expander inlet is expanded to pressure P_{\min} and produces work. After expansion the fluid lies within the two phase region of the vapor dome which is why the fluid is defined as wet. The remaining heat is then rejected to the environment at T_1 in the condenser from 4→1 until the fluid has become a saturated liquid.

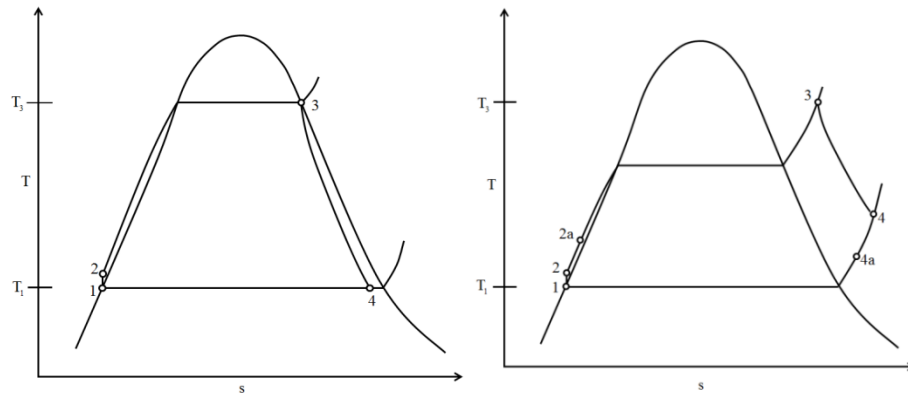


Fig. 5: T-s diagram for a $w1$ cycle with wet expansion (left). T-s diagram for a $w2$ cycle where point 3 lies in the superheated region (right).

$w2$: We will now consider an ORC that achieves superheat. A T-s diagram of the cycle is shown in Fig. 5 (right). The processes of this cycle are the same as that of $w1$ except in the evaporator. After the fluid is pumped to subcritical pressures it is heated at constant pressure until it becomes a saturated vapor. It is then heated further to become a superheated vapor at state point 3. The fluid is then expanded and performs work. After expansion the fluid still remains in the superheated region. Note that in each diagram in Fig. 5 a vertical line from 3 to 4 would indicate an isentropic expansion process. However, the 3 to 4 process slants off to the right showing an expansion process having an isentropic efficiency less than 100%.

$i1$: This cycle goes through the same processes at $w1$ but during expansion the working fluid follows the saturated vapor line. After expansion the fluid remains as a superheated vapor. It should be noted that the fluid may enter the two phase region inside the vapor dome as a high quality vapor.

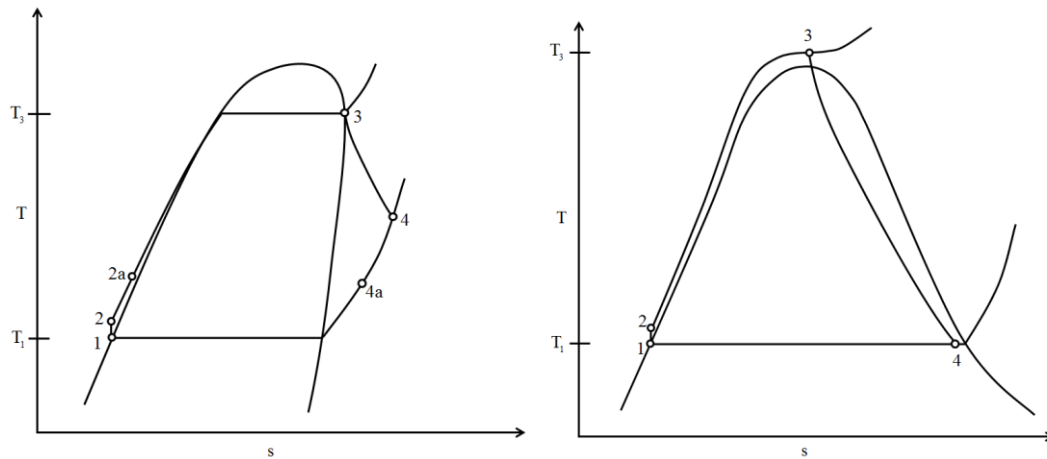


Fig. 6: T-s diagram of a d1 ORC with a dry working fluid where at the expander outlet the fluid is superheated (left). T-s diagram of an s1 ORC where the fluid is pressured to become supercritical (right).

d1: We will now consider a cycle with a dry fluid. It is represented in a T-s diagram in Fig. 6. The processes that the cycle goes through are the same as *i1*. The main difference being that after expansion at state point 4 the fluid must be in the superheated region due to the negative slope of the saturated vapor line.

d2: This cycle follows the same processes as *d1* but state point 3 is in the superheated region. In this respect the cycle is like *w2*.

s1: Unlike the previous cycles it operates at supercritical conditions from process 2→3. By operating at supercritical conditions this cycle aims to reduce the exergy destruction within evaporator caused by the mismatch between the heat source and working fluid [9]. This cycle is described by its T-s diagram in Fig. 6. This cycle is characteristic of *w*-type fluids because point 4 lies within the vapor dome.

s2: This cycle is the same as *s1* but after expansion the fluid is still in the superheated region. This cycle is characteristic of *i*- and *d*- fluids.

Comparing *w2*, *i1*, *d1*, *d2*, and *s2* we notice that the temperature after expansion, T_4 , is higher than the pump inlet T_1 . If this temperature gradient is sufficiently large a regenerator which is shown in Fig. 4 (right) can benefit the performance of the cycle. If the working fluid is dry a regenerator may be required in order to avoid significant losses in the cycle's efficiency [7]. This device recovers sensible heat from the superheated vapor in

4→4a and transfers it into the pressurized liquid in 2→2a. The amount of heat transferred is described by

$$\dot{Q}_R = \dot{m}(h_{2a} - h_2) = \dot{m}(h_4 - h_{4a}) \quad (7)$$

where h_2 , h_{2a} , h_4 , and h_{4a} follow their respective state points. The additional state points 2a and 4a are shown in Fig. 5 (left) and Fig. 6 (right). With the addition of this component the thermal efficiency of the cycle is now described by

$$\eta_T = \frac{\dot{W}_E - \dot{W}_P}{\dot{Q}_E} = \frac{(h_3 - h_4) - (h_2 - h_1)}{h_3 - h_{2a}} \quad (8)$$

where the enthalpy values are represented by their respective state points.

The regenerator is most commonly used with dry working fluids [10]. It allows for better utilization of the heat source as it is recovered internally within the cycle. Secondly, it raises the average temperature at which heat is absorbed and rejected by the cycle, which results in an increase in the thermal efficiency in accordance with Eq. (1) [8]. The regenerator can have a negative impact on the cycle if it causes a significant pressure drop. It also increases the cost of the system. For isentropic fluids the expansion ends very close to the saturated vapor line and the recovery of any sensible heat has a small impact on the overall performance [10], [11].

2.1.2 Working Fluids

Beyond the different fluid types and cycle configurations organic fluids have additional properties that are important to consider. Properties such as boiling temperature, latent heat, critical point, and stability temperature are all important in ensuring good thermodynamic performance. It also has effects on the expander type used as in the case of small turbines a high molecular weight is desired to maintain a high and optimal Reynolds number [7]. A low critical point is useful when *s*-type cycles are considered. Boiling temperature and stability temperature are important when choosing a fluid for the heat source. Thermophysical properties of several refrigerants are summarized in Table 2.

Table 2: Summary of thermophysical properties of different refrigerants [12].

Fluid		Type	Molecular Weight [g/mol]	Critical Point [C°] / [bar]	Boiling Temp. [C°]	Latent Heat @ 1 atm. [kJ/kg]
Water	H ₂ O	<i>w</i>	18.02	374 / 220.6	100	2257
Ammonia	CF ₃ -CH ₂ F	<i>w</i>	17.03	132.3 / 113.3	-33.3	1370
R11	CCl ₃ F	<i>i</i>	137.4	198 / 44.1	23.8	180.3
R123	C ₂ HCl ₂ F ₃	<i>i</i>	170.6	183.7 / 36.7	27.8	170.6
R134a	C ₂ H ₂ F ₄	<i>w</i>	217	101 / 40.6	-26.1	217
R245fa	C ₃ H ₃ F ₅	<i>i</i>	134	154 / 36.5	15.2	196
R601	C ₅ H ₁₂	<i>d</i>	357.8	196.5 / 33.4	35.9	357.8
n-hexane	C ₆ H ₁₄	<i>d</i>	86.17	234.7 / 30.6	69.27	329.9

Beyond thermodynamic performance a working fluid should be benign to the environment and its inhabitants. This is why toxicity, flammability, material compatibility, global warming potential (GWP), ozone depletion potential (ODP), and atmospheric lifetime are important factors. In general refrigerants have a low toxicity [13]. Some of these properties for different fluids are summarized in Table 3.

Table 3: Summary of atmospheric lifetime, GWP, and ODP of different fluids [14].

Fluid	Lifetime [years]	GWP 20 years	GWP 100 years	ODP
CO ₂	-	1	1	-
R11	45	6,730	4,750	1
R22	12	5,160	1,810	0.055
R123	1.3	273	77	0.02
R134a	14	3,830	1,430	-
R152	0.6	187	53	-
R245fa	7.6	3,380	1,030	-

It should be noted that all HCFC refrigerants are scheduled to be phased out by 2030. Most CFCs are already banned. This makes these fluids poor choices as long term candidates for working fluids.

An observation that can be made from Table 2 is that as a general rule most fluids with simpler molecules have lower critical temperatures. These substances also tended to be *w*- or *i*- types. Complex molecules in comparison have higher critical temperatures and tend to be *d*- fluids [8], [11].

Sahar et al. [8] found that fluids with low critical temperatures had a low thermal efficiency when evaporated at subcritical conditions. With supercritical conditions the substances exhibited a significant increase in efficiency. They noted that the low critical point of organic fluids makes the supercritical ORC a practical solution.

In subcritical conditions Sahar et al. [8] noticed that superheating *w*- and *i*- fluids gave a slight increase in thermal efficiency. More significant gains are achieved through the use of both superheat and a regenerator. Strangely *d*- working fluids showed a decrease in thermal efficiency with superheat. No explanation was given but this behavior was also observed by Pedro et al. [15] and Mago et al. [16]. They both noted that superheat would cause an increase in second law irreversibilities and for maximum performance the cycle should be operated at saturated conditions. Our ORC EES model did not show this behavior and as would be expected an increase in superheat increased the thermal efficiency. A deeper analysis of how these authors calculated their thermal efficiency is required to fully understand this counterintuitive behavior.

In closing Sahar et al. [8] recommended R236ea, R245ca, R245fa, R600, R600a, R601a, RE134, and RE245 as working fluids in ORCs. Borsukiewicz-Gozdur et al. [17] recommended both R245fa and R235ea as working fluids. Mago et al. [16] concluded that *d*- working fluids such as R113, R123, R245ca, R245fa, and isobutane achieved better performance than *w*- working fluids such as R134a and propane. Fluids with higher boiling temperatures showed better performance [15], [16].

2.1.3 Irreversibility

As with any process the ORC has inherent irreversibilities. This can come in the form of friction-heat losses in the expander and pump. This is accounted in the isentropic efficiencies of each device. Pressure drops in heat exchangers, valves, and pipes are another source. The largest source of irreversibility in the system is caused by the evaporator [13]. This is caused by a temperature mismatch between the working fluid and the heat source. Organic working fluids due to their low latent heat match the source temperature profile better than water-steam [18].

Practical considerations also exist in an ORC. The liquid entering the pump should be sub-cooled to prevent cavitation. When using turbines with *w*- type working fluids the fluid should be superheated to prevent droplet formation during expansion. In practice the quality at the turbine exit is kept above 90% [4]. Both cavitation and high speed droplets will erode the pump and turbine blades respectively.

2.1.4 Cycle Improvements

Once a cycle configuration and fluid have been specified there are a limited number of ways to improve the thermal efficiency of the cycle. One approach is to increase the average high side temperature or decrease the average low side temperature. In low temperature energy recovery the high side temperature is fixed and decreasing the condensing temperature below atmospheric conditions is impractical. Other approaches include increasing the isentropic efficiencies of the pump and expander. In a Rankine cycle the pump work is significantly less than the expander work. This means that improving the efficiency of the expander will provide the greatest degree of cycle improvement.

Badr et al. [19] modeled an ORC and performed a sensitivity study to show which of these parameters had the greatest effect on thermal efficiency. They varied the isentropic expander efficiency, evaporator temperature, and condenser temperature. They modeled both a basic and regenerative ORC with R113 as the working fluid. Their findings are shown in Fig. 7.

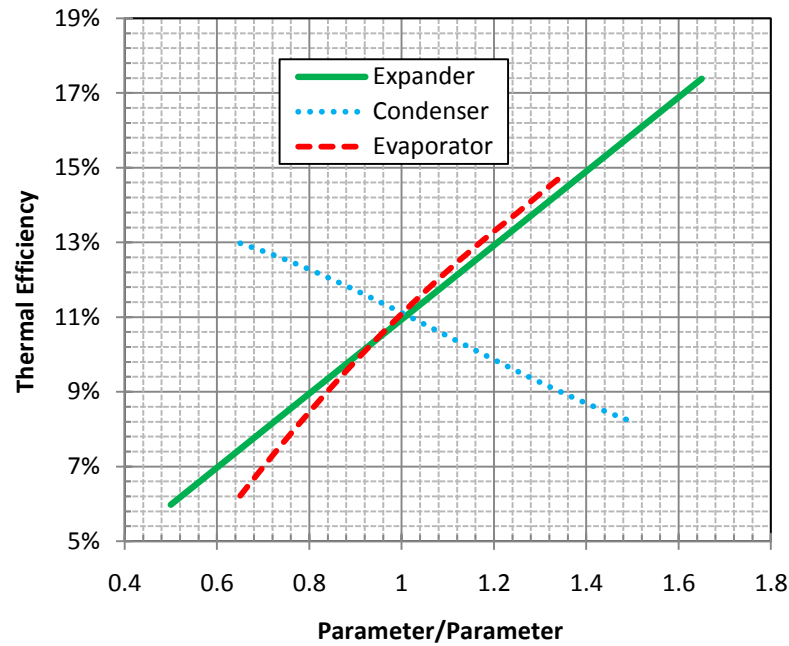


Fig. 7: Sensitivity analysis of a regenerative ORC with varying expander efficiency, evaporator temperature, and condensing temperature. Baseline conditions are condenser=40°C, evaporator=120°C, and isentropic efficiency=60% [19].

The evaporator temperature and the expander efficiency are both important parameters in optimizing a ORCs performance. They noted that the expander efficiency was the most important parameter in low temperature energy recovery and that great care should be taken during expander selection in order to maximize cycle efficiency.

2.1.5 Applications

The ORC is a versatile cycle due, in part, to the large number of working fluids that can be chosen to match the heat source. It is one of the few technologies that has proven itself for power levels from a few [kW] to multi [MW] sizes [10]. It has been used to produce electrical power through geothermal, solar thermal, industrial heat, and biogas sources. Some innovative applications include mechanically driving a reverse osmosis (RO) pump for desalination [20], [21] or a compressor for heat activated cooling [22]. This is a brief review of these applications.

Power Generation: The production of electricity is commonplace and there are many ways that the ORC can be used in its production. Geothermal power plants generally operate around 80°C to 120°C which is why the ORC is preferred over conventional methods [10]. An example of a geothermal plant is the Neustadt-Glewe in Germany. The hot water loop is at 98°C which is used to heat the organic working fluid which drives the turbine [10]. Generally geothermal plants produce power into the MW range.

Solar insolation is another heat source than can be used in the production of electricity. Saitoh et al. [23] modeled a small ORC which utilized a 200°C heat source from a solar collector. They envisioned the system to be used for distributed power for combined heating and power (CHP). This would reduce the losses that occur from transmitting power over large distances.

Desalination: Clean drinking water is one of the most precious resources on the planet and in many places it is scarce. A solution to combat this problem is the desalination of seawater. The most common approach is achieved through phase change methods [10]. A more efficient method is RO which uses a high pressure pump along with a permeable membrane to separate the salt and water. In this application the work from the ORC is used to mechanically or electrically drive the pump. The advantage of mechanically driving the pump is the reduction in series losses. Manolako et al. [20] successfully fabricated a combined ORC-RO system. The cycle operated at low temperatures ranging from 40°C to 70°C. The thermal efficiency of the cycle was approximately 5%.

Heat Activated Cooling: There are scenarios when there is a need for cooling and a waste heat source in close proximity. One such case is refrigerated trucking. The heat from the exhaust is used to power an ORC which in turn powers a vapor compression cycle. A heat activated cooling system was fabricated by Wang et al. [22] that used R245fa as the working fluid. Their system achieved 4.4 [kW] of cooling with a COP of 0.48.

2.2 Alternative Solutions

The ORC is not the only method available for low temperature heat recovery. There are several alternatives that include the Kalina cycle, transcritical cycle, Stirling engine, and thermal electric generator (TEG). Both the Kalina and transcritical cycle are derivatives of the

Rankine cycle. The Stirling engine aims to mimic the reversible processes of the Carnot cycle. TEGs are not power cycles but devices that produce a voltage from a heat flux.

2.2.1 Kalina Cycle

The Kalina cycle is a modified absorption cycle. It is a relatively new cycle and has not had wide spread adoption. A component diagram of a Kalina cycle is given in Fig. 8. It is similar to a Rankine cycle but with the inclusion of a separator and absorber. The cycle is described below:

- 1 → 2: The sub-cooled is increased to P_{\max} .
- 2 → 3: The mixture is preheated by heat from the separation process.
- 3 → 4: The fluid is evaporated into a high temperature-pressure vapor.
- 4 → 5: The mixture is separated into a rich ammonia-water vapor.
- 4 → 6: The mixture is separated into a weak liquid ammonia-water mixture.
- 5 → 9: The mixture is expanded and produces work.
- 6 → 7: The hot liquid is used to preheat the mixture coming out of the pump.
- 7 → 8: The liquid mixture is throttled to a lower pressure.
- 8,9 → 10: The liquid and vapor are mixed.
- 10 → 1: The vapor mixture is cooled and condensed into a liquid at P_{\min} .

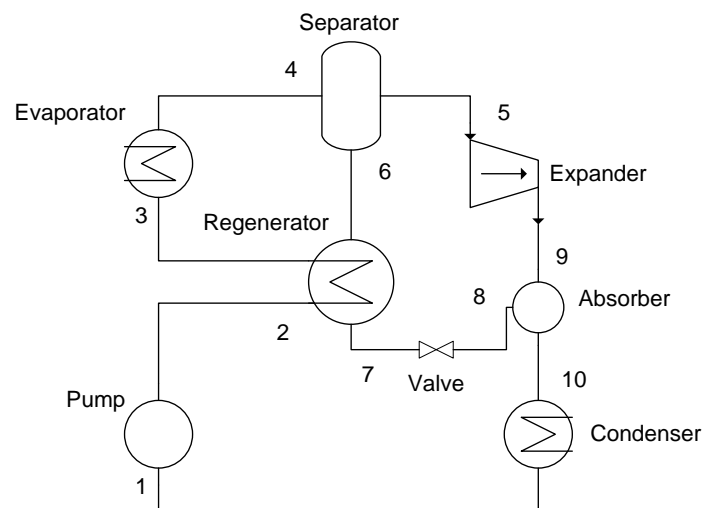


Fig. 8: Component diagram of a Kalina cycle.

There are several variations of this cycle with the inclusion of additional regenerators, condensers, and pumps. These variations can increase performance but can also hurt the overall efficiency of the cycle [8].

The main goal of this cycle is to reduce irreversibilities that occur within the heat exchangers by using an azeotropic working fluid like an ammonia-water mixture. Azeotropic fluids have non-isothermal boiling temperatures at constant pressures, and their boiling curves better match the temperature profile of heat sources. The temperature profiles of the working fluid and heat source in an evaporator are shown in Fig. 9.

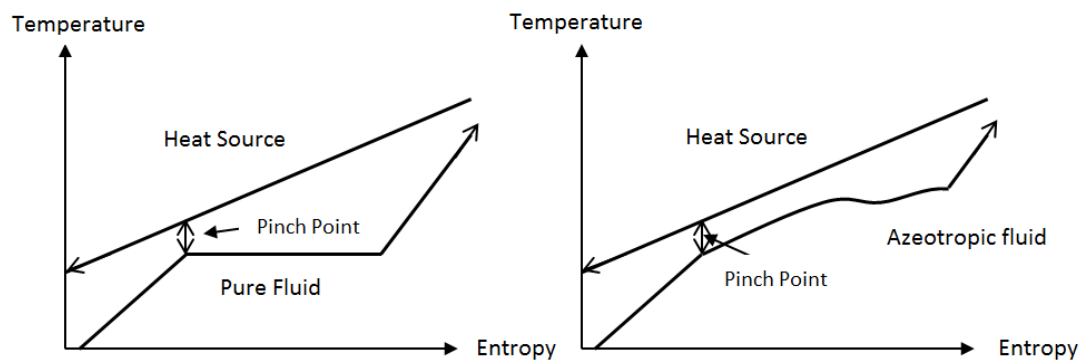


Fig. 9: Temperature profile through an evaporator pure fluid (left) and azeotropic (right) [24].

With a pure fluid the maximum temperature it can achieve before boiling is referred to as the “pinch point.” This causes a large mismatch between the temperature profiles and the area between them is representative of the amount of exergy destruction.

The decrease in irreversibilities should theoretically give the Kalina cycle an advantage over ORCs. Bombarda et al. [24] observed that a Kalina cycle only managed to offer marginal improvements over an optimized ORC but it required a more complex component layout. It provided large improvement in decreasing the irreversibility in the evaporator but its advantage was marginalized when the losses from the additional equipment were accounted for. For medium grade heat they stated that at a 100 [bar] the cycle components would have to be made of expensive materials to resist both the pressure and corrosive nature of ammonia-water mixtures. They also mentioned that the small temperature differential of the Kalina cycle can be problematic in that large heat exchangers are required to achieve the desired high side temperature.

Hettiarachchi et al. [25] modeled Kalina cycles with different ammonia-water mixtures and compared them to ORCs with ammonia and isobutene as working fluids. They found that the Kalina cycle provided better thermal efficiencies than the ORC for a given heat input. Their findings are summarized in Table 4.

Table 4: Kalina cycle and ORC simulation with a geothermal source at 90°C [25].

Cycle	Pressure [MPa]	η_T [%]	Ammonia Fraction	Working Fluid
Kalina	2.6	8.9	0.8	Ammonia-water
Kalina	3.3	10.5	0.95	Ammonia-water
ORC	0.9	7.3	N/A	Isobutene
Rankine	3.4	10	N/A	Ammonia

Both Kalina cycles outperformed the ORC with isobutene but the ORC with ammonia remained competitive. The low 90°C heat source gives the advantage of requiring only moderate pressure for the Kalina cycle. This would allow it to be fabricated with more cost effective materials.

2.2.2 Transcritical CO₂ Cycle

The primary differences between this cycle and a supercritical ORC are that it operates closer to the triple point and uses CO₂ as the working fluid. Operating close to the triple point decreases the amount of work required to compress the working fluid. A T-s diagram of the cycle is shown in Fig. 10 and a component diagram in Fig. 4 (right). The benefits of using CO₂ as a working fluid is that it is non-toxic, inert, abundant, inexpensive, and is environmentally friendly. In order to achieve supercritical conditions the P_{\max} of the cycle must be over 73.8 [bar]. The processes of this cycle are the same as that of an s2 cycle.

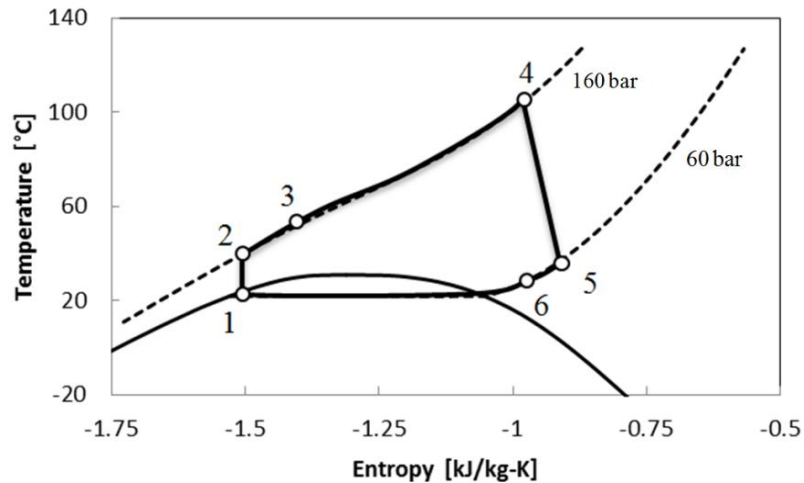


Fig. 10: T-s diagram for a transcritical CO₂ cycle [26].

This cycle like the Kalina cycle reduces the irreversibilities in the evaporator through better temperature matching of the heat source. Theoretically this cycle should achieve better performance than an ORC [27], [26]. Super critical fluids give better agreement with source temperature profiles than azeotropic fluids.

Chen et al. [26] modeled a transcritical CO₂ cycle with a 150°C heat source. They observed that it gave marginal improvements in performance over an ORC that used R123. The transcritical cycle operated at a P_{\max} of 160 [bar] which was described as an advantage because more compact components could be used. The high operating pressure also comes with the disadvantage of requiring thicker pressure vessels and piping which will increase the capital cost of the system [7].

2.2.3 Stirling Engine

The Stirling engine is an old thermodynamic cycle that was patented by its inventor Robert Stirling in 1816 [28]. It is a closed reversible cycle and resembles the Carnot cycle in order to maximize thermal efficiency [4]. The thermodynamic process of this cycle is shown in Fig. 11.

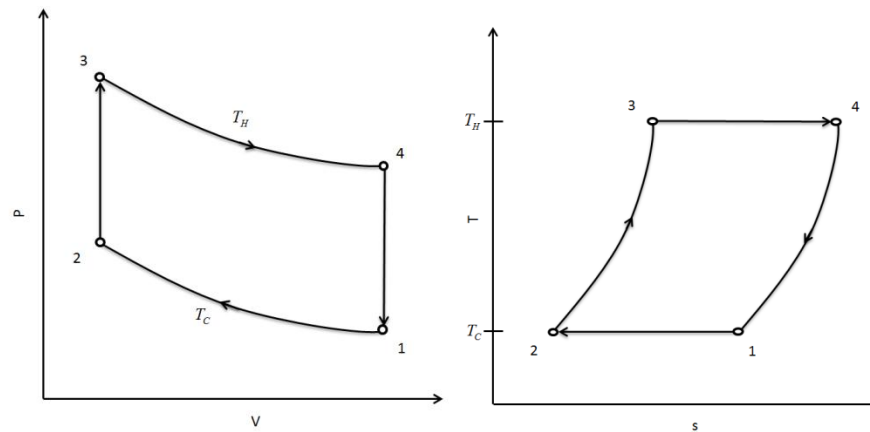


Fig. 11: Qualitative P-v and T-s diagrams for a Stirling engine.

The thermodynamic cycles are described by:

- *Isothermal compression* $1 \rightarrow 2$: the compression piston moves forward to the regenerator and the working fluid stays at a constant temperature as heat is removed from T_c to the surroundings. The amount of work performed on the fluid is equal to the amount of heat that is removed.
- *Constant volume regeneration* $2 \rightarrow 3$: both pistons move to keep the volume constant. The fluid is transferred from the compression chamber to the expansion chamber through the regenerator where it picks up heat and raises its temperature to T_H . The pressure increases and no work is done
- *Isothermal expansion* $3 \rightarrow 4$: the expansion piston moves outward increasing the volume and decreasing the pressure. The temperature is kept constant by adding heat externally. The amount of heat that is put into the system is equal to the amount of work taken out.
- *Constant volume regeneration* $4 \rightarrow 1$: again both pistons move to keep the volume constant and as the fluid moves back through the regenerator heat is removed and stored. This reduces the temperature of the working fluid to T_c .

The Stirling engine is composed of the following components: piston engine, heater, regenerator, and cooler. The piston engine has several different configurations and three common types are alpha, beta, and gamma. The regenerator itself is a porous matrix that

stores heat from the working fluid during $4 \rightarrow 1$ and returns it in $2 \rightarrow 3$. It can be made of several materials like steel wool, steel felt, wire mesh, fine pipes, spring mesh, stacked screen, and metal foils [29]. A component diagram and illustration of the different thermodynamic processes are shown in Fig. 12.

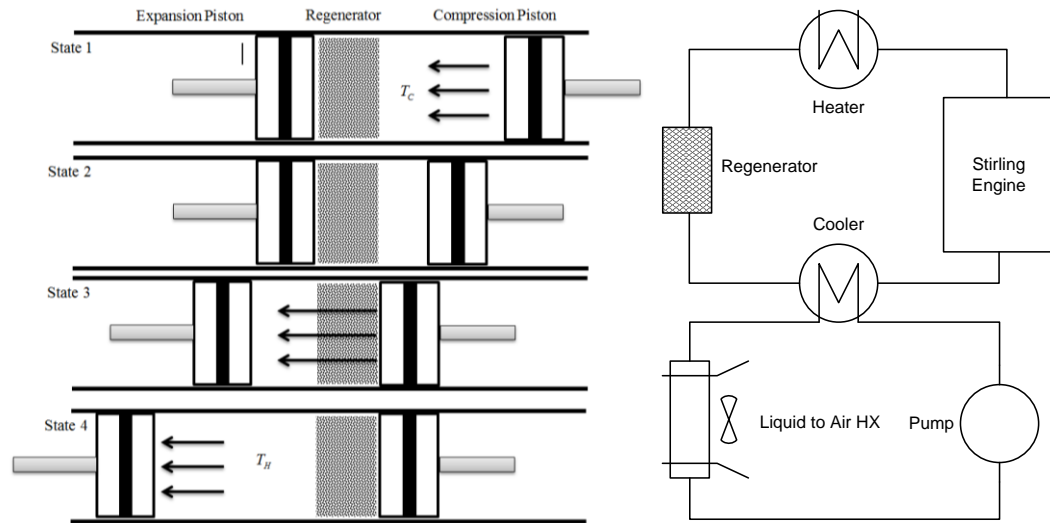


Fig. 12: Illustration of the different thermodynamic states of the Stirling cycle and a component diagram [29].

Main factors that affect the performance of the engine include regenerator effectiveness, volumes of un-swept gas that are known as dead volumes, thermal losses, and mechanical losses from seals, piston rings, bearings, and other frictional parts. Additionally ideal assumptions such as isothermal processes and a regenerator effectiveness of unity are not practical and would require infinitely slow heat transfer time or an infinitely long heat transfer area. From a material stand point a disadvantage of this cycle is its operating pressures which can reach 10-20MPa [29].

Thombare and Verma [29] made the following recommendations for the regenerator design. Desirable characteristics include maximizing heat capacity and heat transfer while minimizing dead space, flow losses, and contamination. The working fluid should have a high thermal conductivity, high specific heat capacity, low viscosity, and low density. Some common working fluids are helium and hydrogen.

They described the Stirling engine as one of the most complicated thermal cycles due to the interwoven motions of the compression-expansion pistons, heat transfer, and complicated control schemes. It requires joint thermal, fluid, and mechanical considerations in its design and optimization. It should be noted that the cycle when properly optimized can achieve efficiencies that are 65-70% of the Carnot efficiency.

2.2.4 Thermal Electric Generators

These devices produce a voltage potential from a heat flux. A simple form of this device would be comprised of several thermocouples connected in series to create a usable voltage [7]. This device would resemble a thermopile and would have a very low efficiency. To obtain improved efficiencies special materials are used to maximize this potential. The elements of a TEG are shown in Fig. 13.

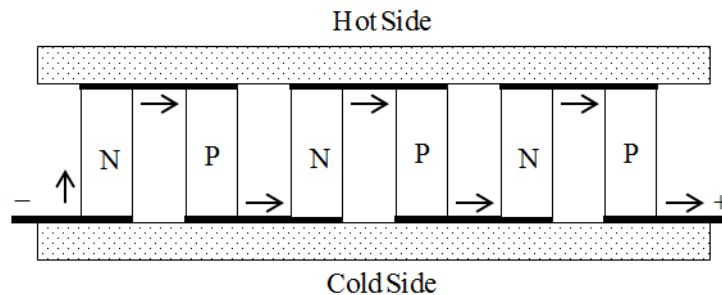


Fig. 13: The arrangement of the P and N type semiconductors in a TEG [7].

The N and P-type semiconductors are characteristically different. The N-type moves free electrons from the cold side to the hot and the P-type move them from the hot to the cold. A TEG is composed of a series of these devices. The limitations in performance of these devices is given by

$$E = \alpha \Delta T \quad (1)$$

where E is the voltage, ΔT is the temperature differential between T_H and T_C , and α is the Seebeck coefficient. The Seebeck coefficient is a property of the material and is a primary limitation in performance. The theoretical efficiency of a TEG can be expressed by

$$\eta_{TEG} = \left(1 - \frac{T_C}{T_H}\right) \left(\frac{\sqrt{1 + ZT_{ave}} - 1}{\sqrt{1 + ZT_{ave}} - \frac{T_C}{T_H}} \right) = \eta_{Carnot} \eta_{seeb} \quad (9)$$

where ZT_{ave} is a dimensionless figure of merit for the material and η_{seeb} is the conversion efficiency of the material. Some common ZT_{ave} values for bulk materials such as Bi_2Te_3 , $PbTe$, and $SiGe$ are on the order of one. This low value is responsible for the low efficiency of TEGs. Continued research into semiconductor wells, superlattice structures, Si nanowires, quantum dot, and other nanostructures hold promise for higher ZT_{ave} values [30].

The advantage of a TEG is that they have no moving parts and therefore have exceptional reliability. Unlike heat engines these devices are able to produce electricity directly from the flow of heat. An innovative application of TEGs is using them combined with an ORC [31].

2.2.5 Comparison

These cycles and devices have their own advantages and disadvantages. The Kalina and transcritical CO_2 cycle show promise in thermodynamic performance but have not met widespread adoption and have not been proven. Both cycles have high operating pressures which introduces material limitations. The use of corrosive ammonia in the Kalina cycle limits the materials that can be used. There continues to be work on the Stirling engine and TEG and they hold promise of higher thermal performance. The Stirling engine has the disadvantage of operating at very high pressures and temperatures. The ORC requires a minimal number of components and is well established technology. The copious number of working fluids allows it to be optimized for a variety of heat sources. Additionally it can operate efficiently over a wide range of pressures and temperatures.

2.3 Expander Overview

It was aforementioned that the expander is the most important component in the efficient recovery of low temperature heat. The selection of the correct type as well as the optimization of its performance is paramount in achieving high thermal efficiencies. There

are many important parameters when selecting an expander such as high isentropic efficiency, pressure ratio, power output, lubrication requirements, complexity, rotational speed, dynamic balance, reliability, and cost. In low temperature heat recovery the turbine, which is the dominant type of expander in conventional power plants, is not necessarily the most appropriate choice. Expanders can be categorized into dynamic and positive displacement types. Most compressors are positive displacement while turbo-machinery is dynamic. Research in the area of compressors has led to many devices that have been found to function efficiently as expanders. The expanders that will be discussed include turbine, reciprocating piston, rotary vane, rolling-piston, gerotor, and scroll types.

2.3.1 Turbine

Turbines are dynamic machines and can be broken up into impulse, reaction, and radial inflow types. Impulse turbines guide the flow into bucket shaped blades at which the kinetic energy of the fluid is converted into motion of the rotor. Reaction turbines in comparison use aerodynamic lift. Radial inflow turbines are like reaction turbines, but in a different orientation. These different types are illustrated in Fig. 14.

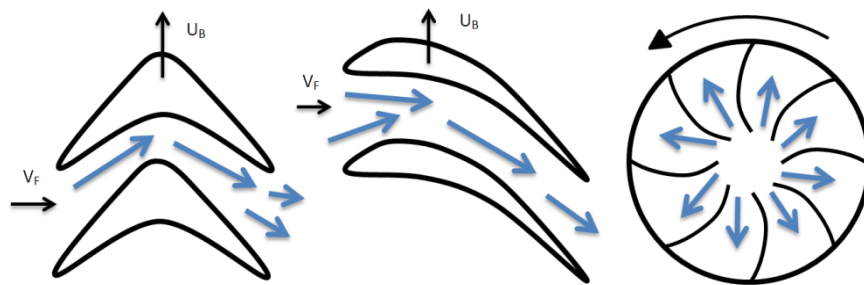


Fig. 14: Impulse turbine (left), reaction turbine (middle), and radial inflow (right).

Turbines dominate utility level power generation. At this size they are known to achieve isentropic efficiencies over 90% [7]. The most critical factor in turbine performance is the ratio of the rotor tip speed to the incoming fluid speed (U_B/V_F) [7]. The tip speed is defined as

$$U_B = \frac{\pi NR}{30} \quad (10)$$

where N is the rotational speed in [RPM] and R is the radius of the turbine. This ratio explains why turbines have poor off design performance. We can infer for a given U_B/V_F ratio and a specified V_F a small machine must rotate at very high speeds to maintain optimal performance. In practice turbines have tip speeds of 305 [m/s] in order to reduce the number of turbine stages [7]. The high speed is related to the blade Reynolds number which should be on the order of 10^6 . This is difficult to achieve in small turbines and organic fluids which have high molecular weights are used to maintain this parameter. Another characteristic of turbines is a low pressure drop per stage. A pressure ratio of 2 is considered large, and larger pressure ratios are achieved by using multiple stages [7]. The disadvantage of requiring multiple stages is that it increases cost.

The primary contribution to loss in a turbine's performance is from aerodynamic effects such as flow separation which can account for 10-30%. Other sources include tip leakage (1-2%), bearings (1%), seal leakage (1%), and moisture churning (1% per 1% of moisture) [7]. Certain losses are exaggerated when turbines are scaled down. The tip leakage which is the amount of fluid that passes between the housing and the tip of the turbine blades increases to 10- 15% in small machines [7]. Other considerations for small turbines that produce on the order of 10-100 [kW] are small blade height, low Reynolds number effects, tip clearance, surface finish, and manufacturing tolerances [32].

A familiar problem with turbines is condensate formation from wet expansion. These droplets impact the blades and over time cause erosion which results in poor performance and mechanical failure. It was aforementioned that a quality of 90% or higher is optimal at the turbine exhaust. This problem ceases when turbines are used with d - fluids in ORCs.

Literature is limited on the performance of small scale vapor turbines. Yamamoto et al. [33] fabricated a small scale turbine for an ORC that used R123 as a working fluid. It was a radial inflow type with 18 blades. It was 30 [mm] in diameter and 4.5 [mm] thick. A summary of the operating conditions are given in Table 5 at the end of this section. The turbine managed to achieve a maximum isentropic efficiency of 46%. This paper also

demonstrated how sensitive turbine performance is to operating conditions. Changing the heat input from 13 [kW] to 9.7 [kW] the turbine efficiency dropped to 15%. The change in volumetric flow rate was likely the cause for the performance drop. The turbine performed optimally at a specific speed for a given heat input. Any deviation would cause a parabolic decrease in power output.

Yagoub et al. [34] used a turbine expander for a CHP ORC. They did not test for off design parameters but at 60,000 [RPM] the expander managed to achieve a high isentropic efficiency of 85% when used with HFE-301. The power output was on the order of one [kW]. The efficiency decreased to 40% when n-Pentane was used as the working fluid. This demonstrates that small turbines can achieve high isentropic efficiencies. It should be mentioned that turbines are precision machines and have a high capital cost.

2.3.2 Reciprocating Piston

Pistons are positive displacement machines and are over 200 years old. In a Rankine cycle the piston expander is composed of three processes; intake, expansion, and exhaust. These are illustrated in Fig. 15.

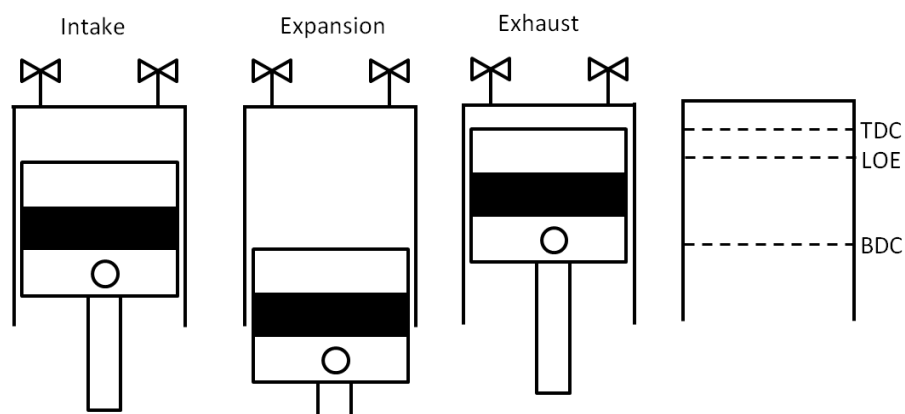


Fig. 15: Different processes of a reciprocating piston [35].

When the piston is at top dead center (TDC) the intake valve opens. High temperature-pressure vapor fills the chamber until the piston reaches the location of expansion (LOE) and the intake valve closes. The vapor expands driving the piston down to bottom dead center

(BDC) and the exhaust valve opens. The piston rises to TDC to expel the low temperature-pressure vapor. Upon reaching TDC the exhaust valve closes and the cycle repeats.

Reciprocating pistons are complex devices that require precise timing of the intake and exhaust valves. They also require both primary and secondary balancing. Primary balance is the effect caused by a mass rotating about the shafts center and secondary is the effect of a mass that rotates around a center that is not concentric with the shaft. They are also known to have large friction losses from the large number of interacting surfaces. A primary contribution is friction between the piston rings, piston, and cylinder wall. An ORC could decrease the impact of these losses by dissolving oil into the working fluid.

Baek et al. [35] design a transcritical CO₂ heat pump and replaced the expansion valve with a piston expander in an effort to increase the COP. The expander was a modified four cycle two cylinder gasoline engine. To limit the requirement of a flywheel the two pistons were modified to operate out of phase. The valve timing was controlled by electronic solenoid valves. The displacement volume of the device was $2 \times 13.26 \text{ [cm}^3\text{]}$. The expander achieved a low isentropic efficiency of 11%. The lower performance was contributed to internal leakages.

Zhang et al. [36] also developed a transcritical CO₂ cycle but fabricated a free piston expander to replace the expansion valve. This device combines the compressor and expander into one unit. This eliminates the need for a camshaft. Instead a slider controls the opening and closing of the intake and exhaust valves. It was expected to achieve a compressor and expander efficiency of 60% and 70% respectively. Extrapolating data from the P-V diagram and their expert opinion they estimated the expander efficiency to be 62%. Under expansion was estimated to account for 10.3% of the loss while 8.4% was contributed to the large pressure drop in the discharge process. A summary of these results are provided in Table 5.

2.3.3 Rotary Vane

Rotary vane expanders (RVE) are positive displacement devices. The makeup includes housing, rotor, vane slots, and vanes which are shown in Fig. 16. In operation a high pressure-temperature vapor enters the inlet (1) which expands causing the rotor to move.

As the rotor moves the expansion volume increases (2→3). The volumes are kept isolated by the vanes which slide out to form a seal. High pressure behind the vanes keeps them in place. At the end of expansion the vapor is exhausted (4). They have several positive characteristics such as simple construction, low noise- vibration, high volumetric expansion ratios as large as ten, and are tolerant of wet expansion [37]. They are also capable of handling high pressures [38].

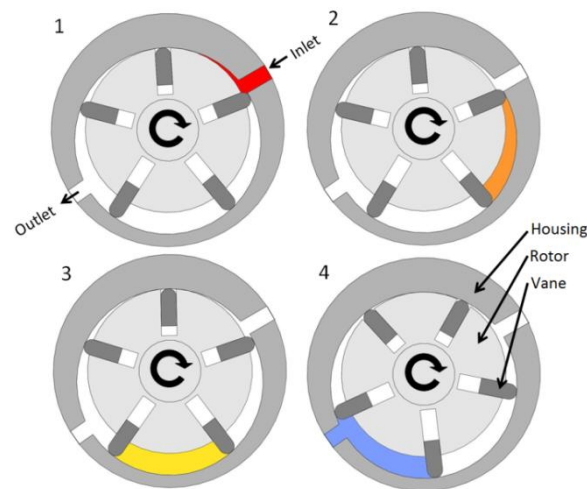


Fig. 16: Rotary vane expander with intake (1), expansion (2-3), and exhaust (4). Leakage and friction are the primary causes for loss in performance RVE.

In operation the device must be lubricated to minimize wear and enhance sealing. A low number of contacting surfaces minimizes friction loss in these devices. Leakage has been found to be a larger contributor in performance loss than friction [38], [39]. This occurs in two locations; between the vanes and housing as well as in between the rotor ends and sealing faces. Badr et al. [37] claim that the pressure drops during intake account for 65% of the loss in efficiency while leakage only accounts for 20%.

Yang et al. [39] tested a double acting RVE in a vapor compression cycle where it replaced the expansion valve to improve the COP. A double acting RVE has two inlets and exits which is beneficial because it creates balanced loading and low vibrations. In its design particular attention was given to leakage. Springs were placed behind the vanes to ensure good sealing. The expander achieved a maximum isentropic efficiency of 23% at 800 [RPM]. The efficiency decreased at higher speeds and was contributed to the increase in frictional

losses. In some cases with RVEs the vanes will impact the cylinder wall. The authors concluded the main cause of this was by incoming vapor pushing the vanes to the bottom of the slots which then bounce back and strike the cylinder wall.

Mohd et al. [38] tested a RVE in an ORC with a source temperature that ranged between 60-80°C. The RVE achieved a maximum isentropic efficiency of 48% with a power output of 32 [W]. A summary of these results are provided in Table 5.

2.3.4 Rolling Piston

The rolling piston, swing piston, and revolving vane expanders are positive displacement devices. A swing arm piston expander differs from a rolling piston expander in that the piston does not roll and instead swings. In this device the piston and vane are one part. A rolling piston during expansion is shown in Fig. 17. The high pressure-temperature vapor enters the inlet (1) and the piston begins to roll. This rolling accommodates the expansion of the vapor (2→3). At the end of expansion it is exhausted through the outlet (4). The sealing vane is in constant contact with the rolling piston and is held in place by a spring. These devices are commonly used as compressors in the vapor compression cycle. Development of these devices has continued since the 1970s due to their ability to handle large pressures at low compression ratios [40].

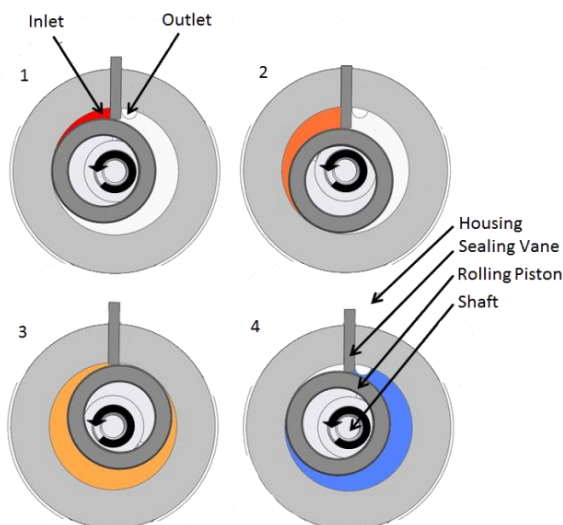


Fig. 17: Rolling piston expander with intake (1), expansion (2-3), and exhaust (4).

Rolling piston expanders have many advantages that include simple construction, few parts, and the ability to handle high pressures. Due to their constrained nature they require tight tolerances to minimize leakage. Additionally lubrication is required to minimize wear and enhance sealing. The primary modes of loss for these devices are friction and leakage. The primary path for leakage occurs between the rolling piston and the cylinder wall. This is caused by the large pressure differential between the neighboring chambers [40].

Wang et al. [22] used a rolling piston expander in a solar powered ORC that used R245fa as the working fluid. It achieved a maximum isentropic efficiency of 45.2% at 800-900 [RPM]. Haiqing et al. [40] used a swing piston expander to replace the expansion valve in a transcritical CO₂ cooling cycle. They claimed that a swing piston should have superior performance over a rolling piston because of a reduction in friction and leakage. It achieved a maximum isentropic efficiency of 44% at 1,800 [RPM]. In contrast this device performed no better than the aforementioned rolling piston expander. Subiantoro and Ooi [41] modeled the performance of a revolving vane expander and claimed that it should provide superior performance to both the rolling piston and swing arm expanders. They recommended a revolving vane expander where the sealing vane is attached to the rotor and the rotor is the driving mechanism.

2.3.5 Gerotor

The gerotor is a positive displacement device. It consists of an outer stator and inner rotor that have eccentric centers to each other. Both of these components share a common shaft and are illustrated in Fig. 18. The rotor has four teeth and the stator has five. The contact points between the two form a sealed chamber for the expanding vapor. It has the advantage of a reduction in friction between the rotor and stator. The rotor and stator do not rotate at the same speed. A five tooth stator will move at one-fifth the shaft speed relative to the rotor [42]. This means that a shaft rotating at 3,000 [RPM] would result in a relative shaft speed of 600 [RPM] between the rotor and stator. The gerotor also benefits

from a simple construction. This device shares many of the advantages of the rotary vane and rolling piston expanders but with a reduction in friction losses.

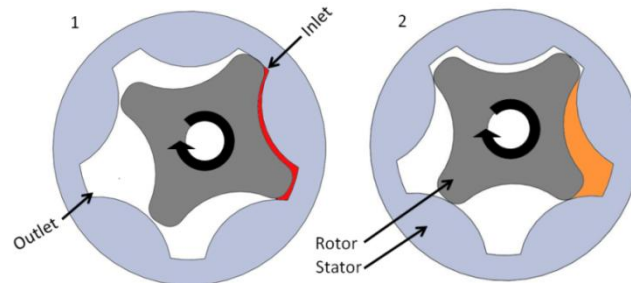


Fig. 18: Gerotor expander with intake (1) and expansion (2). Not all steps are shown due to the complexity of the motion between the rotor and stator. They both rotate in the same direction.

Mathias et al. [42] demonstrated a gerotor in an ORC. They tested three different gerotors which they identified as A, B, and C. Gerotor A had a large spacing between the stator and rotor. This resulted in excessive leakage and poor performance. It achieved a maximum isentropic efficiency of 66%. Gerotor B in contrast had insufficient spacing between the rotor and stator which was contributed to thermal expansion. It eventually failed due to excessive wear but achieved an isentropic efficiency of 66%. Gerotor C showed good performance and achieved a high isentropic efficiency of 85%.

An interesting quantity they used to optimize the performance of their expanders was the expansion-matching ratio (EM_{ratio}). It is a figure of merit of how close an expansion process comes to a devices ideal expansion. A value close to unity represents an ideal expansion. Alternatively the ideal expansion can be determined through a qualitative evaluation of expander performance as a function of pressure ratio. Evaluating the data we can see that with an EM_{ratio} of 1.07 gerotor C achieved an isentropic efficiency of 85%. The efficiency drops to 45% when the EM_{ratio} is 1.39. This shows that the gerotor has poor off design performance.

2.3.6 Scroll

The scroll expander is a positive displacement device and is commonly used as a compressor in vapor compression cycles. Common to all positive displacement devices it has

a fixed volumetric ratio. Compared to the aforementioned positive displacement expansion devices it has the most complicated geometry. It is made up of two involute curves in opposing directions. They are called the orbiting and fixed scrolls. The fixed scroll does not move and the orbiting scroll always keeps its orientation while it orbits around the shafts center. The high pressure-temperature vapor enters the suction port (1). It then expands steadily increasing the expansion volume (2-5). At the end of the expansion the low pressure-temperature vapor is exhausted (6). This process is shown in Fig. 19.

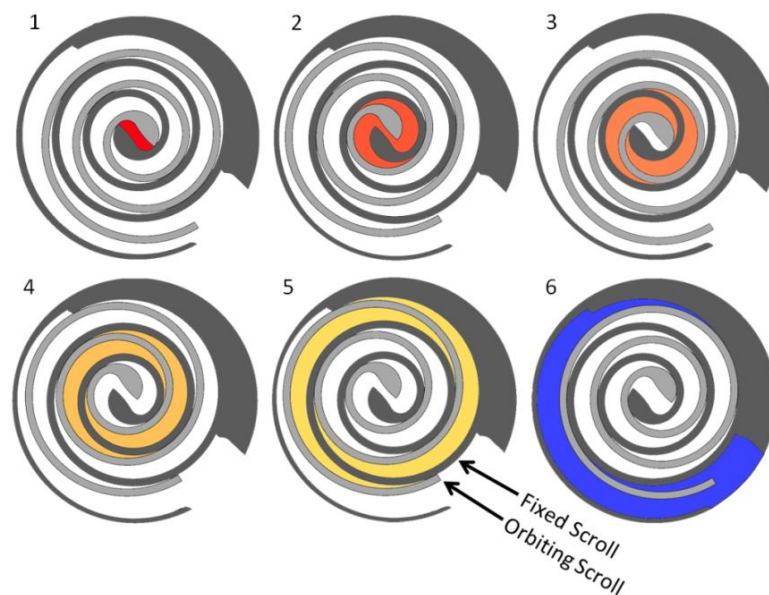


Fig. 19: Scroll expander with fixed and orbiting scroll shown. Intake (1), expansion (2-5), and exhaust (6).

Scrolls can be categorized into two types; compliant and kinematically constrained. Constrained scrolls are fixed in their position. They can be constrained radially, axially, or both. Commonly they are composed of three cranks that are separated by 120° [6], [43]. The three cranks are then linked to a common shaft. It is because of this additional gearing that the scroll and shaft can have different speeds [43]. Manufacturing tolerances are a critical parameter in the effective sealing of constrained scrolls. A compliant scroll in contrast is not constrained and uses a centrifugal effect to keep the orbiting scroll in continuous contact with the fixed scroll. Compliant scrolls require lubrication to operate

efficiently without causing significant wear. Constrained scrolls in contrast can operate without lubrication.

Like the aforementioned positive displacement expanders scrolls are negatively impacted by leakage. The two leakage passages in a scroll assembly are shown in Fig. 20.

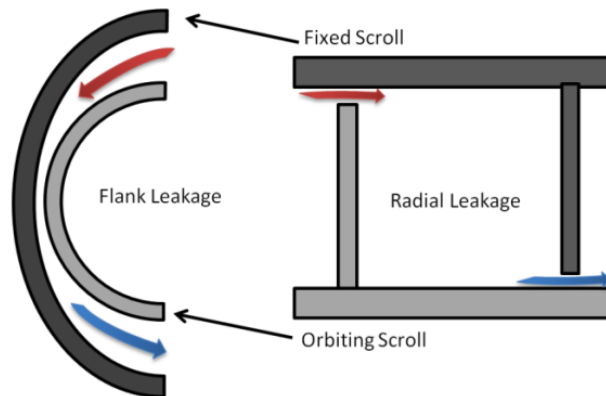


Fig. 20: This shows the two passages for leakage in a scroll assembly [44].

An advantage of compliant scrolls over constrained types is that they can provide better radial and flank sealing. The scroll wraps are only separated by an oil film. They also have the advantage of being tolerant of liquids which allows them to increase the gap size if excessive pressure builds up inside the device [6].

In constrained scrolls a low friction material is used to form a tip seal between the plates which resists radial leakage. Only the tight tolerances between wraps minimize the amount of flank leakage. This sealing can be improved by using oil which acts as a gap filler [6]. Peterson et al. [6] mentioned that constrained scrolls that operate as expanders have a tendency to washout this oil. When they operate as compressors it is swept in.

The primary modes of loss are both leakage and friction. Peterson et al. [6] determined that the poor performance of constrained scroll expanders was caused by excessive leakage. Lemort et al. [45] created a semi-empirical model for the performance of a scroll expander. They concluded that internal leakage is the largest contributing factor in efficiency loss. The lesser but second largest contributor was mechanical losses. Other publications have also concluded that leakage is the primary cause for decreased performance [43], [44].

In constrained scroll expanders internal leakage can be controlled to an extent by increasing the speed of the expander. This is why their efficiency increases with speed [6], [43], [44] because of the time the vapor has to escape decreases. There is a point where increasing the speed will have a negative impact on performance. At excessive speeds frictional losses will become noticeable.

Scroll expanders have demonstrated high performance over a variety of working conditions. They consistently achieve isentropic efficiencies over 50% and have achieved efficiencies as high as 83%. They also have demonstrated good partial load performance [10], [42].

2.3.7 Comparison

There are many different expanders that can convert a high pressure-temperature vapor into mechanical work. This review has shown that not all expanders are created equal and that each has their own limitations and trade-offs. Some are applicable to small-scale operation while others (such as turbines) are not. These considerations are presented in summary below.

Turbines: turbo-machinery is a well proven technology at large scale but they require excessively high speeds to operate efficiently at small speeds. They have poor off design performance and have poor compatibility with wet fluid types. Single turbine stages are characteristic of low pressure ratios. They have been shown to have isentropic efficiencies as high as 85% in a low temperature ORC. Limited literature exists on their performance in small scale ORCs.

Reciprocating Piston: reciprocating pistons are a mature technology but they are characteristic of high friction losses. They require both primary and secondary balancing as well as a cam system to ensure proper valve timing. They have been reported to have an isentropic efficiency of 62% in a transcritical CO₂ cooling cycle but no literature exists on their performance in ORCs.

Rotary Vane: they are simple and robust in design but they are susceptible to high friction losses from the large number of interacting components. They are also susceptible to leakage through the vanes as well as through the end faces of the rotor. They are tolerant

of wet expansion and can handle high pressures. A rotary vane has been recorded to have an isentropic efficiency of 48% in a low temperature ORC but they have not been extensively researched in this application.

Rolling Piston: these devices are simple and robust in design. They have a reduction in the overall number of moving parts as compared to a RVE and therefore should have a reduction in frictional losses. There are several variations that aim to minimize leakage paths and friction. They are also tolerant of wet expansion and high pressures. Isentropic efficiencies as high as 45.2% have been achieved in a solar powered ORC but they have not been extensively researched as expanders in ORCs.

Gerotor: it is more complicated than the rolling piston and rotary vane in operation but it is still a simple and robust device. Due to the low relative velocities between the rotor and stator it benefits from a decreased frictional loss when compared to rotary vane and rolling piston types. It like other positive displacement types it can handle wet fluids and high pressures. It has been shown to have a very high isentropic efficiency of 85% but it has not been tested extensively. Current results show that it has poor off design performance. Only one literary source has documented its performance as an expander.

Scroll: of the positive displacement types the scroll has the most complicated geometry and requires tight manufacturing tolerances. With both axially and radially compliant scrolls the effect of leakage, which is the primary cause of loss of performance, can be minimized. It can handle wet expansion. It has been shown to achieve isentropic efficiencies as high as 83% over a variety of working conditions and has been tested extensively in literature. It has shown good off design performance.

The gerotor is shown to have a higher maximum efficiency than the scroll but it has not been tested as extensively in literature. The scroll has shown a high efficiency over a variety of working conditions. For this reason we chose to develop a high efficiency axially and radially compliant scroll expander for use in an ORC.

Table 5: Summary of operating conditions and performance of different expander types.

Type	Isentropic Efficiency [%]	Expander Inlet Temperature [°C]	Expander Inlet Pressure [bar]	Pressure Ratio	Power Output [W]	Speed [RPM]	Working Fluid	Reference
Turbine	46 ²	70 ¹	3.4 ¹	2 ¹	150 ¹	17,000 ¹	R123	[33]
Turbine ^{3,5,5}	85	70	2.2 ¹	1.1	1500	60,000	HFE-301	[34]
Turbine ^{3,4,5}	40	95	2.7 ¹	1.1	1500	60,000	n-Pentane	[34]
Piston (Recip.) ⁷	10.5	87	60.5	2.1	24.35	114	CO ₂	[35]
Piston (Free) ^{6,7}	62	-	7.8	2.4	-	306 ⁹	CO ₂	[36]
Rotary Vane	48	80 ⁸	2.9	24.2	32.1	2,095 ¹	R245fa	[38]
Rotary Vane ⁷	23	-	90-75	1.5	-	800	CO ₂	[39]
Swing Piston ⁷	44	42	82.3	-	500	1800 ¹	CO ₂	[40]
Rolling Piston	45.2	83 ¹	6	2.2	1,730	800-900	R245fa	[22]
Gerotor A	66	84	4.1	3.0	280 ¹⁰	3,670	R123	[42]
Gerotor B	66	146	18.8	8.3	480 ¹⁰	3,670	R123	[42]
Gerotor C	85	150	12.3	4.2	1,960 ¹⁰	3,670	R123	[42]
Gerotor C	45	160	10.9	5.3	2,070	3,670	R123	[42]
Scroll A	67	127	13.5	8.8	1,200 ¹⁰	3,670	R123	[42]
Scroll B	81	149	18.2	5.5	1,380 ¹⁰	3,670	R123	[42]
Scroll C	83	155	17.9	3.1	1,750 ¹⁰	3,670	R123	[42]
Scroll C	83	120	11.9	3.0	1,040	3,670	R123	[42]
Scroll Con. ⁵	49.9	170	6.4	3.82	256	1,287	R123	[6]
Scroll ⁵	65	136	8.3 ¹¹	-	350	2,800 ¹	R113	[46]
Scroll Con.	33	145	13	11.4	-	2,355	Water	[43]
Scroll	65	65	13 ¹¹	-	2,050	2,000	R134a	[21]
Scroll Con.	68	142	10.03	5.0	-	2,296	R123	[45]
Scroll	45 ¹²	70	3.25 ¹¹	-	211 ¹	891 ¹	R134a	[47]

Table 6: List of assumptions for Table 5.

1	These values were estimated from plots
2	These values were not given explicitly and had to be back calculated
3	Turbine work calculated using enthalpy values instead of a torque meter
4	Represents actual efficiency which includes electric conversion losses
5	Regenerator was used
6	Expander efficiency estimated by P-V diagram
7	Expander replaced an expansion valve in a vapor compression cycle
8	Represented as a temperature difference between the hot and cold side temp
9	This is a linear motion device and for comparison is represented as RPM
10	This is electric power produced and not expander work produced
11	This represents a pressure drop through the expander
12	This represents the product of the isentropic and mechanical efficiency

3 EXPANDER SELECTION AND DESIGN

With the expander type chosen, scroll compressor parts were required in order to fabricate the expander. A selection process was conducted that met our design criteria. A power takeoff scheme had to be chosen and designed. Additional systems such as lubrication and balancing also had to be implemented. This is an overview of the design process behind the scroll expander.

3.1 Design Conditions

A theoretical model was developed using EES for a heat activated cooling (HAC) system. This is an ORC cycle which mechanically powers a vapor compression cycle. From this model the design conditions in Table 7 were calculated.

Table 7: Design requirements for the scroll expander and preliminary test conditions.

Conditions	Design	Preliminary
Maximum Temperature	190 [°C]	125 [°C]
Minimum Temperature	150 [°C]	60 [°C]
Maximum Pressure	400 [psi]	220 [psi]
Minimum Pressure	80 [psi]	60 [psi]
Working Fluid	R245fa	R134a

The maximum pressure-temperature will occur at the scroll inlet and the minimum will occur at its exit. The working fluid is R245fa and was chosen for its high performance at the specified temperature range. Before the above design conditions are met the scroll expander will be tested at the preliminary design conditions with R134a.

3.2 Scroll Compressor Selection

As no company commercially manufactures scroll expanders we selected a scroll compressor that met our design criteria. A compressor from a major manufacturer having an inlet volume of 7.37 [cm³] was selected. It has good compatibility with R245fa and R134a. The difficulty of turning compressors into expanders is that manufacturers put in devices such as check valves to prevent back flow. This is meant as a safety precaution to prevent

high pressure fluid from entering the low pressure chamber. These devices had to be removed for the expander to function properly.

The scroll compressor we received was hermetically sealed and had to be sawed open to recover the scroll components. The two components that were recovered included the scroll assembly and the drive shaft. There was one check valve at the exit of the compressor and it was removed. A precise model of the scroll wraps were used to measure the inlet and exit volumes. Wang et al. [48] calculated the expansion ratio of the scroll unit to be approximately 2.5. They used efficiency plots provided by the manufacturer and correlated the maximum efficiency point to a compression ratio. There is a discrepancy between the two values, which is caused by a level of uncertainty in what is considered the inlet volume. The properties of the scroll components are summarized in Table 8.

Table 8: Summary of scroll characteristics.

Scroll Assembly Max. Height	4.876 [in]
Scroll Assembly Max. Diameter	5.238 [in]
Capacity	6.3 [kW]
Scroll Flank Height	0.7382 [in]
Inlet Volume	0.45 [in ³]
Exit Volume	1.03 [in ³]
Compression Ratio	2.29
Compression Ratio [48]	2.5

3.1.1 Scroll Compressor Description

The chosen scroll compressor is both an axially and radially compliant scroll. As was aforementioned leakage is the primary mode of efficiency loss in scroll expanders and compliant scrolls inherently have better sealing characteristics than constrained types. The scroll assembly is shown in Fig. 21.

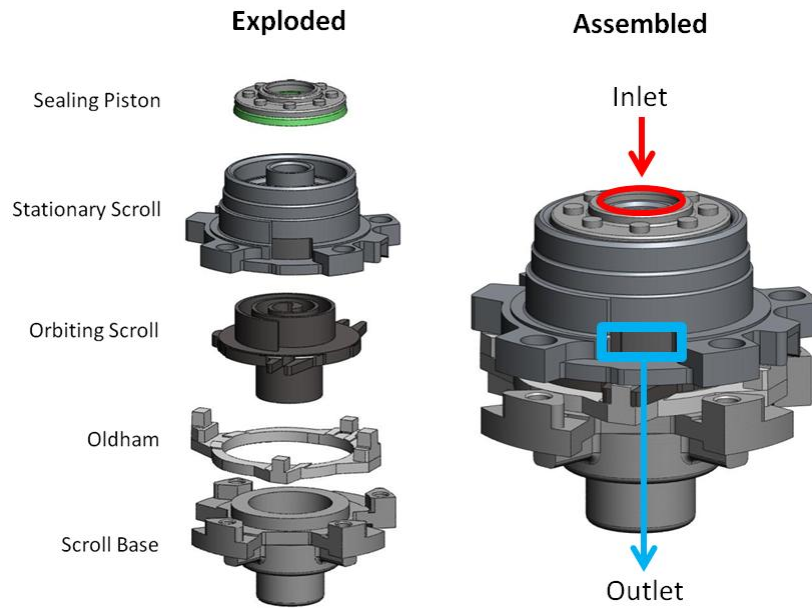


Fig. 21: Scroll compressor exploded (left) and assembled (right) views.

There are the stationary and orbiting scrolls sub-units which produce work from expanding the working fluid. The motion of the orbiting scroll is maintained by the “Oldham.” It is made of aluminum to reduce its effect as a rotating mass. Three bolts hold the stationary scroll to the scroll base. This prevents it from moving radially but it is allowed to a small degree to move axially. This is what makes it axially compliant. If liquid were to enter the chamber it could pass through the radial passages and leave the scrolls undamaged.

Axial compliance is controlled by the sealing piston. It is designed to apply enough pressure to minimize the axial clearance without creating excessive friction. The sealing pistons most important function is to seal the high pressure chamber from the low. This system presents a design challenge when it operates as an expander. Normally the electric motor would turn and engage the orbiting scroll which would draw in vapor. This vapor would be compressed and at point 4 in Fig. 19 a small amount of high pressure vapor would be bled off through the pressure port in Fig. 22 into the sealed chamber under the piston. This would cause the piston to rise which would create a seal between the high and low pressure chamber. Additionally this creates a force that pushes the stationary scroll down which minimizes the radial leakage.

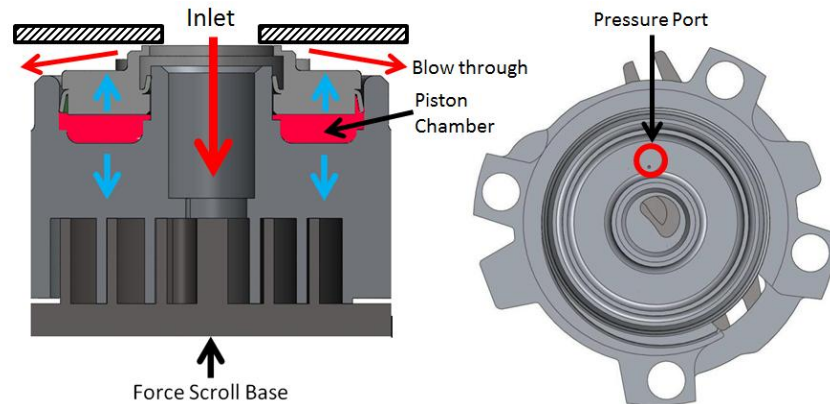


Fig. 22: Scroll sealing piston with high pressure highlighted in red and relative movement in blue.

In an expander this poses a design challenge because the sealing piston chamber has to be pressurized prior to the working fluid entering the scroll which otherwise would blow by the scroll assembly and not create any work as shown in Fig. 22.

The next important component is the shaft. Beyond providing a medium to transfer power, the shaft in the compressor also acts as an oil pump. It should be thought of as a rudimentary centrifugal pump. It has an impeller, suction hole, and discharge port. These are illustrated in Fig. 23.

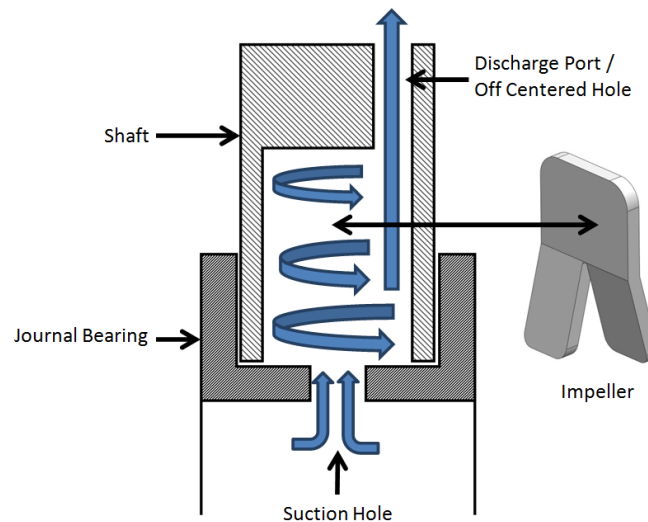



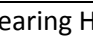
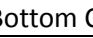
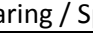

Fig. 23: Lubrication system for scroll compressor.

In a centrifugal pump fluid is accelerated by a rotating impeller outwards. Upon striking the outer wall the fluid increases its pressure and is discharged. The working principle of the pump is based on the Bernoulli principle. The fluid gains kinetic energy which is converted into pressure. In the scroll unit, lubricating oil is brought up into the suction hole below the journal bearing. The fluid is then accelerated outward and upward with the impeller. The pressurized oil is driven up through the off centered hole in the shaft. This supplies two journal bearings with oil and helps lubricate the scroll assembly. The journal bearing in Fig. 23 is lubricated by pooled oil at the bottom of the compressor.

3.3 Review of Previous Designs

The proposed expander is the 3rd iteration using scroll compressor assemblies. It is in the interest of this paper to present an overview of these designs. These previous designs provided important lessons that helped guide decisions for the 3rd iteration. Several of the components in the 2nd iteration were used in the 3rd. To simplify the description of the designs Table 9 has been constructed as a reference.

Table 9: Figure references for description of designs.

Top Cover	1		Bearing Holder	7	
Scroll Assembly	2		Bottom Cover	8	
Housing	3		Gearing / Sprocket	9	
Large Counterweight	4		Power Takeoff	10	
Shaft	5		Artificial Sump	11	
Small Counterweight	6				

3.3.1 1st Design Iteration

This was designed by Tom Herron, Dr. Hailei Wang, and Dr. Richard Peterson. Its primary purpose was a proof of concept. The scroll assembly in the scroll compressor is held rigid by the housing. There is a light press fit between them. Four divots hold onto the scroll base. In order to maintain its rigidity the scroll assembly with this portion of the housing was removed together. Two stainless steel plates were attached onto the top and bottom of the

saved portion of housing. This proved challenging because of the problems associated with bonding dissimilar metals. The final design is shown in Fig. 24 (left).

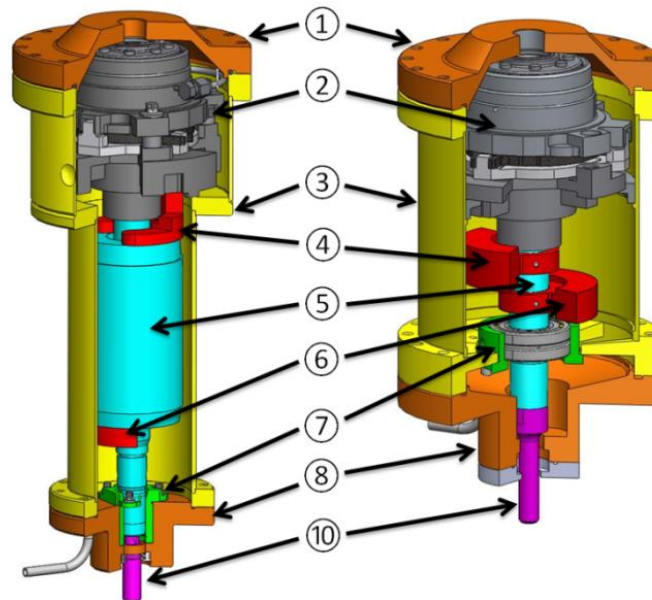


Fig. 24: 1st generation scroll expander (left) and 2nd generation (right). Both are not on the same scale.

The power takeoff is placed on the bottom which rendered the pre-existing lubrication system ineffective. This was replaced by an external oil loop that continuously supplied oil up the shaft. The downside of this is that it requires additional equipment and the power to run the pump. Another impact was heat loss because the oil loop had a cooling effect on the expander which degraded the performance.

At the time it was thought that creating custom counterweights was too complicated. Therefore the original shaft with its squirrel cage and counterweights was used. The downside of this is that it increases the weight of the device and the length of the shaft gives it a larger vertical footprint. The overall height is 17.55 [in].

Advantages of this design are that it required few modifications to the original components and had little vibration from the factory supplied counterweights. It also achieved a high efficiency over a wide range of pressure ratios. The maximum achieved isentropic efficiency was 77.5%.

3.3.2 2nd Design Iteration

This second iteration was designed by Erik Miller, Josh Doerr, Dr. Hailei Wang, Dr. Richard Peterson, and myself. It was meant to overcome some of the disadvantages of the previous design which included an active lubrication system and large vertical footprint.

To reduce the vertical profile the original shaft was modified and custom counterweights were designed. To replace the active lubrication system a scoop was designed to bring oil into the shaft. The final design is shown above in Fig. 24 (right).

Many problems were encountered in this design. The scoop was found to be ineffective and left the expander without a functioning lubrication system. It was concluded that once the oil was scooped up it would be thrown right back out. The custom counterweights could not be balanced by a third party due to inadequate shaft spacing. Additionally oversized holes on the bearing holder made concentricity of the shaft with the shaft seal difficult. This created sealing problems. Overall the expander was difficult to assemble and disassemble. The vertical footprint was reduced to 12.44 [in] but with a larger bottom cover the overall weight increased to 37.6 [lb]. It had an isentropic efficiency of 56.5%.

3.4 Transmission Configuration Selection

With proper scroll components selected the next step was to design a scroll expander that could mechanically power a compressor. This would be used in a HVAC system. Mechanical coupling is used instead of electric generation to eliminate the series losses generally associated with those systems [3]. Coupling methods such as direct drive, roller chain, helical spur gears, and spherical miter gears were considered. A house of quality was used to differentiate and select a final design.

3.4.1 Direct Drive

In this design both scroll assemblies of the expander and compressor share a common shaft. Our conceptualized model of this design is shown in Fig. 25. This design

should theoretically be the most efficient because it contained the least number of seals, bearings, and required no additional mechanical coupling.

This design has both a positive and negative effect on the shaft seal. It is positive in that the shaft seal experiences a lower pressure differential between the two low pressure chambers which should be around 10-20 [psi]. It has the negative effect of increasing the surface speed of the shaft. Frictional losses of shaft seals are a function of surface speed [49]. Another concern was heat loss. In order to minimize heat transfer an insulating layer would have to be inserted between the two housings. Advantages of this design include low weight, minimal components, and compactness. It should only require one counterweight to balance the two offset scrolls on either side of the shaft.

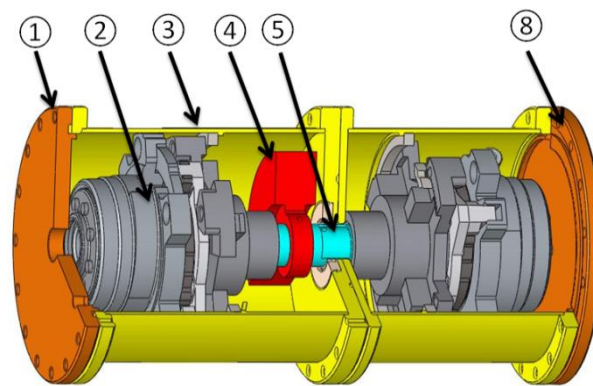


Fig. 25: Direct drive section view, expander top and compressor bottom (left). Isometric view (right).

A disadvantage of this design is that it requires a custom scroll assembly. With a common shaft both scroll assemblies rotate in the same direction and will operate as either expanders or compressors. Designing a custom scroll assembly would have been a substantial task. Lubrication was another drawback. This design would require an active lubrication system like the 1st generation. This would have caused the same problems seen in that design. This has the added complication of requiring two individual oil loops for the respective sides. In hindsight an agitator would have been needed in each chamber to mist the oil for effective lubrication of the scroll assembly. It is unknown to what effect but the shaft would transfer heat from the expander to the compressor. This would have a negative impact on performance.

This design also has no easy way to measure the power output of the expander beyond temperature and pressure measurements. If the two housings were separated it would be possible to place a dynamometer between them but this would have increased the number of shaft seals. This design did not allow for the expander to be individually tested.

3.4.2 Roller Chain

In this design the expander and compressor are mechanically connected by a chain and sprocket. The design and two configurations are shown in Fig. 26. Chain assemblies have many positive features such as the ability to connect two or more components that are not in close proximity. They are also standardized and readily available. Their transmission efficiency can be as high as 98% [50].

Configuration 1 has the advantage of not requiring a custom scroll assembly because the two drive shafts rotate in opposing directions. It does have the negative aspect of only partially engaging one of the drive sprockets. An increase in the amount of engagement would require an additional idler sprocket. This would increase the overall size of the device. Configuration 2 is simpler and fully engages both drive sprockets but would require a custom scroll assembly.

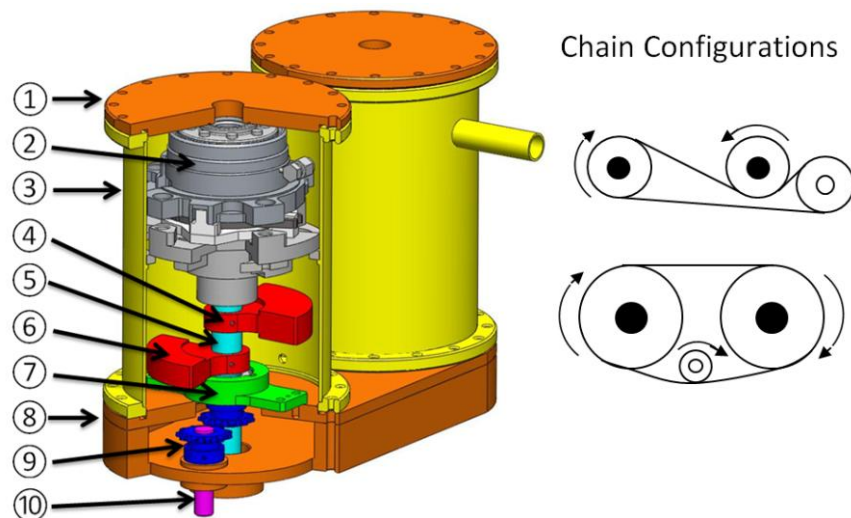


Fig. 26: Partial section view of chain drive (left). Chain configuration 1 (top-right) and 2 (bottom-right). The wheels with the black center are the expander and compressor and the white center is the idler. The chain configuration of the section view is type 1.

Configuration 1 was preferred because it did not require a custom scroll assembly. This design would require three shaft seals, four bearings, three sprockets, and the roller chain. With a single shaft for each scroll assembly a total of four counterweights would be required.

It was thought that a passive lubrication system could be implemented by keeping the chain housing sealed from the expander. A tube could be routed from the expander housing to a lower chamber that housed the bottom of the shaft. The compressor would need no special considerations since it was sealed off from the expander. Like the previous design two shaft seals would experience a low pressure differential but a high surface speed. Individual testing could be achieved by removing the compressor from the chain loop.

We could not conceptualize an easy method to assemble and disassemble the device. It could be accomplished by breaking the bottom cover into several layers but this would increase the number of sealing surfaces. Thermal isolation was another concern because the two assemblies are connected by a large metal plate. This would degrade the performance of the cycle. The chain housing would be large, heavy, and would have likely been expensive to fabricate.

3.4.3 Helical Spur Gears

In this design the expander and compressor are mechanically coupled by helical spur gears. The design and its two configurations are shown in Fig. 27. Helical spur gears were considered because of their ability to operate efficiently at high speeds with low noise [51]. This is due to the gradual loading of the teeth as compared to spur gears which do not. The graduate loading causes a thrust load on the shaft. Gears are known to have efficiencies of 95-97% per set [3].

From the configurations considered 2 was preferred because of the decreased size of the gears. Configuration 1 would require gear diameters of at least 6 [in] which was considered to be too large. This would also cause a high surface speed. Neither of these configurations would require a custom scroll assembly.

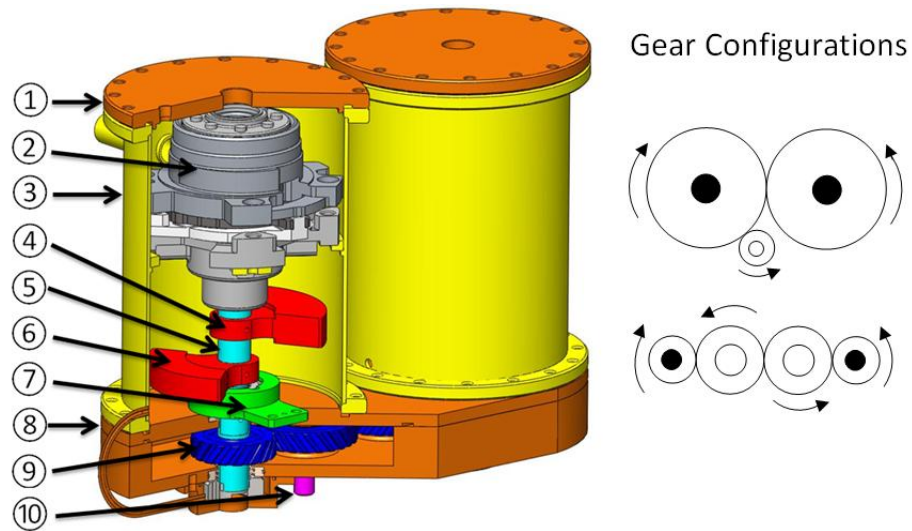


Fig. 27: Partial section view of helical gear drive (left). Gear configuration 1 (top-right) and 2 (bottom-right). The gears with the black center are the expander and compressor while the ones with white centers are idlers. The gear configuration of the section view is type 2.

It would require three shaft seals, six bearings, and four gears. With a single shaft for each scroll assembly a total of four counterweights would be required.

The proposed lubrication system could be passive and is the same design proposed for the chain drive. Individual testing could be achieved through one of the intermittent idler gears and the removal of the compressor gear. This design has the same disadvantages as the chain drive. This design would also weigh more than the chain drive because of the four heavy gears.

3.4.4 Helical Gear-Chain Hybrid

This design combines the advantage of gear sets rotating in opposing directions and the chains ability to couple components that are far apart. The proposed gearing is shown in Fig. 28. This had a few advantages over the pure helical gear and chain systems. This setup would allow for smaller gears to be used and would lead to an overall lighter design. The gear and sprocket stack would cause a larger vertical foot print.

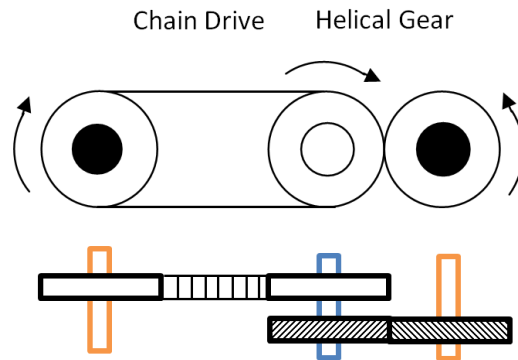


Fig. 28: Interaction between chain and gear components. The top and side views are shown respectively. The orange shafts designate the compressor and expander and the blue is an idler shaft.

It would require three shaft seals, four bearings, two sprockets, two gears, and one chain. With a single shaft for each scroll assembly a total of four counterweights would be required.

The lubrication system would mimic the chain and gear designs. Thermal isolation is still a problem and the bottom housing is still bulky. The power takeoff would be through the idler and the chain could be removed to disengage the compressor. It should have the same order of difficulty in assembly as the chain and gear designs.

3.4.5 Spherical Miter Gears

This design involved using two sets of spherical miter gears to mechanically couple the compressor and expander. The design is shown in Fig. 29. Miter gears are the same as bevel gears but they have a gear ratio of 1:1. Spherical miter gears are like helical spur gears in that they operate with gradual loading instead of impact loading. This gives them lower noise levels at high speeds. Spherical miter gears create both a radial and thrust load on the shaft. The spherical miter gears were expected to be 95-97% efficient per gear set [3].

Miter gears allowed the power takeoff to be placed on the side of the expander. This design would not require a custom scroll assembly.

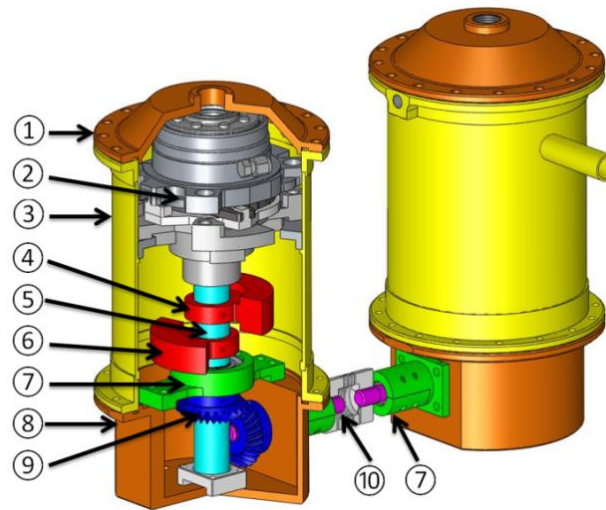


Fig. 29: Partial section view of miter gear drive.

It would require two shaft seals, six bearings, and four gears. With a single shaft for each scroll assembly a total of four counterweights would be required.

By separating the expander and compressor into different housings thermal isolation could be achieved. Assembly would be much easier when compared to the previous designs. The bottom cover, shaft assembly, gears, and power takeoff can be assembled without the housing or scroll assembly. It allowed for individual testing of the expander from the horizontal power takeoff shaft.

It allowed the compressor and expander to be vertically oriented and facilitated the function of the original lubrication system. In hindsight the gear set provided lubrication for the scroll assembly through a misting action. It did have the disadvantage of having the largest number of gears and shaft seal. Spherical miter gears also require positional tolerances in three directions.

3.4.6 Comparison and Selection

A house of quality was used to compare the different proposed transmission systems. It was decided in the design that we would not build a custom scroll assembly. This meant that the direct drive and second chain drive configuration were not considered. The first chain drive was also not included because of the uncertainty in performance of a

partially loaded sprocket. This left the comparison between the helical spur gear, helical gear-chain hybrid, and spherical miter gear.

The values of the engineering requirements were driven by our expert opinion and lessons learned from the 1st and 2nd generation scroll expanders. The full house of quality is shown in Table 10.

Table 10: House of quality for comparison of the helical spur gear, helical gear-chain hybrid, and spherical miter gear designs.

		Engineering Requirements											Competitive Evaluations		Competitive Evaluations		Competitive Evaluations										
		Number of Bearings, Gears/Sprockets, and Shaft Seals			Number of Sprockets and Bearings to be Removed			Machining Tolerances		Component Count		Assembled Weight		Assembled Volume		Electric Generator Implementation		Shaft Work Out (Components Added)		Cost		1	5	1	5	1	5
Units		#	#	#	mm	#	kg	m ³	#	#	\$	Miter Gear		Helical Gear		Helical-Chain											
Customer Requirements																											
1	Efficiency	10	x						x	x		4		3.5		4											
2	Machinability	3			x							3		3		4											
3	Simplicity in Assembly	8		x		x			x			5		3		3											
4	Small Footprint	6						x				5		4		3.5											
5	Low Weight	6					x					5		3		4											
6	Evolvable Design	5							x	x		5		3		3											
7	Cost	2			x						x	4		3		3											
8	Independent Testability	5							x	x		5		3		3											
Targets												207		146		157											

The results of the analysis showed that the spherical miter gear design would best meet our needs. It should operate just as efficiently as the helical-chain design but with easier assembly, a smaller footprint, and lower weight. The lubrication system should function identically to the manufacturers. It is the easiest to individually test.

3.5 Transmission System Development

In order to develop the load bearing components for the spherical miter gears reaction forces had to be calculated along with an FEA analysis to validate structural integrity. Counterweights had to be designed for dynamic balance. Components such as spherical miter gears, bearings, shaft seals, and connectors had to be selected.

3.5.1 Spherical Miter Gears

To minimize the vertical footprint the spherical miter gears were sized as small as possible. The MMSG-25R and MMSG-25L were chosen. The teeth are ground and heat treated to maximize the transferable torque. Brian Dengel [52] from Quality Transmission Components clarified that gears are rated for a torque at a given speed. This equates to a rated power. With the assumption of sufficient lubrication and our estimated loads he calculated that at 3,600 [RPM] the maximum transferable torque for the gear would be just shy of 6 [N-m]. Past this load would result in a surface failure which means that the surface of the gear teeth will deform. This is more than our expected maximum torque of 3 [N-m]. Additional specifications of the gears are given in Table 11 and Fig. 30.

Table 11: Summary of spherical miter gear characteristics where R and L represent teeth direction.

Name	MMSG2-25R
	MMSG2-25L
Type	Ground Spiral Miter Gear
Module	2
No. of teeth	25
Pressure Angle	20°
Tip Angle	49.38°
Pitch Diameter	50 [mm]
Allowable Torque)	25.3 [N-m]

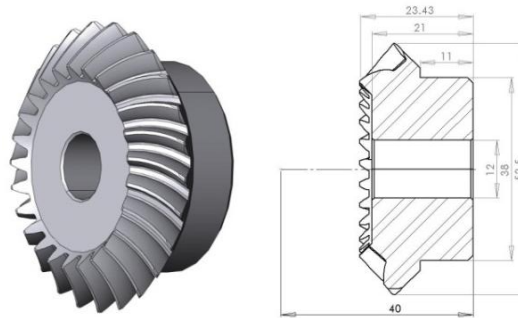


Fig. 30: Spherical miter gear nominal dimensions [mm]. The 40 [mm] represents the mounting distance which is how far the gear should be from the center of the mating gear.

3.5.2 Reaction Force Calculations

With a spherical miter gear selected the reaction forces on the gear tooth were calculated using the design torque of 3 [N-m]. Nominal locations of the bearings were selected to minimize loading without increasing the footprint of the expander. The main shaft bearing location was selected to minimize the size of the counterweights. With these locations a static force analysis was performed to calculate the reaction forces at the bearing locations. These forces would be used in the selection of the bearings. A full summary of the force analysis is given in Appendix A.2.

3.5.3 Bearing Selection

Using the above reaction forces and our environmental conditions the SKF bearing calculator recommended the W6205 stainless steel bearing for the main shaft and the 6201-RSL for the power takeoff shaft. Both bearings are deep groove ball bearings which have low friction, high operating speeds, and ability to handle both radial and axial loads. High temperature PTFE grease was used as a lubricant in the 6201-RSL bearings. The W6205 would be lubricated from the oil inside the expander. The 6201-RSL and W6025 are shown in Fig. 31.

A bearing life analysis was performed to confirm that the bearings would not fail over the course of testing. The analysis showed that the 6201-RSL would have a bearing life

of 1.18×10^6 hours. The W6205 was expected to have a life just as long because it has a higher rated load. The full analysis is shown in Appendix A.3.

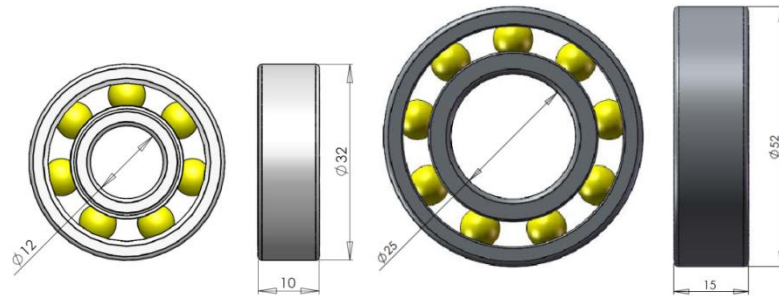


Fig. 31: Nominal dimensions of the 6201 (left) and W6205 (right) bearings. All dimensions are in [mm].

3.5.4 Vertical Bearing Holder Design

The vertical bearing holder is the housing for the W6205 bearing. The bearing is inserted from the bottom because the reaction force calculations in Appendix A.2 showed that a net force occurred in the positive k direction. It is currently made of 6061-T6 and it connects to the bottom cover by four AISI304 $\frac{1}{4}$ -20 sockets. It is raised to keep the vertical profile of the bottom cover minimized by raising the location of the spherical miter gear. There are two $\frac{1}{8}$ [in] pins that keep it in the correct position during installation. An FEA analysis showed that the minimum factor of safety based on a yield strength of 185 [Mpa] was 2.88. A description of the FEA analysis and results for this component are shown in Appendix B.1.

Changing the material of this component to AISI304 or AISI4140 is currently in discussion because of the poor performance of 6061-T6 at elevated temperatures. The above factor of safety accounts for this but it is still a concern. Originally it was thought that the housing would be 120°C at design conditions but current tests have shown it will likely be over 150°C .

3.5.5 Horizontal Bearing Holder Design

The horizontal bearing holder houses the 6201-RSL bearings. It is attached to the bottom cover by four AISI304 ¼-20 sockets. There are two 1/8 [in] pins that keep it in the correct position during installation. It is made of AISI4140. An FEA analysis showed that the minimum factor of safety was 3.28 based on a yield strength of 460 [Mpa]. A description of the FEA analysis and results for this component are shown in Appendix B.2.

3.5.6 Power Takeoff Shaft Design

The power takeoff shaft uses a flat to transfer power from the meshing gears to the compressor. It is also the running surface for the shaft seal. A step in the shaft allows the axial force of the gear to be transferred to the gearing. This shaft has gone through one revision since its initial design. The differences between the original design and the revision are highlighted in Fig. 32.

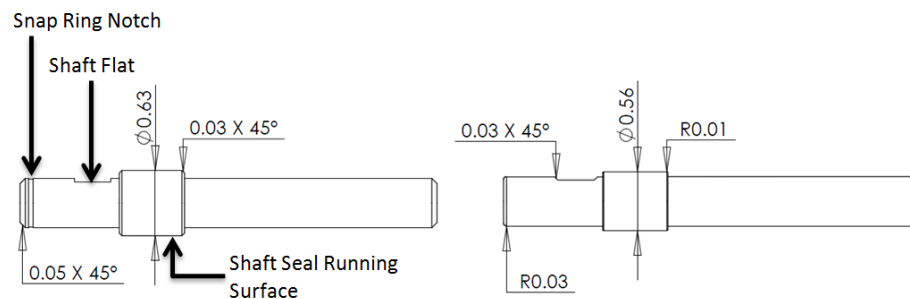


Fig. 32: Power takeoff shaft comparison original (left) and revision (right). All units are [in].

Changes included removal of the snap ring notch, reduction in the diameter of the shaft seal running surface, chamfers on the edges of the flat, and a material change.

A series of shaft seal failures led to the requirement of a shaft redesign. During disassembly the snap ring notch would grab the lips of the shaft seal and damage it. Sharp edges on the flat were also known to do this. The reduction in the diameter of the running surface was done to improve efficiency. Shaft seal losses are a function of surface speed and shaft diameter [53].

The material was the primary reason for the redesign. After a shaft seal failure we became aware of two wear marks on the shaft which coincided with the shaft seal lip locations. An older shaft that was still in service was examined and it showed extensive wear. The shaft seal had actually conformed to the grooves it had created on the shaft. The extent of the damage is shown in Fig. 33.

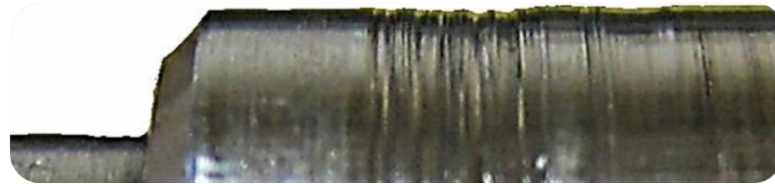


Fig. 33: Extensive wear caused by a Teflon shaft seal on the original power takeoff shaft.

The shaft seal is made of Teflon and at high speeds it is abrasive to soft metals. The original shaft was AISI304 stainless steel which had an 80 Rockwell B hardness [54]. American High Performance Seals specifies that a 55-60 Rockwell C hardness is ideal for shafts that experience moderate to high speeds. This is why 440C stainless steel was selected because it has a 60 Rockwell C hardness [54]. The majority of the testing has been performed using the older shaft.

3.5.7 Shaft Seal

Given our operating conditions American High Performance recommended a SB40 ekonal impregnated Teflon shaft seal. It is a double lipped seal and is meant to handle moderate speeds and pressures. The shaft seal is inserted into the bottom cover from the inside which is shown in Fig. 37. It is held in place by the pressure differential from the pressure inside the expander.

Beyond the aforementioned failures caused by excessive wear the seal also failed from excessive pressure. In the bottom cover the shaft seal has a large unsupported span which decreases its pressure rating. This causes the lips of the seal to push out which is shown in Fig. 34. With the redesign of the power takeoff the seal had to be redesigned as well. To reduce the chances of future failures a washer was placed in front of the shaft seal for increased support of the unsupported span. This is also shown in Fig. 34.

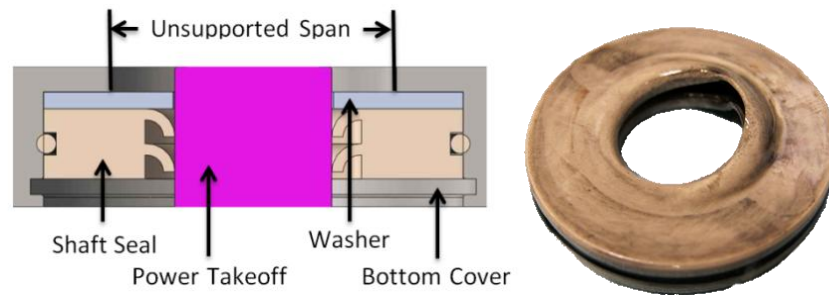


Fig. 34: Shaft seal in the bottom cover with washer for unsupported span (left) and failure caused by excessive pressure (right).

There have not been any shaft seal failures since these changes have been implemented. As an additional precaution a pressure relief valve that was set to 110 [psi] was attached to the expander outlet.

3.5.8 Connections

Dowel pins and set screws were used to attach components to the shafts. All components that did not have to be removed were attached with dowel pins. This included both counterweights and the gear on the main shaft. The pins were 1/8 [in] steel. The factor of safety for the pin in the gear was calculated to be 60. A set screw was used with the spherical miter gear on the power takeoff shaft. The gear has to be removed to access the shaft seal. The set screw is steel, has a knurled end, and is a ¼-20 thread. The holding torque of the set screw is 9.83 [N-m] which is three times our design torque.

The top cover, bottom cover, and bearing holders are all connected with AISI304 ½-20 socket screws. It was determined that the minimum thread engagement was 0.183 [in]. The top cover experiences a load of 1,999 [lbf] which is distributed between 8 screws. An analysis was performed to validate the integrity of this connection. With a pre-torque of 7.5 [N-m] the load factor of the screws is 15.7 and the factor of safety from member separation is 3. If insufficient pre-torque is applied and the members separate causing the screws to take the entire load the factor of safety is 2.38. It was found that all screw connections would not fail at design conditions. A full summary of all the connections is given in Appendix A.4-A.10.

3.5.9 Balancing

Balance can be both static and dynamic. A shaft can be statically balanced without being dynamically balanced. A dynamically balanced shaft will consist of at least three rotating masses. These masses rotate at the same speed and therefore the force they exert is only a function of mass, radius, and their distance along the shaft. The design goal of a counterweight is to maximize the amount of mass radially. This will minimize its total weight.

To calculate their masses you take the sum of the moments about one counterweight location and do the same about the other. The largest counterweight (lobe) will be rotated 180° from the imbalanced mass. It is meant to statically balance the imbalanced mass. The distance between them should be minimized. The smaller lobe is aligned with the imbalanced mass and counters the resulting moment caused by the imbalanced mass and larger lobe. A full summary of calculations used in the design of the counterweights is provided in Appendix A.1.

Calculations are not always enough to ensure smooth operation. There are several imbalance effects that are caused by machining tolerances, inertia, and bearings. Any rotating machine will also resonate at a specific speed range [50]. It is due to these factors that we had our shaft balanced by OTS Wire. The act of balancing is done by oversizing the counterweights and then correcting the masses with a balancing machine. With a 10% oversize the large and small counterweight had masses of 385.6 [g] and 288.5 [g] respectively. Balancing ensures that the rotating shaft will operate smoothly at its rated speed. The shaft was balanced for a speed of 3,600 [RPM]. This speed comes from the two pole induction motor inside the compressor, which operates at a synchronous speed in accordance with an electrical frequency of 60 [Hz].

The assembly that was sent to OTS is shown in Fig. 35. In order to replicate the operating conditions of the shaft the rollers of the balancing machine are placed at the bearing locations. This is labeled as bearings 1 and 2. There is a notch cut out of the shaft at bearing 1 and a sleeve had to be fabricated to provide a smooth running surface. The step is meant to prevent the lobe from striking the rollers. Bearing 2 was too small for the roller

and as a compromise the roller was placed past the gear. The scroll and knuckle bearing were epoxied to the shaft. The shaft was balanced to a tolerance of 0.3 [mills] [55].

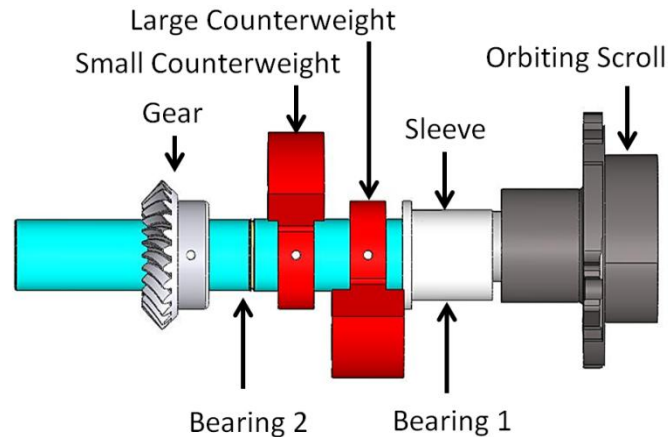


Fig. 35: Shaft assembly sent to OTS Wire for balancing.

There were speeds during testing at which the expander would appear to be poorly balanced. At certain speeds we would approach the natural frequency of our device which would cause it to violently shake. This occurred close to 2,800 [RPM]. OTS mentioned that a method to reduce this effect and change the natural frequency of the device was to add shock absorbers to the fixture the expander was attached to. This addition reduced the effect of resonance.

3.6 Lubrication System Development

Proper lubrication has been a continual priority since the 1st and 2nd generation scroll expanders. A primary goal of this design was to ensure the optimal function of its lubrication system. The miter design added an additional complication of requiring lubrication for the mating gears. This section evaluates the design of the lubrication systems for both the scroll components and the gear set. Two oils were tested. The lighter oil manufactured by Exxon Mobile was named EAL ARCTIC 32 and had a viscosity of 5.8 [mm²/s] at 100°C. The heavier was manufactured by CPI Engineering Services was named SOLEST-370 and had a viscosity of 29.2 [mm²/s] at 100°C. These oils were chosen for their compatibility with the refrigerants used. It was estimated that the oil entrained into the working fluid is 3-5% by weight.

3.6.1 Gear Lubrication

To ensure efficient operation the gears need to be lubricated. The effective lubrication of mechanical components can be accomplished by bath or spray-mist methods. These are illustrated in Fig. 36.

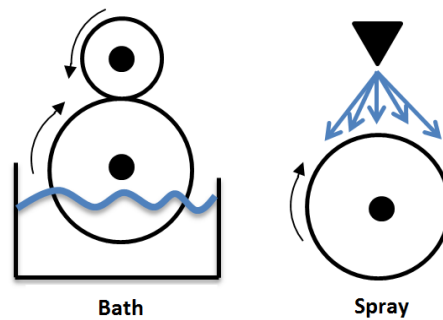


Fig. 36: Lubrication methods; the black center represents a drive shaft.

Bath lubrication has part of the gear submerged in a pool of oil. It is important to not submerge the entire gear in oil as it causes unnecessary viscous drag. Spray or mist lubrication generally uses an active system to continuously supply a stream of lubricant. Mist lubrication is considered the most effective method because of the even coating it applies.

It was desirable to implement a passive system and therefore spray and misting methods were disregarded. Bath lubrication coincided with the oil sump required by the lubrication system implemented by the scroll manufacturer and the horizontal orientation of the spherical miter gear. Oil naturally pools in the bottom cover as it condenses during expansion of the working fluid. The bottom cover is shown in Fig. 37

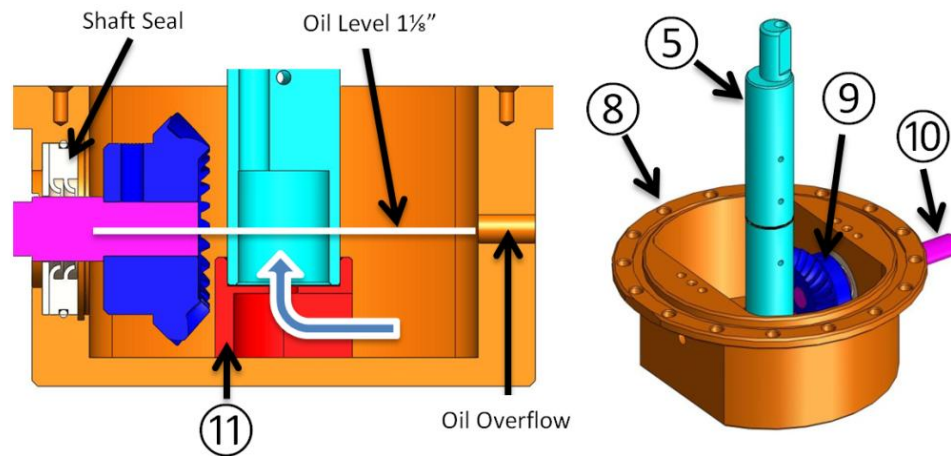


Fig. 37: Bottom cover assembly with horizontal miter gear, artificial sump, power takeoff shaft, and main shaft. It also shows the oil height in the bottom cover as well as oil flow into the shafts oil pump.

In hindsight it was found that the spherical miter gears have an oil misting effect. This was found by externally powering the expander while the top cover was removed. A light mist of oil was observed coating the scroll assembly. It is unknown how this mist behaves during operation but we believe it may have a positive effect. Another unforeseen benefit of the sump was that metal fragments that had made their way into the system would get stuck at the bottom of the sump.

3.6.2 Scroll Lubrication

The manufacturer has already devised a system that effectively lubricates the scroll components and it was decided to replicate their system shown in Fig. 23. In the compressor the lower journal bearing was an important component in the oil pumps function. To replicate the lower journal bearings function the artificial sump was designed. It is shown in Fig. 38. It is not a load bearing component and was designed out of aluminum to minimize weight. The bolt holes are oversized to encourage the shafts suction effect to pull up the artificial sump and form a seal. The inlet for the oil is placed opposite to the side facing the spherical miter gear in an effort to minimize its effect.

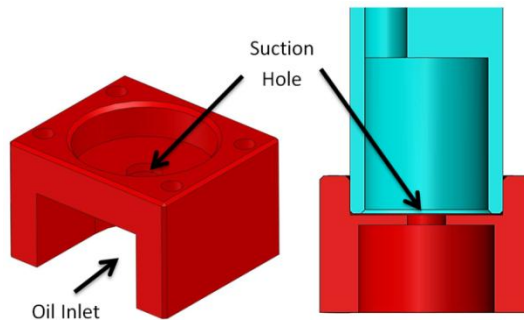


Fig. 38: Artificial sump and section view of artificial sump and shaft.

In hindsight it should be noted that high weight oil should not be used with this lubrication system. It was originally thought that the elevated temperatures of the expander would cause a heavier weight oil to become less viscous. Upon opening the expander after several tests with the heavier oil it was found that the entire scroll assembly was dry. The heavy wear caused to the orbiting scroll is shown in Fig. 39.



Fig. 39: Extensive wear to orbiting scroll caused by insufficient lubrication.

The heavy oil was replaced with a lighter one and new scroll components were purchased. We have found that the damaged scroll components have retained their performance after some break-in time and a functioning lubrication system.

3.6.3 Lubrication System Validation

A test of the above lubrication system was performed to confirm its effectiveness. It was meant to quantify the effect of initial oil height, the impeller, and shaft speed. The shaft was powered by an electric motor with a speed controller.

To collect data a guard was placed around the entire shaft with a vertical section missing. Oil was collected from this vertical section over a period of time and then weighed. The speed was approximated by the power level of the controller and the motors maximum speed. The mass flow rates were then normalized by the largest calculated mass flow rate of 2.94 [g/s]. Only the lighter oil was used in this testing. The results are shown in Fig. 41.

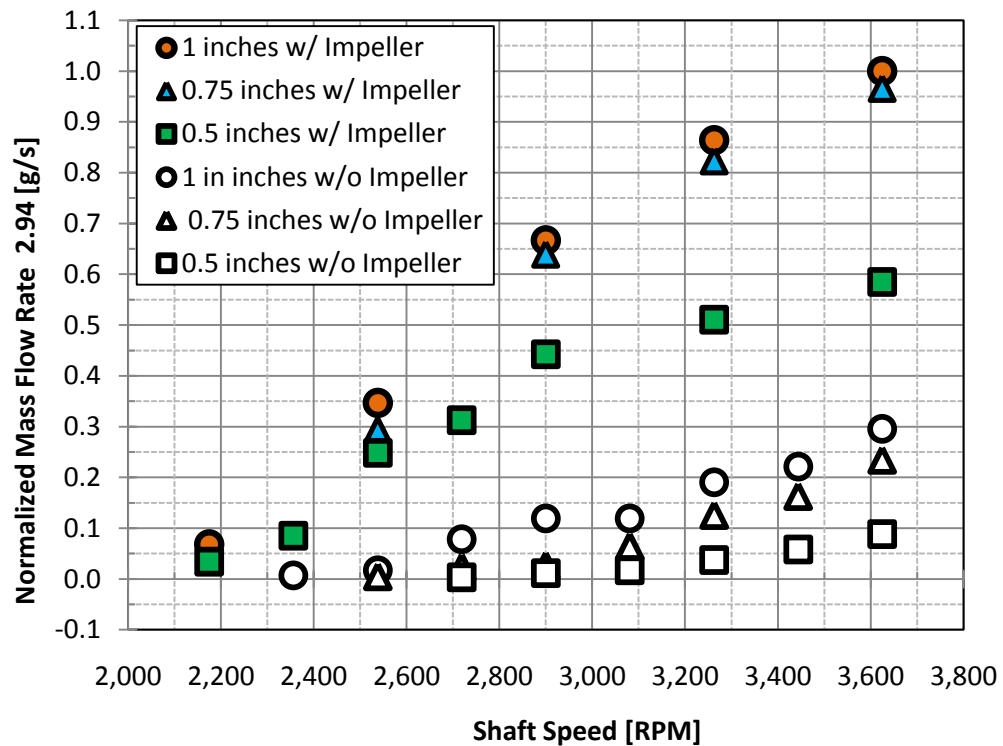


Fig. 40: Qualitative oil mass flow rate out of the shaft as a function of shaft speed. Solid shapes signify that an impeller was used. In the legend the number represents the height of the oil in the bottom cover (refer to Fig. 37 for reference).

The results show that the impeller has a strong effect on the mass flow rate of the oil. At 1 [in] the lack of an impeller resulted in a 70% reduction in mass flow rate. At some point between the 0.5 and 0.75 [in] heights the oil mass flow rate becomes a weak function of oil height. It was decided to place the oil overflow 0.75 [in] above the bottom of the bottom cover to ensure maximum performance.

3.7 Seal Piston Engagement

It was aforementioned that engaging the sealing piston was a design challenge when operating the scroll compressor as an expander. There are two aspects of this problem. One is the initial engagement of the piston as well as maintaining the proper pressure for optimal performance. To overcome these challenges a port was placed on the side of the stationary scroll that fed into the expander inlet pressure. It was found that this was sufficient to control the piston pressure with a needle valve but it was not always capable of starting the expander. In order to start the device a ball valve would be closed to raise the pressure and then opened. This adds bulk and complexity to the system and requires manual intervention which is not ideal.

We needed to find a way to passively raise the piston. A novel idea to solve this was by placing small springs inside the piston chamber. The piston chamber is shown in Fig. 22. We have found that four springs is sufficient to start the expander. This solution made the scroll expander self-starting.

3.8 Part Modifications

To reduce fabrication costs the housing from the 2nd generation expander as well as the top cover used in the 1st and 2nd generation expander were modified. These modifications were done to reduce the weight of the device.

3.8.1 Tube Assembly

The largest contributors to weight in the 2nd generation housing were the tube assembly flanges and scroll support. The changes are highlighted in Fig. 41. The top and bottom flange as well as the scroll support height were reduced but the overall height remained the same. The flange thickness remained larger than the minimum thread engagement. The lower wall thickness was reduced to 0.1 [in]. This resulted in a 44% reduction in weight.

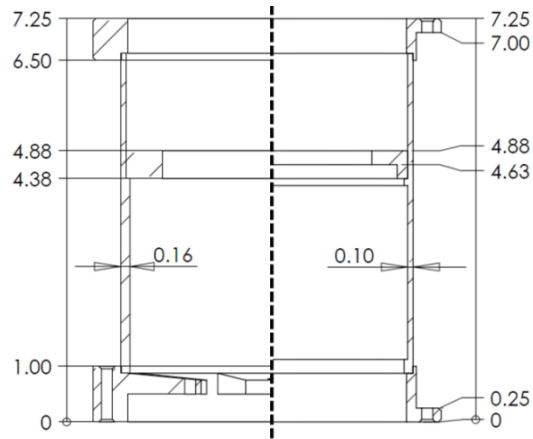


Fig. 41: Changes made to the 2nd generation expander housing. 2nd generation (left) and 3rd generation (right). All units are in [in].

The entire assembly is made of AISI304. Solidworks Simulation was used to perform an FEA analysis on this assembly to validate its structural integrity. The largest stress occurs in the tubing near the scroll support. This is caused by the high pressure vapor inside the scroll assembly exerting a downward force. Other forces include a pulling action caused by the top and bottom cover as well as a 66 [psi] differential. The minimum factor of safety was calculated to be 4.58 based on a yield strength of 206.8 [Mpa]. The full FEA analysis and engineering drawings can be reviewed in Appendix B.4 and C respectively.

3.8.2 Top Cover

The top cover was a particularly heavy component. The wall thickness was changed to a uniform thickness of 0.25 [in]. This resulted in a 50% reduction in weight. Changes between the 1st and 3rd generation cover are highlighted in Fig. 42.

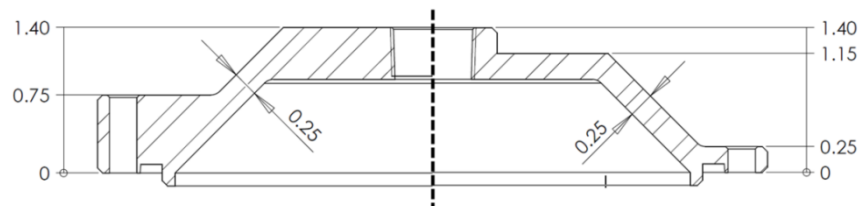


Fig. 42: Changes made to the 1st generation expander top cover. 1st generation (left) and 3rd generation (right). All units are in [in].

The top cover is made of AISI304. Solidworks Simulation was used to perform an FEA analysis on this part. This component is exposed to a 66 [psi] and a 386 [psi] pressure differential. The scroll pressure also exerts a force on it. The analysis shows that the surfaces under the heads of the screws are likely experiencing a small amount of yielding. This will not compromise the integrity of the part. In locations not directly under the screw the factor of safety is either 2.5 or greater based on a yield strength of 206.8 [Mpa]. It should be noted that the tensile strength of AISI304 is 517 [Mpa]. The full FEA analysis and engineering drawings can be reviewed in Appendix B.3 and C respectively.

3.9 Final Design

With the above analysis the expander was designed and fabricated. The entire expander assembly along with a descriptive section view is shown in Fig. 43. After the completed design and a few revisions we managed to fabricate a reliable and self-starting scroll expander. It had an effective lubrication system which is shown in Fig. 44. It also was dynamically balanced with two counterweights which are also shown. Spherical miter gears provided an efficient and quiet method for power transmission. The next step was to demonstrate the expander in an ORC and quantify its performance. The complete engineering drawings of all the components can be reviewed in Appendix C.

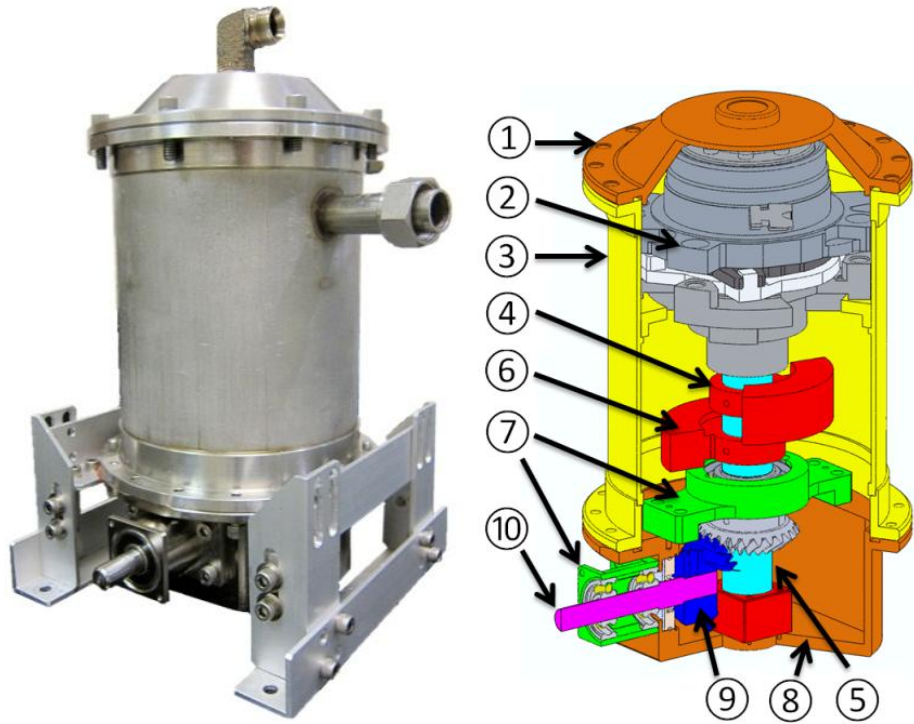


Fig. 43: Expander assembly built and partial section.

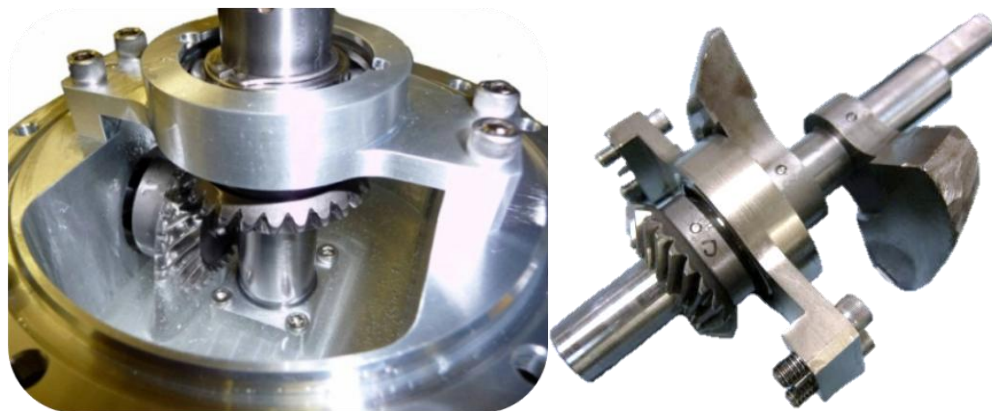


Fig. 44: Expander lubrication system (left) and shaft assembly (right).

4 EXPERIMENTAL SETUP

To measure the performance of the expander two test beds were used. Both are ORCs but the first test bed is ideal for expander testing. The second is primarily for HAC but is capable of measuring expander performance. In order to accurately calculate the efficiency of an expander a dynamometer is required. This measures the torque, speed, and power output. The temperature and pressure before and after expansion also have to be measured. Mass flow is another required measurement. Below is an explanation of the equipment used in the different test beds.

4.1 Modified Organic Rankine Cycle Test Bed

The modified organic Rankine cycle (MORC) test bed was used to test both the 1st and 2nd generation scroll expanders. It contains all the components of a basic Rankine cycle except a pump. Instead a compressor is used. In this cycle the working fluid never condenses because the primary purpose of the test bed is to measure expander performance. In this setup the speed of the expander can be controlled by changing the hysteresis brake torque on the dynamometer. The component diagram is shown in Fig. 45. The expander is mechanically coupled to the dynamometer by a helical shaft coupler.

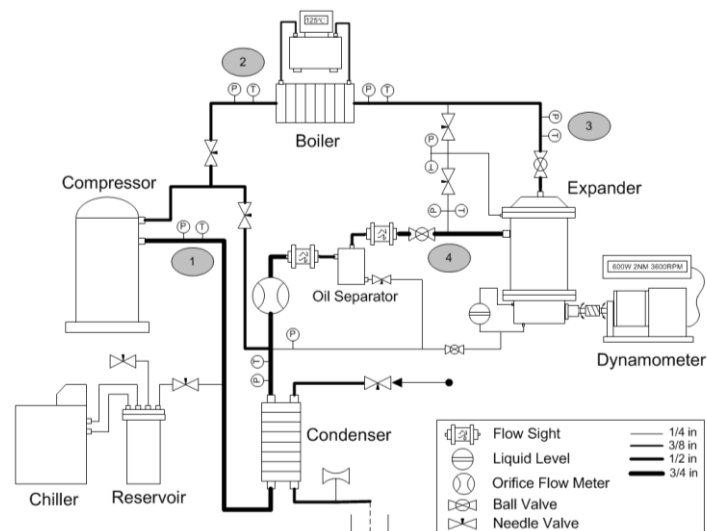


Fig. 45: Diagram of the ORC Test Bed.

To calculate the performance of the expander the only required measurements are the power, mass flow rate, and temperature-pressure before and after expansion. Additional data such as the speed, torque, piston seal pressure, and oil level in the bottom cover will also be collected. The relevant equipment to expander testing is described below:

Dynamometer: The dynamometer is manufactured by Magtrol and its model number is HD-715-8N-4831. It has a rated torque of 6.5 [N-m], maximum continuous power rating of 3 [kW], and a maximum speed of 25,000 [RPM]. It is a hysteresis brake type and is able to develop torque independent of speed. It has a tolerance of 0.25% to 0.5% of its full torque rating. The output and control module is the DSP6001. It sets the break torque and measures power, torque, and speed. Prior to taking measurements the dynamometer was calibrated but had an offset of 0.5 [N-m]. This is not a problem because it still outputs the correct torque at load.

Thermocouple: Type K thermocouples with special limits of error were used. They have a temperature range of -200-1,250°C and its special limits of error are 1.1°C or 0.4%.

Pressure Transducer: The pressure is measured with an Omega PX315-200GI at the expander outlet and an Omega PX315-500GI at the inlet. The PX315-500GI and PX315-200GI have pressure ranges of 0-500 [psi] and 0-200 [psi] respectively. They are both active transducers and have 0.25% full scale accuracy. Additionally they were calibrated with a digital pressure gauge to an accuracy of $\pm 0.05\%$ (of full scale range) or ± 1.7 [kPa].

Mass flow meter: An orifice plate manufactured by Lambda Square Inc. directly measures the volumetric flow rate. The entrance length before the meter is sufficiently long to assume fully developed conditions. A thermocouple and pressure transducer placed directly below the orifice is used to derive the density. With the density and volumetric flow rate the mass flow rate can be calculated. The accuracy of the orifice according to the manufacture is $\pm 0.6\%$ of its full scale reading.

4.2 Heat Activated Cooling System

In this setup the expander is placed in a HAC system. This system can measure expander performance because of an in-line dynamometer between the compressor and

expander. A major difference between this setup and the aforementioned is that in this setup the speed of the expander cannot be controlled. The component diagram is shown in Fig. 46. The expander is mechanically coupled to the torque sensor by an Oldham coupler. The previous helical coupler failed from excessive parallel misalignment which reduced its rated load.

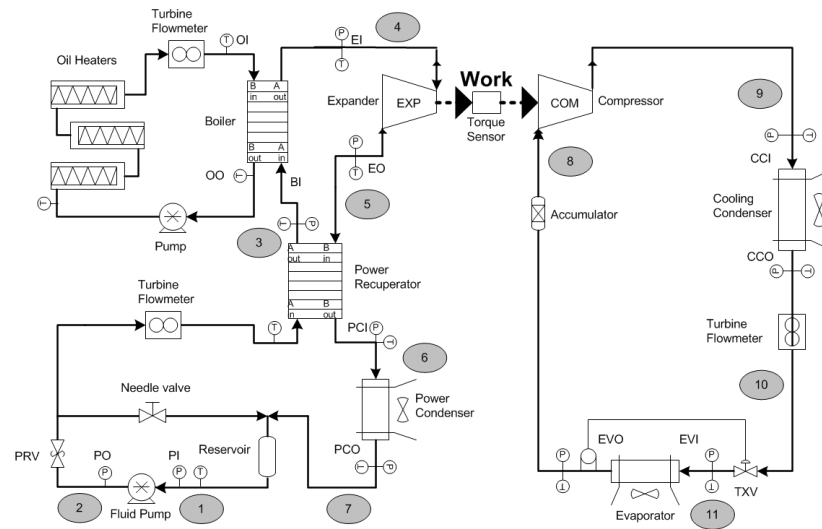


Fig. 46: Component diagram of the HAC system.

The same type of data is collected as in the ORC test bed except for the oil level.

Dynamometer: The expander speed and torque were measured by a Futek torque sensor model TRS 605 which has a rated torque capacity of 10 [N-m]. Its maximum speed is 7,000 [RPM]. The power was calculated from the product of torque and speed. It has an accuracy of ± 0.105 [N-m].

Thermocouple: Type K thermocouples with special limits of error were used. They have a temperature range of -200-1,250°C and its special limits of error are 1.1°C or 0.4%.

Pressure Gauge: All pressure transducers with inherent 0.25% accuracy were calibrated against a digital pressure gauge with an accuracy of $\pm 0.05\%$ (of full scale range) or ± 1.7 [kPa].

Mass Flow Meter: The mass flow rates for both the power and cooling sides were measured by turbine flow meters made by AW Company model TRG-11.300-5 which have an accuracy of $\pm 1\%$ of the measured flow.

5 DATA REDUCTION AND UNCERTAINTY

To ensure the accuracy of the calculated efficiency of the expander a design stage uncertainty analysis was performed for each of the different experimental test setups. The uncertainty analysis was focused on bias error introduced by the instrumentation because random errors are minimized through averaging at each operating point. In accordance to the theory of error propagation the root-sum-square methods proposed by Kline and McClintock [56] were used to combine the individual errors. The total uncertainty in a measurement can be described by

$$W_x = \sqrt{B_x^2 + P_x^2} \quad (11)$$

where B_x is the contribution from bias error and P_x is from random errors. A summary of the total error in the expander isentropic efficiency is given in Table 12.

Table 12: Design stage uncertainties of several quantities for each test bed.

	Efficiency	Temperature	Pressure
ORC Test Bed	±3.19%	±1.1°C	±1.38 [kPa]
HAC Test Bed	±6.98%	±1.1°C	±0.34 [kPa]

A full summary of the design stage uncertainty analysis is given in Appendix A.11. After data collection the ORC test bed showed a range of uncertainty in isentropic efficiency between 3-5% while the HAC ranged between 6-9%.

6 RESULTS AND DISCUSSION

In order to evaluate the efficiency and performance of the scroll expander over a variety of operating conditions a series of tests were conducted by varying expander inlet pressure, rotational speed, seal piston pressure, and oil level. From previous experience with constrained scroll expanders it has been shown that their performance has a linear relationship to speed [6]. At increased speeds the vapor has a decreased amount of time to escape between the small gaps between the scroll wraps illustrated in Fig. 20. It was of interest to confirm that an adequate seal piston pressure would minimize these losses.

The results presented come from a variety of sources. This includes different test setups and expander modifications. All data from 2007 is from the 1st generation scroll expander on the MORC test bed. Data from 2009 is from the 3rd generation scroll expander on the ORC test bed. This set used the larger power takeoff shaft which is the primary reason for the isentropic efficiency of the 2009 data being lower than the 2010 data. The larger shaft and poor surface conditions caused excessive friction. The 2010 data is for the 3rd generation scroll expander and was collected from the HAC system. Data from 3/17/2010 and on were outfitted with the smaller power takeoff shaft which significantly increased the efficiency.

It was established that there is an optimal piston pressure which minimizes the leakage without creating excess friction. Through testing it was found that the power output of the expander is maximized for a range of seal piston pressures. A 220 [psi] inlet pressure will operate optimally with a piston pressure range of 109-125 [psi]. Lower values will cause the piston seal to drop which will result in blow through and larger values will have a negative impact on performance from excessive friction. Once the piston pressure is set it will dynamically change for varying inlet pressures to its optimal value. A quantitative measure of the seal pistons effect on performance can be seen in [48].

It was found through the aforementioned results in Fig. 40 that the lubrication system could deliver sufficient oil to the journal bearings at speeds varying between 2,500-3,600 [RPM]. It was also observed while powering the scroll expander externally at 3,600 [RPM] with the top cover removed that the gear mesh creates a misting lubrication effect.

Additionally the oil indicator allowed the amount of oil in the bottom cover to be monitored during testing and it was concluded that the oil height had no observable effect on performance. To keep the oil height high the oil overflow port was kept closed.

The shaft seal is a component in the expander that requires break-in and over time the performance of the expander will increase given a sufficient amount of run time. A chronological record of efficiency during testing on the HAC system after the power takeoff shaft was replaced is shown in Fig. 47.

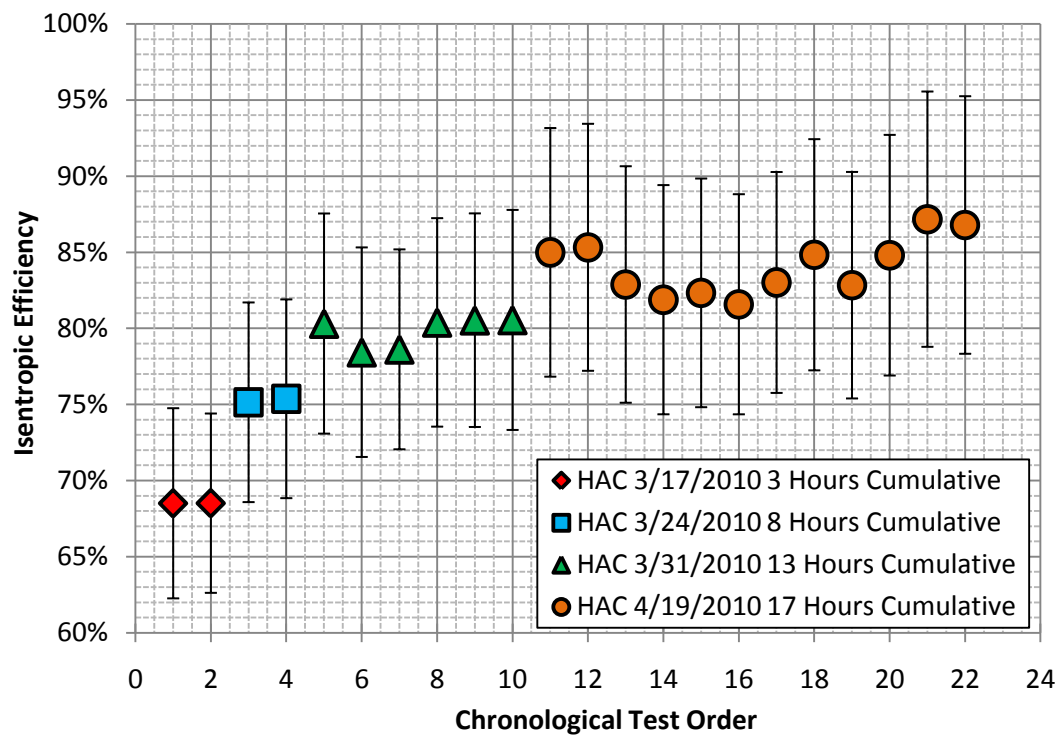


Fig. 47: Expander isentropic efficiency as a function of break-in period with $Pr=4\pm 0.2$. The speed was not kept constant. Each data set is given in chronological order for the date of data collection.

Both pressure ratio and speed were kept to a specific range for comparison. The fluctuations in each data set are likely from varying parameters such as refrigerant charge, expander rotational speed, and compressor load. The different data points in each set were not taken consecutively. The increasing average of each data set indicates that the expander has not

been fully broken-in even after 13 hours of runtime and further testing could yield higher efficiencies.

The impact of the larger power takeoff shaft and its damaged running surface on performance is quantified in Fig. 48. The new shaft with a new shaft seal with no break-in achieved efficiencies 9-15% higher than those with the older shaft. This shows why the performance of the expander on the ORC test bed, which was subjected to a similar break-in period, had lower isentropic efficiencies. If those tests were repeated it would be expected to achieve performance levels similar to those taken on the HAC system on 4/19/2010.

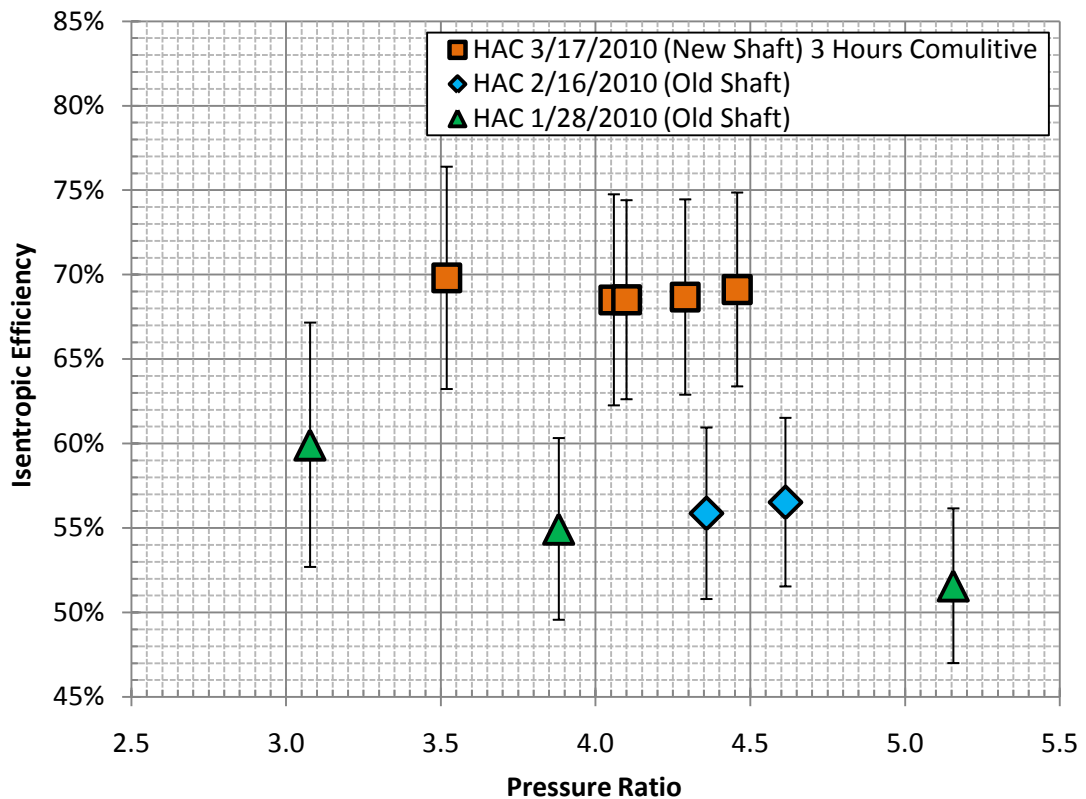


Fig. 48: The data for 1/28/2010 and 2/16/2010 was taken with the damaged shaft and the 3/17/2010 is taken with the new shaft. The changes are highlighted in Fig. 32. The data for 3/17/2010 has only 3 hours of cumulative break-in.

The isentropic efficiency of the expander as a function of speed is shown in Fig. 49. No data from the 2010 tests are shown because the speed of the expander cannot easily be controlled in the HAC system. The data suggests that there is a slight upward trend with

speed but provides an overall flat profile. Wang et al. [48] who fabricated the 1st generation expander observed the same trend. A different scroll expander built by Manolakos et al. [57] gave the same performance characteristics. They observed that the efficiency was a weak function of speed in the range of 750-3,300 [RPM] but out of that range it had a significant negative impact. The pressure drop across the expander was kept constant at 13 [bar].

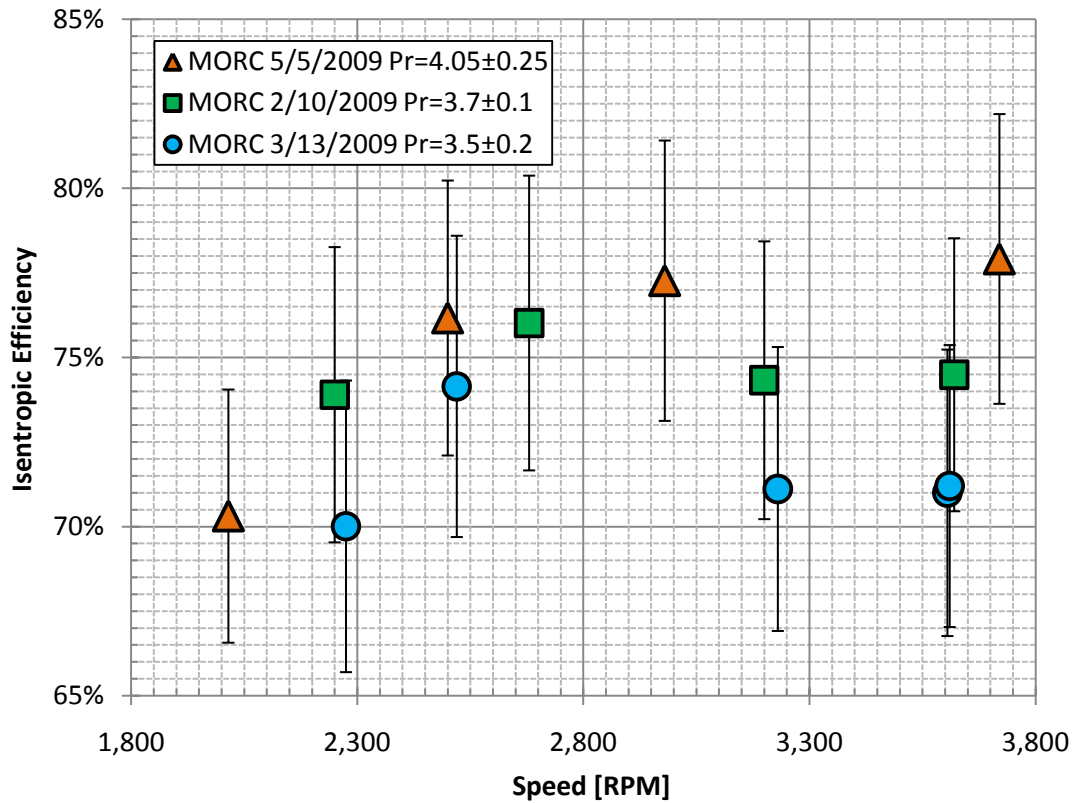


Fig. 49: Expander efficiency versus shaft speed for 3rd generation expander.

In contrast constrained scroll expanders have a dependence on speed because this decreases the time for the vapor to escape through the small spacing between the scroll wraps. This behavior was observed by Peterson et al. [6] and Guangbin et al. [49]. A double-sided constrained scroll expander tested by Kim et al. [43] using steam as the working fluid observed an increase in volumetric efficiency with speed but the overall efficiency remained constant.

The power output and mass flow rate as a function speed is shown in Fig. 50. Since the scroll expander is a positive displacement machine the speed and mass flow rate are

proportional. This explains why the expander power output increases with increasing speeds. The performance of the data sets can be evaluated by comparing the power output to the mass flow rate. The 5/5/2009 data set had the longest break in period but due to a non-ideal pressure ratio it has a lower performance when compared to the other two. The difference between the 2/10/2009 and 3/31/2009 data sets is more complicated. During the 2/10/2009 tests an oil overflow valve was opened which boosted the performance by reducing the back pressure on the expander. This is likely the primary cause for the performance of the 2/10/2009 data being higher than the 3/31/2009 data set which had a longer break-in and would be expected to have higher performance.

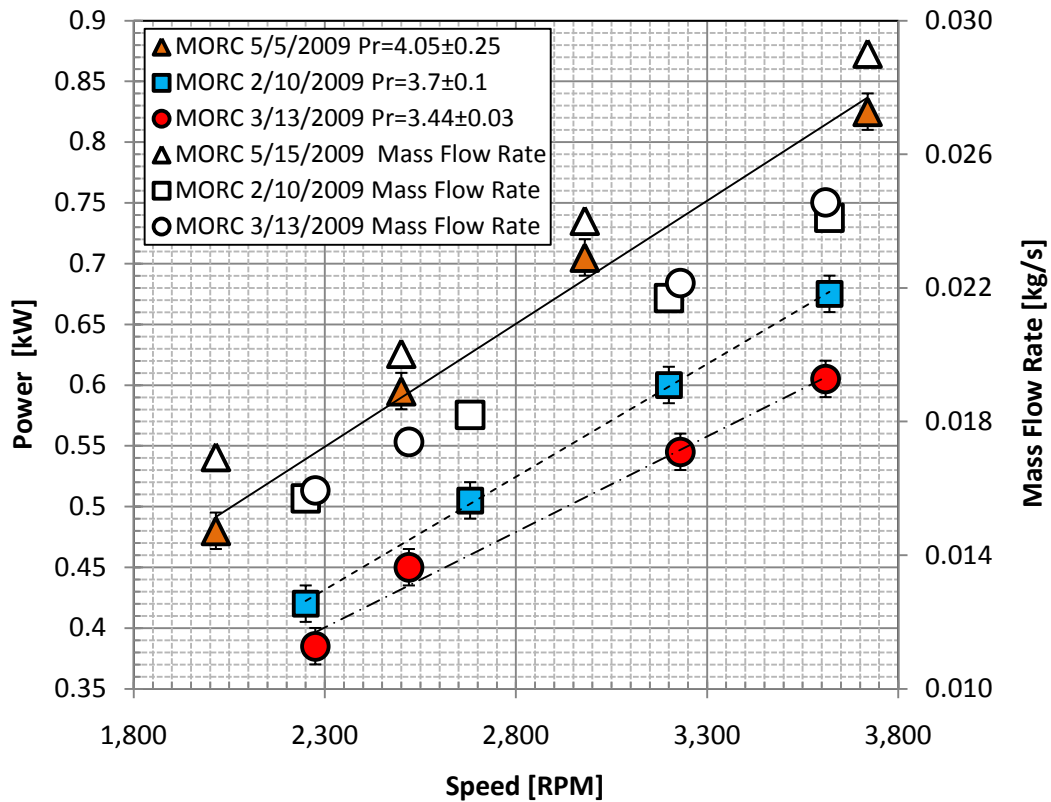


Fig. 50: Expander power output versus speed as well as mass flow rate versus speed.

The effect of pressure ratio on the expander efficiency is shown in Fig. 51. Positive displacement machines have fixed expansion ratios [6] which means that they will operate most efficiently at an ideal pressure ratio. This is why we see the peaking behavior near the pressure ratio of 3.5 for the 3/31/2010 and 3/13/2009 data. In contrast the 7/23/2007 data

has a flatter profile. This discrepancy in performance is odd because both expanders use the same scroll assembly and are expected to have similar performance profiles. It is true that the speeds over the measured pressure ratios vary more significantly in the 2007 data but as it was earlier concluded the efficiency is a weak function of speed. The gearing, bearings, and lubrication system are a significant change over the 1st generation expander but the exact cause of the discrepancy is unknown. It should be noted that the flat profile was unexpected even to the authors of the data [48].

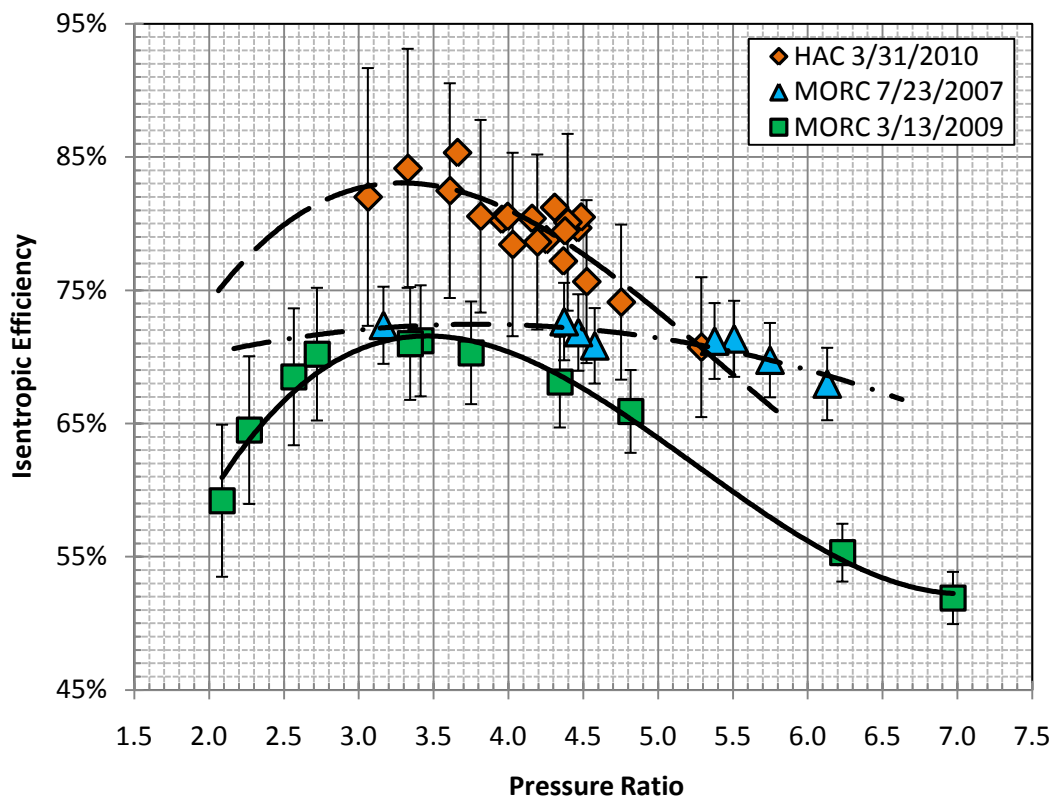


Fig. 51: Expander isentropic efficiency as a function of pressure ratio. Speed is mostly kept constant but to achieve a high pressure ratio the speed had to be decreased. The 7/23/2007 data is extracted from [48].

Overall the 2009 and 2010 data show that the 3rd generation expander can achieve a high isentropic efficiency over a wide range of pressure ratios ranging from 2.09 to 5.29. This shows another advantage over constrained scrolls which have a negative relationship with increasing pressure ratios because of the increase in leakage [48]. Both performance profiles

of the 2009 and 2010 data resemble asymmetric bell curves and agree which is expected. The profiles do show that the expander efficiency is more sensitive to over-expansion than under-expansion. This behavior is predicted by a model of a scroll expander developed by Lemort et al. [45]. The thermodynamic process of non-ideal expansion in a thermodynamic cycle is illustrated in Fig. 52.

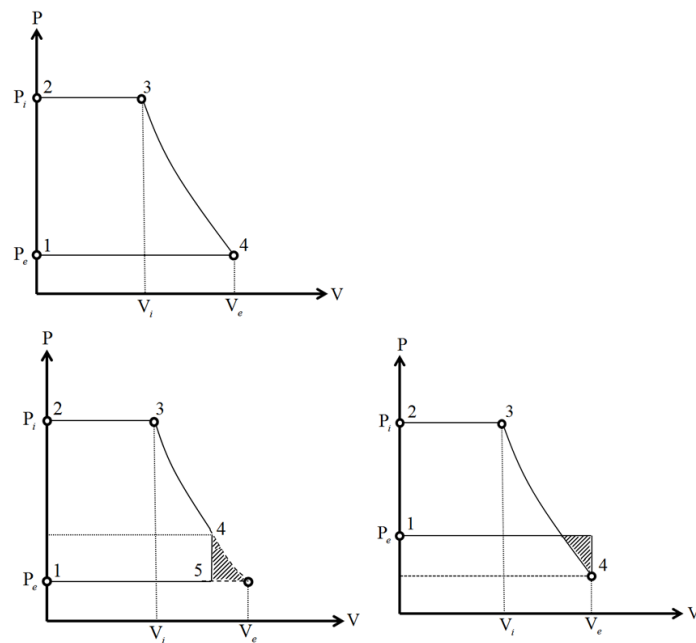


Fig. 52: Counterclockwise: Ideal expansion, under-expansion, and over-expansion. Points 3-4 represent expansion.

In under-expansion the fluid exiting the expander is at a pressure higher than P_e which results in the fluid expanding outside the expansion volume and not providing any useful work. In over-expansion the fluid is brought to a pressure below P_e . When the fluid exits the expander it compresses to match P_e . The expander is more sensitive to over-expansion because in that case the expander has to perform work to expand the gas below P_e . It is analogous to having excessive back pressure. In under-expansion the work is lost but it is not subtracted from the total work. Another factor involves the ideal pressure being close to unity. As it approaches this value the work extracted will approach zero. We see in Fig. 51 that the efficiency is equally sensitive to over and under-expansion with small variations in pressure ratio.

There are two ways to calculate the pressure ratio that correlates to the ideal expansion of a device. The most commonly known is the polytropic relationship which can describe most expansion processes [4]. A polytropic process can be described by the relationship

$$PV^n = \text{constant} \quad (12)$$

where n is a constant for a particular process. The parameter n must first be empirically calculated from a plot such as Fig. 51. This isn't the most useful quantity because it is a function of heat loss and can change with different mass flow rates. The second and more useful quantity is the EM_{ratio} which is used by Mathias et al. [42] to describe the optimal operating conditions for a gerotor and scroll expander. The EM_{ratio} is given by

$$EM_{\text{ratio}} = \frac{\left(\frac{v_3}{v_4} \right)_{\text{fluid}}}{\left(\frac{V_{\text{inlet}}}{V_{\text{outlet}}} \right)_{\text{expander}}} \quad (13)$$

where v_3 and v_4 are the specific volume of the working fluid at the inlet and outlet respectively. Ideal expansion will occur when the ratio of the specific volumes at the inlet and outlet match the fixed volumetric ratio of the device which is represented by an EM_{ratio} of unity.

For comparison the EM_{ratio} as a function of pressure ratio is shown in Fig. 53. It normalizes values around the ideal expansion and breaks it into two regimes that represent over and under expansion. Values greater than unity are under-expanded and values less than are over-expanded.

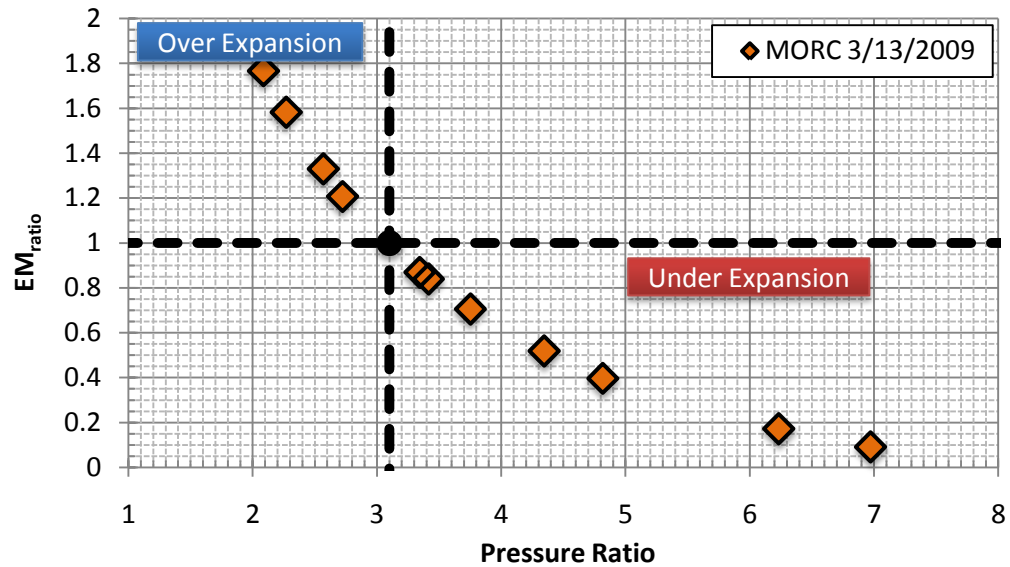


Fig. 53: Showing the relationship between EM_{ratio} and pressure ratio. The ideal expansion for the case data is represented by the dot on the dashed line.

The EM_{ratio} does have an inherent problem when used with our data. There is a level of uncertainty in the measurement of the inlet and exit volume of the expander which have been calculated to be 0.45 and 1.03 [in³] respectively. From these values the expansion ratio is 2.29 which does not match the value estimated by Wang et al. [48] of approximately 2.5. This estimated value also contains some uncertainty. An alternative method to calculate the expansion ratio is by using the exit volume, an EM_{ratio} of less than unity, and the ideal operating point from the 3/31/2010 data set. The exit volume is considered accurate because it is easy to identify in the model of the scroll assembly. An EM_{ratio} of less than unity is chosen because Fig. 51 would suggest that there is a peak in performance between the pressure ratios 2.72 and 3.34. With EES and the properties of the selected point an EM_{ratio} of 0.87 was selected.

This results in an inlet volume of 0.3653 [in³] and expansion ratio of 2.828 which is close to the estimated values of 2.5 and 2.29. The inlet volume appears to be low but it is possible that the exit volume could occur earlier in the expansion process. With these values the EM_{ratio} of different data sets were calculated.

The efficiency as a function of EM_{ratio} is shown in Fig. 54. It should be noted that the expander exit temperature for the HAC system is not necessarily representative of the

expanders exit temperature. The measured value is higher than the actual which causes the data to shift to the left. The HAC 3/31/2010 data should be closer to unity. Results from Mathias et al. [42] are also plotted for comparison. We can see that values closest to unity achieve the highest efficiency. An obvious advantage of the scroll expander over the gerotor is that it is less sensitive to a non-ideal EM_{ratio} . More data needs to be collected to determine the pressure ratio that will yield the highest efficiency and confirm the assumptions made in the calculation of inlet expander volume.

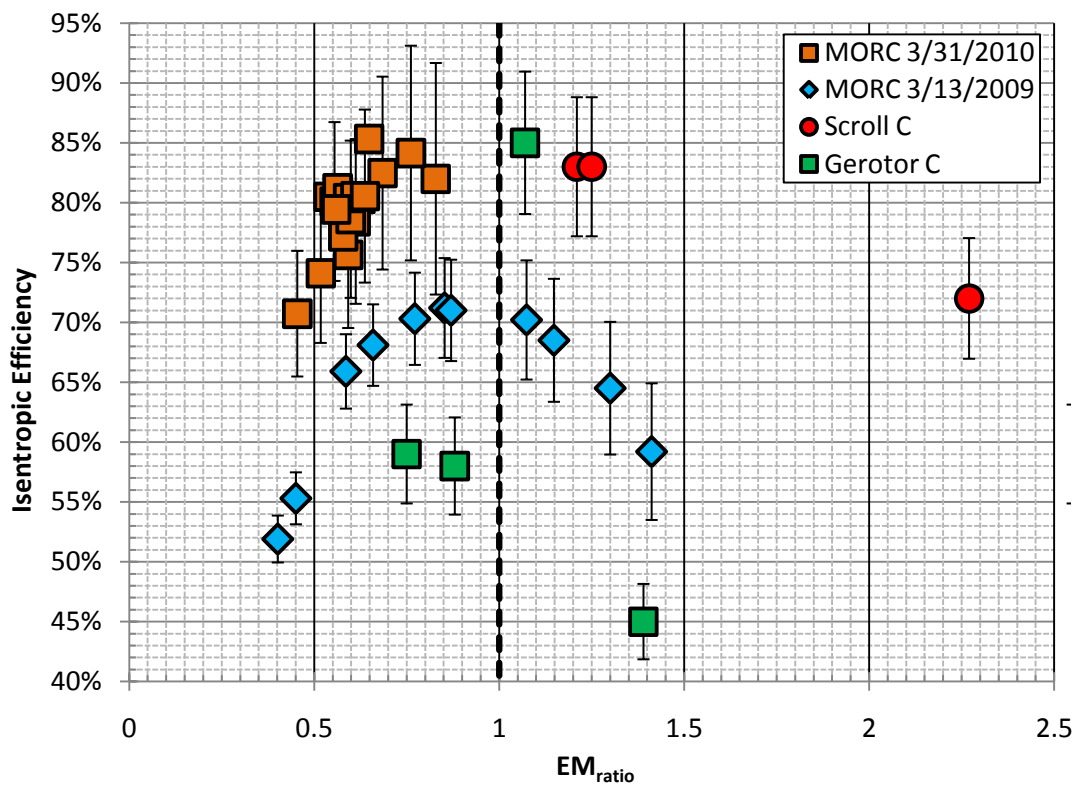


Fig. 54: Isentropic efficiency as a function of EM_{ratio} . The Gerotor and Scroll C data is taken from Mathias et al. [42].

The data set with the highest efficiency was not plotted because it was taken at similar operating conditions over the entire data set. The highest recorded efficiency was calculated to be 87.2% which was taken from the HAC 4/19/2010 data set at a pressure ratio of 3.98. Its maximum power out was 1 [kW]. The 3rd generation scroll expander is expected to achieve higher efficiencies with increased runtime and a more optimal pressure ratio.

7 CONCLUSION

A scroll expander has been successfully fabricated and demonstrated with both R134a and R245fa as working fluids with varying rotational speeds, expansion ratios, and achieved isentropic efficiencies over 70%. This expander was modified from a compliant scroll compressor. It was self-starting and had external control over the seal piston pressure. Spherical miter gears placed the power takeoff on the side of the expander which allowed the lubrication system design by the manufacturer to function properly. The gears had the unforeseen effect of acting as an oil mister which improved the lubrication of the scroll assembly. The expander achieved a maximum isentropic efficiency of 87.2% while producing a maximum power output of 1 [kW] and was dynamically balanced to minimize vibration. The performance characteristics such as speed, torque, and power were measured using two separate dynamometers. It was also shown that a scroll expander has good off design performance and has an optimal pressure ratio of approximately 3.3. It was also shown that its performance is a weak function of speed. It is important to note the significant impact that a larger diameter shaft and shaft seal can have on performance. Break-in is another important consideration with performance.

This thesis has shown the value of the EM_{ratio} can be a useful quantity when evaluating expander performance but further data needs to be collected to fill gaps in the current data set to establish an accurate inlet volume. Additional testing should also be performed because the expander has shown that it is still in break-in and is expected to yield increased performance with increased runtime.

8 FUTURE WORK

As mentioned earlier, Lemort et al. [45] created a computational model of the different losses that degrade the performance of a scroll expander. Besides non-ideal expansion the losses in order of magnitude are leakage, mechanical friction, pressure drops, and internal heat transfer. In this order these are the areas where a potential follow-on work could improve the efficiency of the expander.

The first recommendation would be to run the expander until it is sufficiently broken in and the efficiency is no longer a function of run time. Another recommendation includes minimizing the sealing surface diameter of the power takeoff shaft as it was shown to have a significant effect on performance. Adding a PTFE tip seal on the fixed and orbiting scroll could reduce leakage and mechanical friction. A PTFE seal could also be added to the sealing piston. A computational fluid model could be developed for the inlet and outlet ports of the expander to optimize their geometry to minimize pressure drop. Insulation could be added to the exterior of the scroll assembly to reduce internal heat transfer.

Measurement improvements include improving the exit temperature which could be accomplished by placing a thermocouple directly in the scroll assembly exit port. It would also be useful to better quantify over and under-expansion by measuring the pressure at the scroll assembly exit port.

Another suggestion would be to perform a more comprehensive test to confirm that the isentropic efficiency is a weak function of speed. More testing should also be done to confirm the effect of pressure ratio on efficiency. It would be useful to have a detailed trend with the new shaft and shaft seal which caused a significant increase in performance.

Beyond performance the bottom cover could be modified to reduce weight. Also it was aforementioned that the 6061-T6 vertical bearing holder should be changed to AISI4140. It was noticed that the scroll assembly is causing wear on the fixed scroll. A more rigid method of fixing the scroll assembly to the housing should be considered.

9 BIBLIOGRAPHY

- [1] S. Carnot and W. Thompson, *Reflection On The Motive Power Of Heat. Accompanied By An Account of Carnot's Theory*. New York: Wiley & Sons, 1897.
- [2] *Annual Energy Review 2008*. Washington, DC: U.S. Energy Information Administration, 2009, p. 407.
- [3] M. Ehsani, *Modern electric, hybrid electric, and fuel cell vehicles : fundamentals, theory, and design*, 2nd ed. Boca Raton: CRC Press, 2010.
- [4] M. Moran, *Fundamentals of engineering thermodynamics*, 5th ed. [Hoboken NJ?]: Wiley, 2004.
- [5] *Annual Energy Outlook 2010*. Washington, DC: U.S. Energy Information Administration, 2010, p. 221.
- [6] R. B. Peterson, H. Wang, and T. Herron, "Performance of a small-scale regenerative Rankine power cycle employing a scroll expander," *Proceedings of the Institution of Mechanical Engineers, Part A: Journal of Power and Energy*, vol. 222, no. 3, pp. 271-282, 2008.
- [7] A. Fraas, *Engineering evaluation of energy systems*. New York: McGraw-Hill, 1982.
- [8] B. Saleh, G. Koglbauer, M. Wendland, and J. Fischer, "Working fluids for low-temperature organic Rankine cycles," *Energy*, vol. 32, no. 7, pp. 1210-1221, 2007.
- [9] A. Schuster, S. Karellas, and R. Aumann, "Efficiency optimization potential in supercritical Organic Rankine Cycles," *Energy*, vol. 35, no. 2, pp. 1033-1039, 2010.
- [10] A. Schuster, S. Karellas, E. Kakaras, and H. Spliethoff, "Energetic and economic investigation of Organic Rankine Cycle applications," *Applied Thermal Engineering*, vol. 29, no. 8, pp. 1809-1817, 2009.
- [11] T. Hung, "A review of organic rankine cycles (ORCs) for the recovery of low-grade waste heat," *Energy*, vol. 22, no. 7, pp. 661-667, 1997.
- [12] S. A. Klein, *Engineering Equation Solver (EES)*. fchart.com: F-Chart Software, 2009.

- [13] T. Hung, "Waste heat recovery of organic Rankine cycle using dry fluids," *Energy Conversion and Management*, vol. 42, no. 5, pp. 539-553, 2001.
- [14] C. Ennis, *Scientific assessment of ozone depletion 2006 : pursuant to article 6 of Montreal protocol on substances that deplete the ozon layer*. Ženeva: WMO, 2007.
- [15] P. Mago, L. Chamra, K. Srinivasan, and C. Somayaji, "An examination of regenerative organic Rankine cycles using dry fluids," *Applied Thermal Engineering*, vol. 28, no. 8, pp. 998-1007, 2008.
- [16] P. J. Mago, L. M. Chamra, and C. Somayaji, "Performance analysis of different working fluids for use in organic Rankine cycles," *Proceedings of the Institution of Mechanical Engineers, Part A: Journal of Power and Energy*, vol. 221, no. 3, pp. 255-263, 2007.
- [17] A. Borsukiewiczgozdur and W. Nowak, "Comparative analysis of natural and synthetic refrigerants in application to low temperature Clausius–Rankine cycle," *Energy*, vol. 32, no. 4, pp. 344-352, 2007.
- [18] J. Larjola, "Electricity from industrial waste heat using high-speed organic Rankine cycle (ORC)," *International Journal of Production Economics*, vol. 41, no. 1, pp. 227-235, 1995.
- [19] O. Badr, P. Ocallaghan, and S. Probert, "Performances of Rankine-cycle engines as functions of their expanders' efficiencies," *Applied Energy*, vol. 18, no. 1, pp. 15-27, 1984.
- [20] D. Manolakos, G. Kosmadakis, S. Kyritsis, and G. Papadakis, "Identification of behaviour and evaluation of performance of small scale, low-temperature Organic Rankine Cycle system coupled with a RO desalination unit," *Energy*, vol. 34, no. 6, pp. 767-774, 2009.
- [21] D. Manolakos, G. Papadakis, S. Kyritsis, and K. Bouzianas, "Experimental evaluation of an autonomous low-temperature solar Rankine cycle system for reverse osmosis desalination," *Desalination*, vol. 203, no. 1, pp. 366-374, 2007.
- [22] X. Wang, L. Zhao, J. Wang, W. Zhang, X. Zhao, and W. Wu, "Performance evaluation of a low-temperature solar Rankine cycle system utilizing R245fa," *Solar Energy*, vol. 84, no. 3, pp. 353-364, 2010.
- [23] T. Saitoh, N. Yamada, and S. Wakashima, "Solar Rankine Cycle System Using Scroll Expander," *Journal of Environment and Engineering*, vol. 2, no. 4, pp. 708-719, 2007.

- [24] P. Bombarda, C. M. Invernizzi, and C. Pietra, "Heat recovery from Diesel engines: A thermodynamic comparison between Kalina and ORC cycles," *Applied Thermal Engineering*, vol. 30, no. 2, pp. 212-219, 2010.
- [25] H. D. Madhawa Hettiarachchi, M. Golubovic, W. M. Worek, and Y. Ikegami, "The Performance of the Kalina Cycle System 11(KCS-11) With Low-Temperature Heat Sources," *Journal of Energy Resources Technology*, vol. 129, no. 3, p. 243, 2007.
- [26] Y. Chen, P. Lundqvist, A. Johansson, and P. Platell, "A comparative study of the carbon dioxide transcritical power cycle compared with an organic rankine cycle with R123 as working fluid in waste heat recovery," *Applied Thermal Engineering*, vol. 26, no. 17, pp. 2142-2147, 2006.
- [27] J. Baek, E. Groll, and P. Lawless, "Piston-cylinder work producing expansion device in a transcritical carbon dioxide cycle. Part I: experimental investigation," *International Journal of Refrigeration*, vol. 28, no. 2, pp. 141-151, 2005.
- [28] R. Stirling, "Stirling air engine and the heat regenerator," U.S. Patent 4081.
- [29] D. Thombare and S. Verma, "Technological development in the Stirling cycle engines," *Renewable and Sustainable Energy Reviews*, vol. 12, no. 1, pp. 1-38, 2008.
- [30] P. Pichanusakorn and P. Bandaru, "Nanostructured thermoelectrics," *Materials Science and Engineering: R: Reports*, vol. 67, no. 2, pp. 19-63, 2010.
- [31] E. W. Miller, T. J. Hendricks, and R. B. Peterson, "Modeling Energy Recovery Using Thermoelectric Conversion Integrated with an Organic Rankine Bottoming Cycle," *Journal of Electronic Materials*, vol. 38, no. 7, pp. 1206-1213, 2009.
- [32] C. McDonald and C. Rodgers, "Small recuperated ceramic microturbine demonstrator concept," *Applied Thermal Engineering*, vol. 28, no. 1, pp. 60-74, 2008.
- [33] T. Yamamoto, "Design and testing of the Organic Rankine Cycle," *Energy*, vol. 26, no. 3, pp. 239-251, 2001.
- [34] W. Yagoub, P. Doherty, and S. Riffat, "Solar energy-gas driven micro-CHP system for an office building," *Applied Thermal Engineering*, vol. 26, no. 14, pp. 1604-1610, 2006.

- [35] J. Baek, E. Groll, and P. Lawless, "Piston-cylinder work producing expansion device in a transcritical carbon dioxide cycle. Part I: experimental investigation," *International Journal of Refrigeration*, vol. 28, no. 2, pp. 141-151, 2005.
- [36] B. Zhang, X. Peng, Z. He, Z. Xing, and P. Shu, "Development of a double acting free piston expander for power recovery in transcritical CO₂ cycle," *Applied Thermal Engineering*, vol. 27, no. 8, pp. 1629-1636, 2007.
- [37] O. Badr, "Multi-vane expanders as prime movers for low-grade energy organic Rankine-cycle engines," *Applied Energy*, vol. 16, no. 2, pp. 129-146, 1984.
- [38] M. Mohd.Tahir, N. Yamada, and T. Hoshino, "Efficiency of Compact Organic Rankine Cycle System with Rotary-Vane-Type Expander for Low-Temperature Waste Heat Recovery," *International Journal of Environmental Science And Engineering*, vol. 2, no. 1, pp. 11-16, 2010.
- [39] B. Yang, X. Peng, Z. He, B. Guo, and Z. Xing, "Experimental investigation on the internal working process of a CO₂ rotary vane expander," *Applied Thermal Engineering*, vol. 29, no. 11, pp. 2289-2296, 2009.
- [40] G. Haiqing, M. Yitai, and L. Minxia, "Some design features of CO swing piston expander," *Applied Thermal Engineering*, vol. 26, no. 2, pp. 237-243, 2006.
- [41] A. Subiantoro and K. Ooi, "Design analysis of the novel Revolving Vane expander in a transcritical carbon dioxide refrigeration system," *International Journal of Refrigeration*, vol. 33, no. 4, pp. 675-685, 2010.
- [42] J. A. Mathias, J. R. Johnston, J. Cao, D. K. Priedeman, and R. N. Christensen, "Experimental Testing of Gerotor and Scroll Expanders Used in, and Energetic and Exergetic Modeling of, an Organic Rankine Cycle," *Journal of Energy Resources Technology*, vol. 131, no. 1, p. 012201, 2009.
- [43] H. J. Kim, J. M. Ahn, I. Park, and P. C. Rha, "Scroll expander for power generation from a low-grade steam source," *Proceedings of the Institution of Mechanical Engineers, Part A: Journal of Power and Energy*, vol. 221, no. 5, pp. 705-711, 2007.
- [44] G. Xiaojun, L. Liansheng, Z. Yuanyang, and S. Pengcheng, "Research on a Scroll Expander Used for Recovering Work in a Fuel Cell," *International Journal Of Thermodynamics*, vol. 7, no. 1, pp. 1-8, Mar. 2004.
- [45] V. Lemort, S. Quoilin, C. Cuevas, and J. Lebrun, "Testing and modeling a scroll expander integrated into an Organic Rankine Cycle," *Applied Thermal Engineering*, vol. 29, no. 14, pp. 3094-3102, 2009.

- [46] T. Saitoh, N. Yamada, and S. Wakashima, "Solar Rankine Cycle System Using Scroll Expander," *Journal of Environment and Engineering*, vol. 2, no. 4, pp. 708-719, 2007.
- [47] D. Manolakos, G. Kosmadakis, S. Kyritsis, and G. Pa, "Identification of behaviour and evaluation of performance of small scale, low-temperature Organic Rankine Cycle system coupled with a RO desalination unit," *Energy*, vol. 34, no. 6, pp. 767-774, Jun. 2009.
- [48] H. Wang, R. B. Peterson, and T. Herron, "Experimental performance of a compliant scroll expander for an organic Rankine cycle," *Proceedings of the Institution of Mechanical Engineers, Part A: Journal of Power and Energy*, vol. 223, no. 7, pp. 863-872, 2009.
- [49] L. Guangbin, Z. Yuanyang, L. Liansheng, and S. Pengcheng, "Simulation and experiment research on wide ranging working process of scroll expander driven by compressed air," *Applied Thermal Engineering*, vol. 30, no. 14, pp. 2073-2079, 2010.
- [50] A. Ambekar, *Mechanism and machine theory*. New Delhi: Prentice-Hall of India, 2007.
- [51] Richard G. Budynas and J. Keith Nisbett, *Shigley's Mechanical Engineering Design*, 8th ed. McGraw-Hill Science/Engineering/Math, 2006.
- [52] B. Dengel, "Miter Gears," 16-Jul-2008.
- [53] F. Yeaple, *Fluid power design handbook*, 3rd ed. New York: M. Dekker, 1996.
- [54] P. Schweitzer, *Metallic materials : physical, mechanical, and corrosion properties*. New York: M. Dekker, 2003.
- [55] Ralph Cuppoletti, "Re: OSU Scroll Balance," 25-Aug-2010.
- [56] A. Wheeler, *Introduction to engineering experimentation*, 2nd ed. Upper Saddle River NJ: Prentice Hall, 2003.
- [57] D. Manolakos, G. Papadakis, S. Kyritsis, and K. Bouzianas, "Experimental evaluation of an autonomous low-temperature solar Rankine cycle system for reverse osmosis desalination," *Desalination*, vol. 203, no. 1, pp. 366-374, 2007.
- [58] J. Kaufman, *Properties of aluminum alloys : tensile, creep, and fatigue data at high and low temperatures*. Materials Park Ohio ;Washington D.C.: ASM International ;Aluminum Association, 1999.

10 APPENDICIES

Appendix A: Engineering Calculations

A.1 Counterweight Calculations

As was aforementioned counterweight sizes only require taking the sum of the moments about points A and B shown in Fig. 55. The force these masses cause is the centrifugal force, which is expressed as

$$F_c = m\omega^2 r \quad (14)$$

where m is the mass of the rotating mass, ω is the angular velocity, and r is the distance of rotating mass to the center of rotation. All masses will have the same angular velocity and it therefore drops out of the analysis.

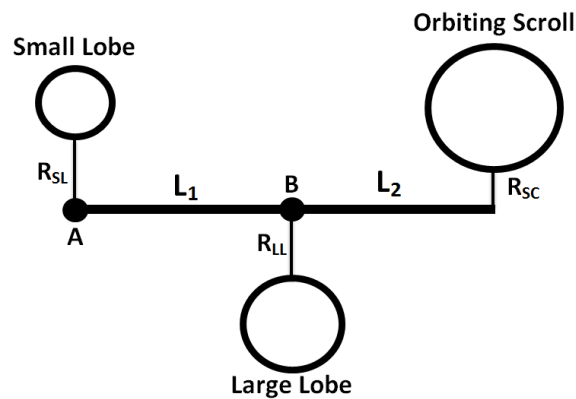


Fig. 55: Free body diagram of the position of the different components in the balancing calculation.

First we take the sum of the moments about B where the direction out of the paper is positive is

$$\Sigma M_B = m_{SC} R_{SC} L_2 - m_{SL} R_{SL} L_1 = 0 \quad (15)$$

and taking the moments about A in the same direction is

$$\Sigma M_A = m_{SC} R_{SC} (L_1 + L_2) - m_{LL} R_{LL} L_1 = 0 \quad (16)$$

By fixing certain parameters Eqns. (15) and (16) can be solved. When fixing parameters it is desirable to maximize L_1 , R_{SL} , and R_{LL} and minimize L_2 . This will minimize the mass of the

counterweights. Many values were not well optimized due to the constraints of the housing. A summary of the different parameters as well as the final weight of the counterweights are given in Table 13.

Table 13: Summary of fixed and calculated parameters for the design of the counterweights.

Mass [g]		Lengths [mm]	
Calculated	Oversized (10%)	R _{SL}	25.4
350.9	385.6	R _{LL}	25.4
262.3	288.5	R _{SC}	3.321
		L ₁	75.22
		L ₂	25.4

A.2 Reaction Force Calculations

With a spherical miter gear selected the reaction forces could be calculated. The design torque of 3 [N-m] was used to calculate the reaction forces on the gear teeth. The tangential, axial, and radial forces are given by

$$\begin{aligned}
 W_t &= \frac{T}{r_p} = \frac{3[\text{N-m}]}{0.025[\text{m}]} = 120[\text{N}] \\
 W_r &= W_t \tan(\phi) \cos(\gamma) = 120[\text{N}] \tan(20^\circ) \cos(49.38^\circ) = 28.44[\text{N}] \\
 W_a &= W_t \tan(\phi) \sin(\gamma) = 120[\text{N}] \tan(20^\circ) \sin(49.38^\circ) = 33.15[\text{N}]
 \end{aligned} \tag{17}$$

where T is torque, r_p is the pitch radius, ϕ is the pressure angle, and γ is the tip angle. The positions of the bearings were selected to minimize loading while keeping the foot print to a reasonable size. For reference the reaction forces and lengths are listed in Fig. 56. The shaft and power takeoff shaft both have five unknowns and will both require five equations to solve. We write out the sum of the forces in the ijk directions for the main shaft as

$$\begin{aligned}
 \Sigma F_i &= B1_i + B2_i - W_r = 0 \\
 \Sigma F_j &= B1_j + B2_j - W_t = 0 \\
 \Sigma F_k &= B2_k + W_a - F_g = 0
 \end{aligned} \tag{18}$$

and the power takeoff shaft as

$$\begin{aligned}\Sigma F_i &= B3_i + W_r = 0 \\ \Sigma F_j &= B3_j + B4_j + W_t = 0 \\ \Sigma F_k &= B3_k + B4_k - W_a = 0.\end{aligned}\tag{19}$$

Next we write out equations for the sum of the moments in the ij directions about B1 for the main shaft

$$\begin{aligned}\Sigma M_{B1i} &= B2_j L_A - W_t(L_A + L_B) = 0 \\ \Sigma M_{B1j} &= -B2_i L_A + W_r(L_A + L_B) - W_a L_C = 0\end{aligned}\tag{20}$$

and about B4 in the jk directions for the power takeoff shaft as

$$\begin{aligned}\Sigma M_{B4j} &= B3_k L_F - W_a(L_F + L_E) + W_r L_D = 0 \\ \Sigma M_{B4k} &= -B3_j L_F - W_t(L_F + L_E) = 0\end{aligned}\tag{21}$$

where F_g is the force caused by the weight of the counterweights, bearing, gear, and main shaft. It was calculated to be 12.98 [N]. Eqn. (18)-(21) were solved simultaneously with EES. A list of the calculated forces is summarized in Table 14. With these forces known bearings can be selected.

Table 14: Summary of bearing reaction forces shown in Fig. 56. All forces are in [N].

	Location	i	j	k
Shaft	B1	1.671	-45.76	0
	B2	26.77	165.8	-11.43
Power Takeoff	B3	-28.44	-246	44.58
	B4	0	126	-11.43

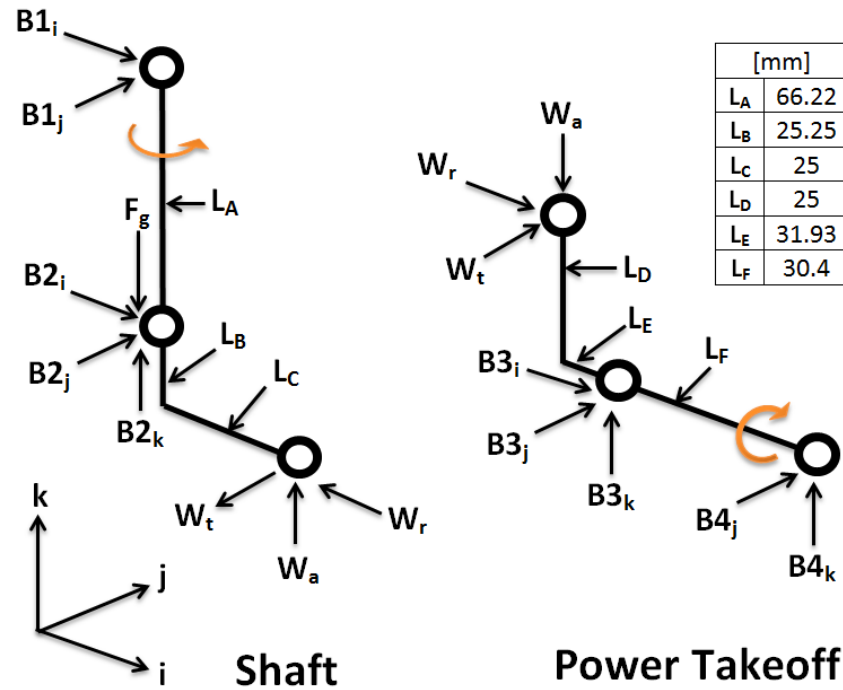


Fig. 56: Free body diagram of reaction forces on the shaft and power takeoff.

A.3 Bearing Life

To confirm that the selected bearings would not fail over the course of testing the bearing life was calculated. The dynamic loading of the 6201-RSL bearing is rated at $C_{10}=7.28$ [kN] and its static loading is rated at 2.3 [kN]. The magnitude of the radial loads is $F_r=248$ [N], and the axial load is $F_a=44.5$ [N]. The shaft will rotate at 3,600 [RPM]. The inner race turns which makes the parameter $V=1$. The load ratio is calculated to be

$$F_a / C_o = 44.5 / 2,300 = 0.0139 \quad (22)$$

and from this value the parameter e was taken to be 0.19 from Table 11-1 [51]. This parameter is then compared to the following ratio

$$F_a / (VF_r) = 44.5 / (1 \cdot 248) = 0.1797 \quad (23)$$

and because it is less than e we use the values $X_1=1$ and $Y_1=0$ to calculate our effective load. In this case the effective load is $F_e=VF_r$. The life of a bearing in hours can be described by

$$C_{10}(L_R n_R (60))^{1/a} = F_e (L_D n_D 60)^{1/a} \quad (24)$$

where L_R is the rated life in hours, n_R is the rated speed in [RPM], L_D is the desired life in hours, n_D is the rated speed in [RPM], and $a=3$ for ball bearings. The quantity $L_R n_R 60$ represents the rated number of revolutions, which for a SKF bearing is 10^6 [51]. Rearranging the equation and solving gives

$$L_D = \frac{L_R n_R (60)}{n_D 60} \left(\frac{C_{10}}{F_e} \right)^a = \frac{10^6}{3,600 \cdot 60} \left(\frac{7,280}{258} \right)^3 = 1.18 \times 10^6 \text{ Hours} . \quad (25)$$

This shows that both 6201-RSL bearings will not fail during testing. The rated dynamic and static loads of the W6205 are 11.9 and 7.65 [kN] respectively. These values are larger than the other bearing and therefore this bearing is expected to have a life longer than the period of testing.

A.4 Minimum Thread Engagement

The first check is to see if the threaded length is sufficient to ensure that under failure the screw will fail and not the thread. The minimum thread engagement is determined by

$$L_e = \frac{2A_t}{0.5 \cdot \pi (D - 0.64952 \cdot p)} \quad (26)$$

where A_t is the tensile stress area, D is the major diameter, and p is the thread pitch. For a ¼-20 fastener $D=0.25$ [in], $A_t=0.0318$ [in²], and $p = 1/20$. This results in a minimum thread engagement of 0.1826 [in]. All threaded holes are kept at least at this depth.

A.5 Top Cover Bolts

The top cover is exposed to a 66 [psi] and 386 [psi] gauge pressure. Additionally the scroll pressure plate exerts a 200 [psi] pressure on the top cover. It is held down by a circle of screws that fasten into the top flange of the housing. It is desirable to see if a total of 8 screws are adequate to hold down the top cover. The areas exposed to various pressures are summarized in Table 15.

Table 15: Summary of pressure force information for top cover.

Gauge Pressure [psi]	Area [in ²]	Resulting Force [lbf]
386	0.62	239
66	20.6	984
200	3.88	776

The total force exerted is 1,999 [lbf], which results to 250 [lbf] per screw. A more critical analysis was performed on these screws because it was subjected to the largest load. Table 16 gives a summary of the important quantities from the analysis.

Table 16: Summary of important quantities in calculating bolt load factor.

Bolt Minimum Tensile Strength	70 [kpsi]
Bolt Estimated Yield Strength	30 [kpsi]
Tensile Area of Bolt	0.0318 [in ²]
Member Spring Stiffness	36.32 [Mlbf/in ²]
Bolt Spring Stiffness	2.34 [Mlbf/in ²]
Preload for reused bolts	715 [lbf]
Joint Constant	0.061

These above values are used to calculate different safety factors of bolts which are summarized for different cases in Table 17. The load factor is the quantity that prevents the stress in the bolt from becoming larger than the yield strength. The joint load factor prevents the joints from separating and causing the entire bolt from carrying the load. The bolt factor of safety represents a case when the joints separate, and the bolt takes the entire load.

Table 17: Summary of factors of safety for the top cover under varying scenarios.

Load Factor (8 Bolts based on Yield Strength)	15.7
Joint Load Factor (8 Bolts based on Yield Strength)	3
Factor of Safety (8 Bolts based on Yield Strength)	0.95
Factor of Safety (8 Bolts based on Yield Strength with ½ Preload)	2.38

The above shows that the bolt should not experience the full load with the appropriate preload of 715 [lbf], which is equivalent to about 66.4 in-lb of torque. In the case when insufficient preload is applied and the bolts take the entire load the factor of safety increases to 2.38. It should also be noted that the ultimate strength of AISI304 is over twice as large as the yield strength.

A.6 Bottom Cover Bolts

The bottom cover is only subjected to a 66 [psi] differential, and has an area of 21.6 [in²] which results in 1,426 [lbf] of force. Using the yield strength in Table 16 and 6 bolts results in a factor of safety of 2.5 with a preload of 358 [lbf].

A.7 Vertical Bearing Holder Bolts

With the FEA model created with Solidworks Simulation the screw reaction forces were calculated. They are summarized in Table 18.

Table 18: Summary of bolt reaction results from Solidworks Simulation for the vertical bearing holder.

Connector	Axial Force [lb]	Shear Force [lb]
1	589	8.9
2	592	11.8
3	589	9.5
4	592	10.6

Using 0.0318 [in²] as the tensile stress area we calculate the maximum normal stress to be 18,616 [psi] which results in a factor of safety of 3.76. The shear stress developed in the bolted connection is given as

$$\tau = \frac{F}{A_r} = 0.577 \frac{S_p}{n} \quad (27)$$

where S_p is the minimum strength of the bolt and A_r is the minor diameter. Solving this equation with $A_r = 0.0269 \text{ [in}^2\text{]}$ and taking $S_p = 70,000 \text{ [psi]}$ we get a factor of safety of 92.

A.8 Horizontal Bearing Holder Bolts

With the FEA model created with Solidworks Simulation the screw reaction forces were calculated. They are summarized in Table 19.

Table 19: Summary of bolt reaction results from Solidworks Simulation for the horizontal bearing holder.

Connector	Axial Force [lb]	Shear Force [lb]
Top Right	590	10.7
Top Left	590	2.6
Bottom Right	590	12
Bottom Left	590	5.4

Comparing the loads between Table 18 and Table 19 we can see that the ¼-20 AISI304 bolts should be sufficient to support the horizontal bearing holder.

A.9 Set Screw

The ability of a set screw to resist motion between the hub and shaft is called holding power [51]. A steel knurled cup ¼-20 set screw was used with a 3A class coarse thread was used. The nominal seating torque for this type of set screw is 87 [lbf-in] [51] which is equivalent to 9.83 [N-m]. This results in a static factor of safety of three with our design torque. It is recommended that set screws have an engagement length that is at least half of the shaft diameter [51]. The shaft diameter of the power takeoff is 12 [mm] and the thread engagement length is a little over 12.7 [mm].

A.10 Dowel Pins

Steel dowel pins with a double shear strength of 3200 [lbf] were selected. With our design torque of 3 [N-m] and at a radius of 0.5 [in] this results in a force of 256 [N] or 53.1 [lbf]. This results in a factor of safety of 60.2.

A.11 Design Stage Uncertainty

It is important to establish the accuracy of your equipment which is why a design stage uncertainty is performed. In our tests operating points are measured and averaged which is why our uncertainty is dominated by bias errors.

The bias errors of the equipment used to measure the expander performance are summarized in Table 20 and Table 21.

Table 20: Detailed uncertainty summary of torque sensor in the HAC test bed. The rated output (R.O.) is 5VDC. Temperature effects are not included because we are operating within the compensated range of the device.

Specification	Accuracy	Uncertainty
Zero Balance	±1% (R.O.)	0.05 [VDC]
Nonlinearity	±0.2% (R.O.)	0.01 [VDC]
Hysteresis	±0.1% (R.O.)	0.005 [VDC]
Non Repeatability	±0.2% (R.O.)	0.01 [VDC]
RMS Uncertainty		0.0522 [VDC]

Taking the uncertainty of the signal processing into account and scaling the RMS uncertainty of the torque sensor we end with an overall uncertainty of ±0.105 N-m for the HAC test bed torque sensor.

Table 21: Summary of equipment bias uncertainty.

Measurement	Equipment	Accuracy	Uncertainty	Test Bed
Temperature	Type K SLE	1.1°C or 0.4%	±1.1[°C]	HAC /ORC
Pressure Inlet	PX315-500GI	0.05% (FS)	±1.38 [kPa]	HAC /ORC
Pressure Outlet	PX315-200GI	0.05% (FS)	±0.34 [kPa]	HAC /ORC
Torque	HD-715-8N-4831	0.25-0.5% (FS)	±0.031 [N-m]	ORC
Torque	Futek TRS-605	1.05% (FS)	±0.105 [N-m]	HAC
Torque Signal	-	±0.1%	±0.1 [VDC]	HAC
Mass flow rate	TRG-11.300-5	±1% (Reading)	-	HAC
Mass flow rate	Orifice Plate	±0.6% (FS)	±2.7e-4 [kg/s]	ORC
Power	HD-715-8N-4831	0.25-0.5% (FS)	15 [W]	ORC
Power	Futek TRS-605	-	-	HAC

The sum of the different bias errors can be combined using the perturbation of errors method. First we start with basic expander isentropic efficiency which is described by

$$\eta_{Exp} = \frac{\dot{W}_m}{\dot{m}(h_3 - h_{4s})} \quad (28)$$

In order to calculate the overall uncertainty in the efficiency the uncertainty in enthalpy and work has to be first derived. The overall uncertainty in the enthalpy is given by

$$h_{error} = \sqrt{\left(h(T + T_p, P) - h(T, P)\right)^2 - \left(h(T, P + P_p) - h(T, P)\right)^2} \quad (29)$$

where the nominal values used are summarized in Table 22.

Table 22: Summary of nominal and perturbed values used in the enthalpy uncertainty calculation.

Parameter	ORC Uncertainty		HAC Uncertainty	
	Nominal	Perturbed	Nominal	Perturbed
T _i	125 [°C]	±1.1[°C]	165 [°C]	±1.1[°C]
P _i	400 [psi]	±1.38 [kPa]	400 [psi]	±1.38 [kPa]

The overall uncertainty in enthalpy for the ORC and HAC test beds was calculated to be ±1.375 and ±1.603 [kJ/kg] respectively.

The uncertainty in the power measurement for the ORC test bed is given but in the HAC it is calculated from the torque and speed measurements. This requires an additional uncertainty calculation given by the following

$$\dot{W}_{error} = \sqrt{\left(\left(T_q + T_{qp}\right) \cdot \omega - T_q \omega\right)^2 + \left(T_q \cdot \left(\omega + \omega_p\right) - T_q \omega\right)^2} \quad (30)$$

where T_q is torque and ω is speed. The nominal values for torque and speed are 3 [N-m] and 3,600 [RPM]. Using the bias errors given in Table 21 the uncertainty in work is calculated to be ± 40 [W].

Applying the method of perturbation we can express the total error in the isentropic efficiency as

$$\eta_{error} = \sqrt{\left(\frac{\dot{W}_m + \dot{W}_p}{\dot{m}(h_3 - h_{4s})} - \eta_{Exp}\right)^2 + \left(\frac{\dot{W}_m}{(\dot{m} + \dot{m}_p)(h_3 - h_{4s})} - \eta_{Exp}\right)^2 + \left(\frac{\dot{W}_m}{\dot{m}(h_3 + h_{3p} - h_{4s})} - \eta_{Exp}\right)^2 + \left(\frac{\dot{W}_m}{\dot{m}(h_3 - (h_{4s} + h_{4sp}))} - \eta_{Exp}\right)^2} \quad (31)$$

where the subscript p represents the perturbed value. The perturbed, nominal, and overall uncertainty are summarized in Table 23.

Table 23: Summary of perturbed, nominal, and overall uncertainty for ORC and HAC test beds.

ORC Uncertainty			HAC Uncertainty	
Parameter	Nominal	Perturbed	Nominal	Perturbed
\dot{W} [kW]	0.9	0.015	1	0.040
\dot{m} [kg/s]	0.035	$\pm 3.5e-4$	0.033	$\pm 2.7e-4$
h_1 [kJ/kg]	342.8	± 1.375	534.3	± 1.603
h_{2s} [kJ/kg]	301.6	± 1.375	500.3	± 1.603

The resulting design stage uncertainties in isentropic efficiency for the ORC and HAC test beds are 3.19% and 6.98% respectively.

Appendix B: Finite Element Analysis

B.1 Vertical Bearing Holder

Soldiworks Simulation was used to perform a static FEA analysis on the vertical bearing holder attached to the bottom cover. It was refined in several locations of interest such as the bolt locations.

In the model a no penetration global contact was defined. Four screw connections were defined with ½-20 sockets. The sockets had a head diameter of 0.37 [in] and were pre-torqued to 7.5 [N-m] with a coefficient of friction of 0.2. It was subjected to the loads specified for B2 in Appendix A.1. The specifications of the mesh used are defined in Table 24.

The yield and tensile strength of 6061-T6 were modified to reflect their decreased strength at 150°C which are 200 and 185 [Mpa] respectively [58]. These properties represent 6061-T6 that has been at the specified temperature for 10,000 hours.

The results of the FEA analysis are shown in Fig. 57. The plots show that the vertical bearing holder made with 6061-T6 at 150°C will hold its structural integrity. The minimum factor of safety based on the yield strength is 1.55. Under the screw head is close to yielding.

Table 24: Summary of mesh and solver information from Solidworks Simulation for the vertical bearing holder.

Mesher	
Mesh type	Solid Mesh
Mesher Used	Standard mesh
Jacobian points	4 points
Element size	9.71289 mm
Tolerance	0.0794691 mm
Mesh quality	High
Total nodes	410480
Total elements	271989
Maximum Aspect Ratio	159.29
with Aspect Ratio < 3	98.5
with Aspect Ratio > 10 (Jacobian)	0.00221 0.9
Solver	
No. of DOF	1247922
Total solution time	05:12:37

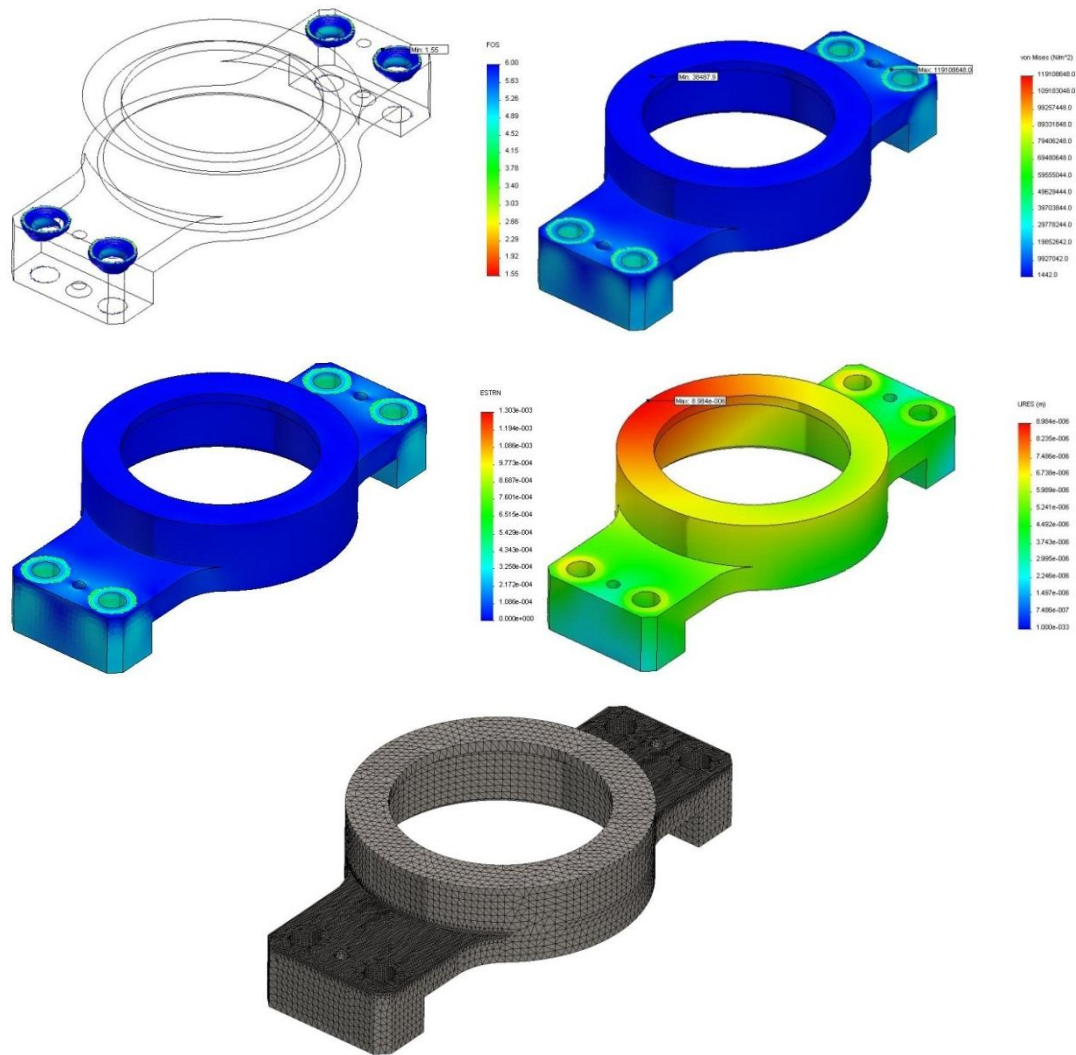


Fig. 57: From left to right and top to bottom. Factor of safety plot based on a yield strength of 185 [Mpa] with ISO clipping, stress plot, strain plot, displacement plot, and mesh.

B.2 Horizontal Bearing Holder

Soldiworks Simulation was used to perform a static FEA analysis on the horizontal bearing holder attached to the bottom cover.

In the model a no penetration global contact was defined. The four screw connections were ¼-20 sockets. They have a head diameter of 0.37 [in] and were pre-torqued to 7.5 [N-m] with a coefficient of friction of 0.2. It was subjected to the loads specified for B3 and B4 in Appendix A.1. The specifications of the mesh used are defined in

Table 25. The mesh was refined in areas that extended beyond the head of the screw. Surfaces surrounding the screw connection were also refined.

The material of the horizontal bearing holder and bottom cover was set to AISI4130 which is similar to the chosen material of 4140. Solidworks Simulation lists the yield and ultimate strength of AISI4130 as 460 and 560 [Mpa] respectively. The minimum factor of safety calculated was 3.28, which occurs in a small area under the outer most edge of the screw head.

Table 25: Summary of mesher and solver information from Solidworks Simulation for the horizontal bearing holder.

Mesher	
Mesh type	Solid Mesh
Mesher Used	Standard mesh
Jacobian points	4 points
Element size	4 mm
Tolerance	0.15 mm
Mesh quality	High
Total nodes	225566
Total elements	157089
Maximum Aspect Ratio	8.4652
with Aspect Ratio < 3	99.1
with Aspect Ratio > 10	0
(Jacobian)	5.08
Solver	
No. of DOF	710070
Total solution time	0:42:31

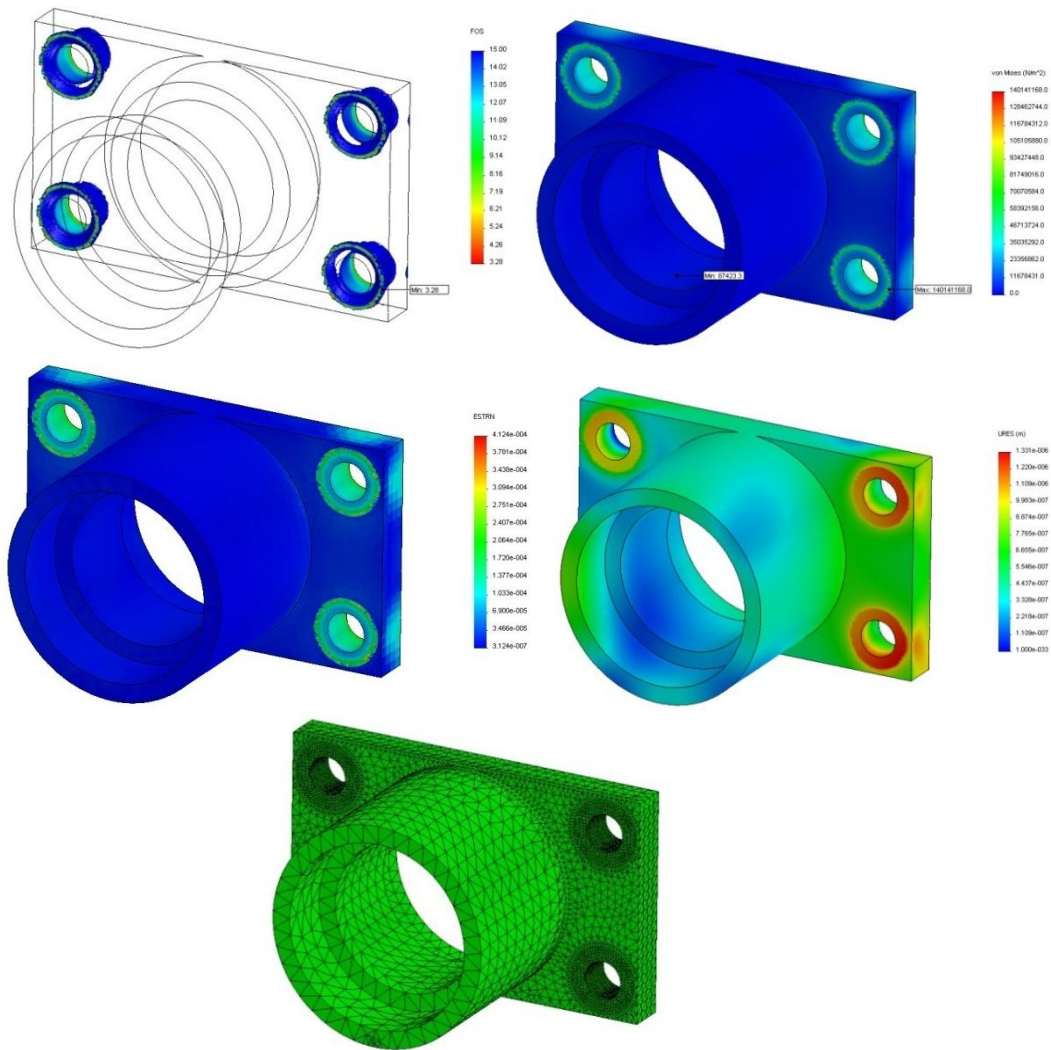


Fig. 58: From left to right and top to bottom. Factor of safety plot based on a yield strength of 460 [Mpa] with ISO clipping, stress plot, strain plot, displacement plot, and mesh.

B.3 Top Cover

Solidworks Simulation was used to perform a static FEA analysis on the top cover. The results of the analysis are shown in Fig. 59. The loads are listed in Appendix A.5. The solution and mesh details are summarized in Table 26.

The top flange was used as a fixture for the bolted connections, but was not of interest in this analysis. In defining the model a global no penetration contact was specified. The one screw connection was a ¼-20 socket. It had a head diameter of 0.37 [in] and was

pre-torqued to 7.5 [N-m] with a coefficient of friction of 0.2. The top cover was applied to the same loads specified in the top cover bolt calculations, but are adjusted for the 1/8th section.

The analysis shows that they surfaces under the heads of the screws are likely experiencing a small amount of yielding. This will not compromise the integrity of the part. Overall the stresses are much lower than the yield strength of AISI304 which is 206.8 [Mpa]. The previous bolt calculations confirm the integrity of these connections.

Table 26: Summary of mesh and solver information from Solidworks Simulation for the top cover.

Mesher	
Mesh type	Solid Mesh
Mesher Used	Standard mesh
Jacobian points	4 points
Element size	0.06 in
Tolerance	0.003 in
Mesh quality	High
Total nodes	80291
Total elements	51757
Maximum Aspect Ratio	5.0832
with Aspect Ratio < 3	99.8
with Aspect Ratio > 10	0
(Jacobian)	0
Solver	
No. of DOF	239856
Total solution time	1:04:41

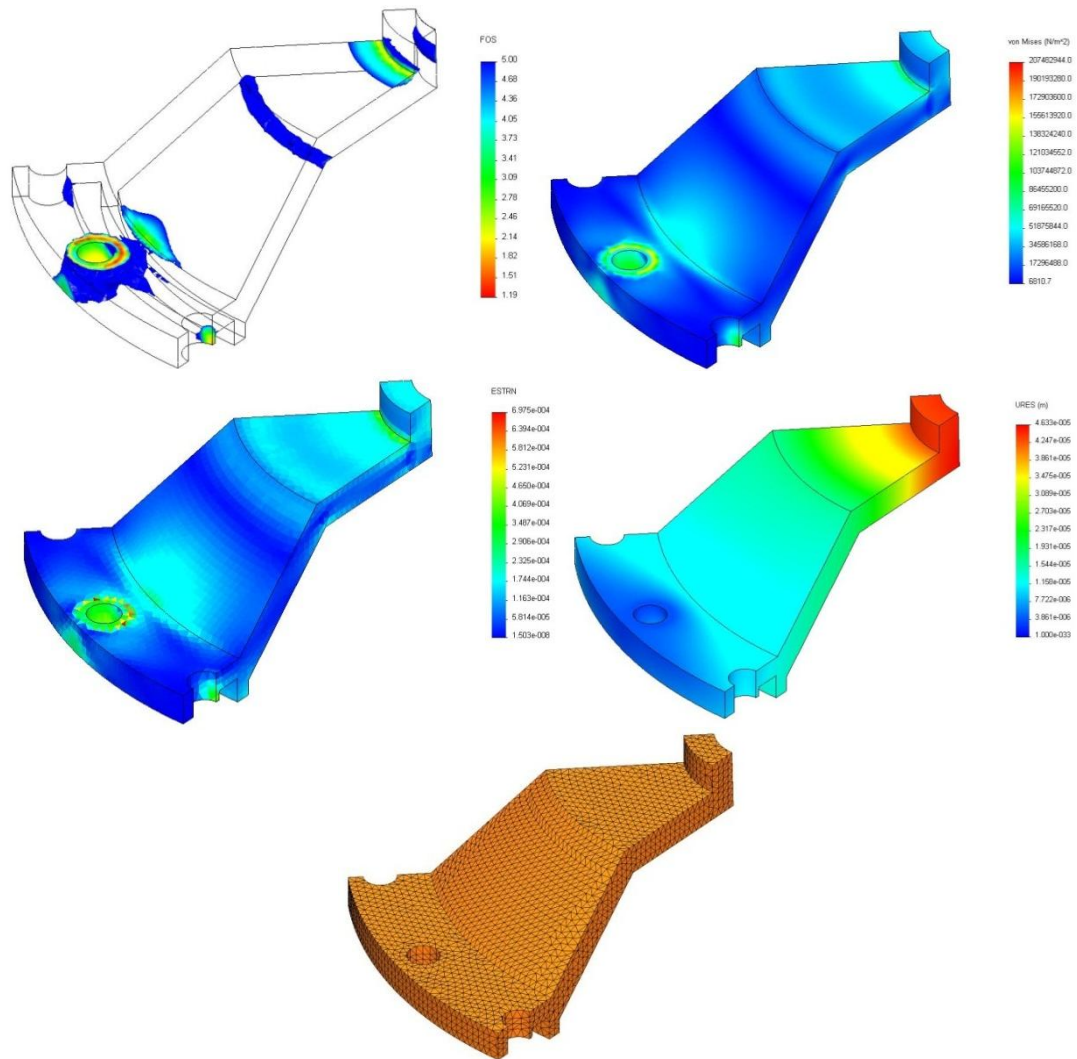


Fig. 59: From left to right and top to bottom. Factor of safety plot based on a yield strength of 206.8 [Mpa] with ISO clipping, Stress plot, strain plot, displacement plot, and mesh.

B.4 Tube Assembly

Solidworks Simulation was used to perform a static FEA analysis on tube assembly which included the top flange, tube, and bottom flange. Circular symmetry was used to reduce the computational time. The results of the analysis are shown in Fig. 60. The solution and mesh details are summarized in Table 27. The direct sparse solver was used.

In the assembly the top and bottom flange are bonded to the tube. A roller restraint is applied to the top and bottom flange. The assembly is fixed at the thread locations

on the bottom flange. The housing is subjected to a uniform 66 [psi] pressure differential, a force of 96 [lbf] caused by the piston seal, 250 [lbf] from the top cover, and 178 [lbf] from the bottom cover. All components are made of AISI304.

The results show that the maximum stress occurs in the ring that supports the scroll base. The minimum factor of safety is 4.58 based on a yield strength of 206.8 [Mpa].

Table 27: Summary of mesh and solver information from Solidworks Simulation for the tubing assembly.

Mesher	
Mesh type	Solid Mesh
Mesher Used	Standard mesh
Jacobian points	4 points
Mesh Control	Defined
Element size	0.11 in
Tolerance	0.0055 in
Mesh quality	High
Total nodes	218106
Total elements	136753
Maximum Aspect Ratio	6.199
with Aspect Ratio < 3	95.8
with Aspect Ratio > 10 (Jacobian)	0
Solver	
No. of DOF	652986
Total solution time	0:28:57

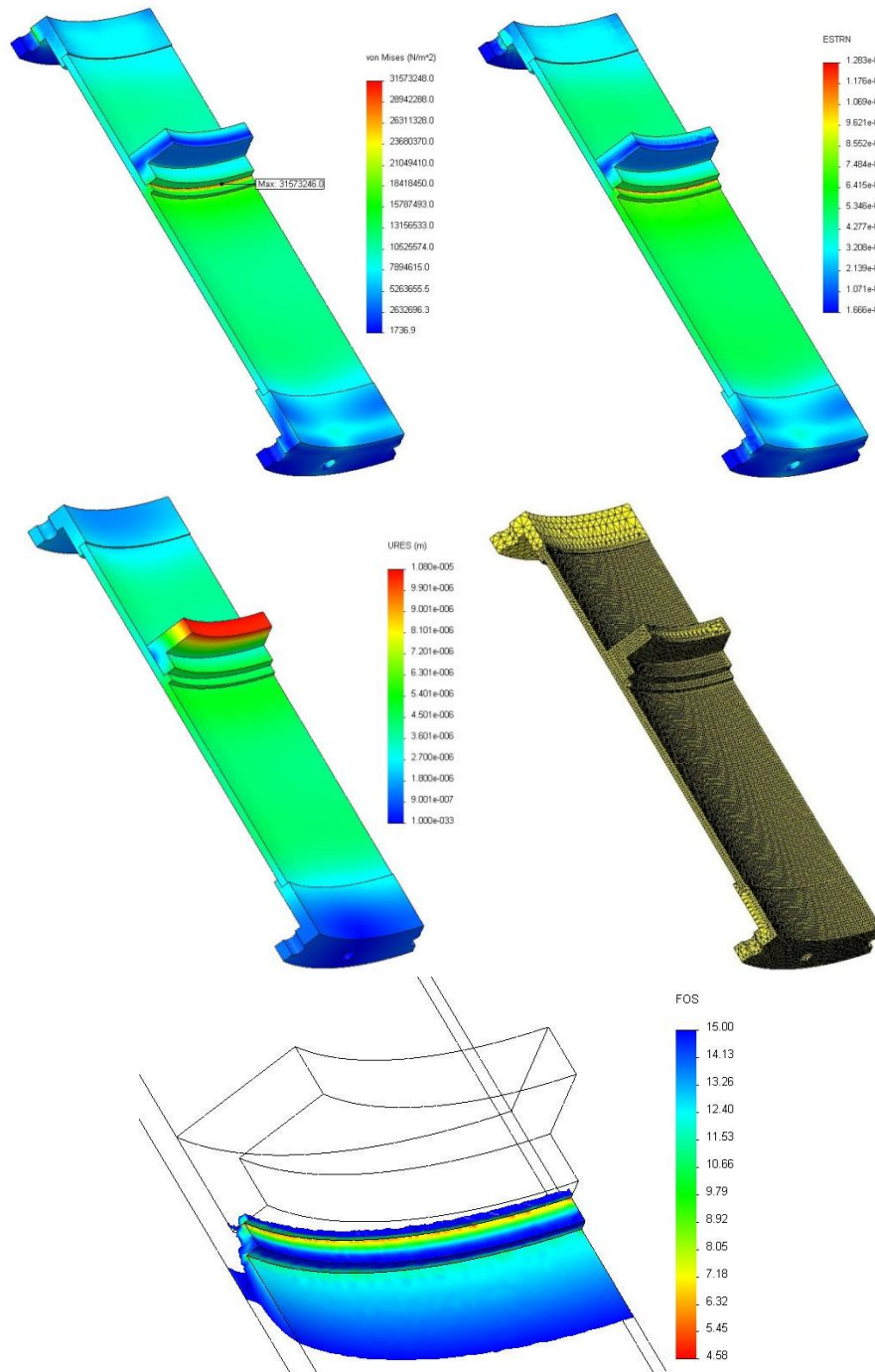


Fig. 60: FEA analysis of the tube assembly. Top to bottom and left to right: Stress plot, strain plot, displacement plot, mesh, and factor of safety distribution with ISO clipping based on a yield strength of 206.8 [Mpa].

B.5 Bottom Cover

An FEA Simulation was performed on the bottom cover. It experiences a uniform 66 [psi] pressure differential. It is the bulkiest part and is also subject to the smallest loads. It is no surprise that the majority of the areas have a factor of safety in excess of 50. The results of this analysis are uninteresting and are not presented.

Appendix C: Engineering Drawings

Table 28: Bill of materials

#	Assembly	Description	Material	Quantity
1	B	Top Cover	AISI304	1
2	B	Top Flange	AISI304	1
3	B	Tube	AISI304	1
4	B	Exit Port	AISI304	1
5	B	Support Ring	AISI304	1
6	B	Bottom Flange	AISI304	1
7	C	Bottom Cover	AISI4140	1
8	C	Artificial Sump	6061-T6	1
9	C,D	Vertical Bearing Holder	6061-T6	1
10	A,C,D	Main Shaft	Steel	1
11	C,D	Large Counterweight	Stainless Cast	1
12	C,D	Small Counterweight	Stainless Cast	1
13	C,E	Horizontal Bearing Holder	AISI4140	1
14	C,E	Power Takeoff Shaft	AISI440C	1
15	A	Sealing Piston	-	1
16	A	Stationary Scroll	Cast Iron	1
17	A	Orbiting Scroll	Cast Iron	1
18	A	Oldham	Aluminum	1
19	A	Scroll Base	Steel	1
20	A	Knuckle Bearing	Steel	1
21	A	Linear Bearings	Steel	3
22	A	3/16 Swagelok Cap	Stainless Steel	1
23	C,D	Gear MMSG2-25R	Steel	1
24	C,E	Gear MMSG2-25L	Steel	1
25	C,D	W6205 Bearing	Stainless Steel	1
26	C,E	6201-RSL Bearing	Steel	2
27	C,E	SB40 Shaft Seal	Teflon	1
28	C,D	1/8" Alignment Pin, 3/4"	Stainless Steel	2
29	C,E	1/8" Alignment Pin, 1/2"	Stainless Steel	2
30	C,D	1/8" Dowel Pin, 1-1/2"	Steel	3
31	B	¼-20 Hex Bolt, ½"	Stainless Steel	22
32	C,D	¼-20 Hex Bolt, 7/8"	Stainless Steel	4
33	C,E	¼-20 Hex Bolt, 7/16"	Stainless Steel	4
34	A,B	M8-1.25 Hex Bolt, 50 [mm]	Stainless Steel	3
35	C	8-32 Hex Bolt, 1-1/8"	Stainless Steel	4
36	C,E	¼-20 Set Screw, 5/8"	Steel	1
37	B	1/16X1.4X5/8" Washer	Stainless Steel	3
38	C,E	0.06X1.5X0.575" Washer	Stainless Steel	1
39	A	Spring	Steel	3
40	B	O-rings	Teflon-Viton	2

#	Description	Quantity
1	Top Cover	1
31	1/4-20 Hex Bolt, 1/2"	22
A	Scroll Assembly	1
B	Housing Assembly	1
C	Bottom Cover Assembly	1
D	Main Shaft Assembly	1
E	Powertake Off Assembly	1

OSU Oregon State University
Mechanical Engineering

Expander Assembly

DATE: 11/12/12
SCALE: 1:1
DRAWN: [blank]
CHECKED: [blank]
APPROVED: [blank]

#	Description	Quantity
15	Sealing Piston	1
16	Stationary Scroll	1
17	Orbiting Scroll	1
18	Oldman	1
19	Scroll Base	1
20	Knuckle Bearing	1
21	Linear Bearing	3
22	3/16 Swagelok Cap	1
34	M8-1.25 Hex Bolt, 50 [mm]	3
37	1/16X1.4X5/8" Washer	3
39	Springs	3

OSU Oregon State University
Mechanical Engineering

Scroll Assembly

DATE: 11/12/12
SCALE: 1:1
DRAWN: [blank]
CHECKED: [blank]
APPROVED: [blank]

#	Description	Quantity
2	Top Flange	1
3	Tube	1
4	Exit Port	1
5	Support Ring	1
6	Bottom Flange	1

DIMENSIONS ARE IN INCHES

TOLERANCES:

LINEAR: XXX ±0.01

XXXX ±0.0005

XXXXXXXX ±0.0010

ANGULAR: 1° ±10"

2.2° ±25"

MATERIAL:

FINISH:

SCALE: 1:2

DATE: 10/13/11

OSU Oregon State University
Mechanical Engineering

B Housing Assembly

REV: 00

APP: A

#	Description	Quantity
7	Bottom Cover	1
8	Artificial Sump	1
24	Gear MMSG2-25L	1
27	S840 Shaft Seal	1
32	1/4-20 Hex Bolt, 7/8"	4
33	1/4-20 Hex Bolt, 7/16"	4
35	8-32 Hex Bolt, 1-1/8"	4
36	1/4-20 Set Screw, 5/8"	1
38	0.06X1.5X0.575" Washer	1
D	Main Shaft Assembly	1
E	Powertake Off Assembly	1

DIMENSIONS ARE IN INCHES

TOLERANCES:

LINEAR: XXX ±0.01

XXXX ±0.0005

XXXXXXXX ±0.0010

ANGULAR: 1° ±10"

2.2° ±25"

MATERIAL:

FINISH:

SCALE: 1:2

DATE: 10/13/11

OSU Oregon State University
Mechanical Engineering

C Bottom Cover Assembly

REV: 00

APP: A

#	Description	Quantity
9	Vertical Bearing Holder	1
10	Main Shaft	1
11	Large Counterweight	1
12	Small Counterweight	1
23	Gear MMSG2-25R	1
25	W 6205 Bearing	1
28	1/8" Alignment Pins, 3/4"	2
30	1/8" Dowel Pins, 1-1/2"	3

DIMENSIONS ARE IN INCHES		OSU Oregon State University Mechanical Engineering
TOLERANCES:		
LINEAR:	XXX ±0.01	D Main Shaft Assembly
XXX ±0.005	XXX ±0.002	
ANGULAR:	° ±1.0	
° ±0.5		
UNITED STATES		
DATE:		
SCALE: 1:2	SHEET 01	REV: 00

#	Description	Quantity
13	Horizontal Bearing Holder	1
14	Power Takeoff Shaft	1
26	6201-RSL Bearing	2
29	1/8" Alignment Pin, 1/2"	2

DIMENSIONS ARE IN INCHES		OSU Oregon State University Mechanical Engineering
TOLERANCES:		
LINEAR:	XXX ±0.01	E Power Takeoff Shaft Assembly
XXX ±0.005	XXX ±0.002	
ANGULAR:	° ±1.0	
° ±0.5		
UNITED STATES		
DATE:		
SCALE: 1:2	SHEET 1 OF 1	REV: 00

